

*INVESTIGATING WIND-DRIVEN SURFACE
CURRENTS IN THE RHEIC OCEAN
THROUGH MODELLING*

Melissa Vleugel

MSc Thesis



Department of Earth Sciences, Utrecht University

March 2019

Supervisors:

Dr. P. Th. Meijer

Dr. J. Trabucho Alexandre

*The ocean has its silent caves,
Deep, quiet and alone;
Though there be fury on the waves,
Beneath them there is none.*

“The Ocean” (1–4)

by Nathaniel Hawthorne

ABSTRACT

The Rheic Ocean was one of the most important oceans of the Paleozoic, evidenced by remnants that can be found across present-day Central America, North America, Europe, and Northern Africa. Its closure led to the formation of Pangea and has been attributed to the abrupt change in climate and mass extinctions that occurred at the end of the Devonian. Although geological evidence of the shallow environments of the Rheic Ocean can be found at its former margin edges, subduction of the ocean and subsequent destruction of its lithosphere leaves no direct evidence of its deep-sea environment. Inferences of the mid-Paleozoic oceanic surface circulation within the Rheic Ocean have thus far been made through the application of general oceanic theory in schematic reconstructions. This study was aimed at testing several published schematic reconstructions through numerical modelling, thereby increasing the understanding of the Rheic Ocean surface circulation. A numerical ocean model was constructed with the Princeton Ocean Model (POM). An additional aim of this study involved determining whether the model could be used to infer the position of peri-Gondwanan terranes and the paleoposition of Gondwana in the mid-Paleozoic. Experiments were carried out to test various aspects of three known controls on surface circulation, namely the paleogeography, wind stress, and Coriolis force. The experiments showed that the model was sensitive to wind stress, throughflow and bathymetry in particular. The resulting circulation patterns justify the depiction of certain oceanographic phenomena in the schematic reconstructions, such as a Western Boundary Current (WBC) and gyres. Higher velocities gave some indication of the position of Gondwana as well as the peri-Gondwanan terranes. The sensitivity of the model to bathymetry, however, makes it difficult to make directly correlate terrane orientation and Gondwanan paleoposition to an increase in velocity. We propose the model be further improved by expanding it to a three-dimensional model and by refining the bathymetry. This can be achieved by focusing on smaller basins and obtaining a more detailed bathymetry from published research. Another option would be to use the knowledge obtained in this study in combination with an approximated tectonic model to create a global circulation model. This global model could then be used to gain a better understanding of the dynamics between ocean closure, climate change and extinction that took place in the Devonian.

CONTENTS

1 INTRODUCTION.....	1
1.1 RATIONALE	1
1.1.1 <i>Why use numerical modelling?</i>	5
1.2 OBJECTIVE AND RESEARCH QUESTIONS.....	6
2 BACKGROUND	7
2.1 HISTORY OF THE RHEIC OCEAN	7
2.1.1 <i>Geodynamic scenario</i>	8
2.2 MAIN PALEOGEOGRAPHIC CONTROVERSIES	11
2.3 RHEIC PALEOCEANOGRAPHY AND CLIMATE	18
2.3.1 <i>Available mid-Paleozoic schematic reconstructions</i>	19
3 MODELLING APPROACH.....	23
3.1 EXPERIMENTAL SETUP	23
3.2 MODEL CONFIGURATION AND INPUT DATA	23
3.2.1 <i>Land-sea distributions</i>	24
3.2.2 <i>Bathymetries</i>	26
3.2.3 <i>Boundary Conditions</i>	27
3.2.4 <i>Wind stress</i>	27
3.2.5 <i>Coriolis Parameter</i>	34
3.3 DATA ANALYSIS	34
4 RESULTS AND ANALYSIS	37
4.1 REFERENCE EXPERIMENT.....	37
4.2 EFFECT OF PALEOGEOGRAPHY	42
4.2.1 <i>Influence of the land-sea distribution</i>	42
4.2.2 <i>Influence of bathymetry</i>	52
4.2.3 <i>Influence of throughflow</i>	56
4.3 EFFECT OF THE APPLIED WIND STRESS.....	60
4.4 EFFECT OF THE CORIOLIS PARAMETER	65
5 DISCUSSION	69
5.1 MODEL LIMITATIONS	69
5.2 MAIN PARAMETER SENSITIVITY	72
5.2.1 <i>Bathymetry</i>	72
5.2.2 <i>Throughflow</i>	78

5.2.3 <i>Applied zonal wind stress</i>	78
5.3 COMPARISON TO CONCEPTUAL CIRCULATION MODELS	80
5.4 CONTRIBUTION TO MID-PALEOZOIC PALEOGEOGRAPHY	83
6 CONCLUSION	87
7 ACKNOWLEDGEMENTS	91
8 REFERENCES	93
9 APPENDICES	101
APPENDIX A – COMPLETE SET OF MODEL DOMAINS	102
APPENDIX B – REPRODUCING THE DATA	103

LIST OF TABLES

TABLE 2-1: OVERVIEW OF THE INCONSISTENT NUMBER OF MID-PALEOZOIC OCEANIC DOMAINS BETWEEN LAURUSSIA AND GONDWANA AS REFERRED TO IN LITERATURE.	13
TABLE 3-1: INFORMATION ON THE LAND-SEA DISTRIBUTIONS USED IN THE EXPERIMENTS	26
TABLE 3-2: THE POM OUTPUT PARAMETERS USED FOR PLOTTING DATA IN GMT	35

LIST OF FIGURES

FIG. 1.1: RECONSTRUCTIONS DEPICTING THE RHEIC OCEAN CONFIGURATION AT 370 MA (LEFT) AND AFTER CLOSURE AT 280 MA (RIGHT) FROM NANCE ET AL. (2012).....	1
FIG. 1.2: EIFELIAN PALEOGEOGRAPHIC RECONSTRUCTION SHOWING THE LOCATION OF THE ARDENNES EXCURSION. PALEOMAP PROJECT ILLUSTRATION BY SCOTESE (N.D.).	2
FIG. 1.3: MAP OF THE MODERN-DAY EUROPEAN VARISCIDES. THE RED STAR INDICATES THE LOCATION OF THE CONDROZ SHELF. IMAGE MODIFIED FROM WOODCOCK, SOPER, AND STRACHAN (2007), ORIGINALLY BASED ON THE TECTONIC SUBDIVISIONS BY FRANKE (2000).	2
FIG. 1.4: SCHEMATIC RECONSTRUCTION OF FAMENNIAN OCEANIC CURRENTS WITHIN THE RHENOHERCYNIAN OCEAN. THE RED STAR INDICATES THE CONDROZ SHELF (PAPROTH ET AL., 1986).	4
FIG. 1.5: DEVONIAN RECONSTRUCTIONS SHOWING THE DEFLECTED COLD-WATER CURRENTS THOUGHT TO HAVE TRIGGERED CLIMATE CHANGE. FROM COPPER (1986).	5
FIG. 1.6: SCHEMATIC OCEANIC CIRCULATION RECONSTRUCTION SHOWING THE MAIN DEVONIAN CURRENTS IN THE RHEIC OCEAN, BY DOPIERALSKA (2009).....	6
FIG. 2.1: ILLUSTRATION OF THE PALEOZOIC OROGENIC BELTS RELATED TO THE CLOSURE OF THE RHEIC OCEAN (MARTÍNEZ CATALÁN ET AL., 2009).	7
FIG. 2.2: DIAGRAM BY FRANKE (1989) SHOWING THE MAIN STRUCTURAL ELEMENTS OF THE VARISCAN BELT.....	8
FIG. 2.3: RECONSTRUCTION OF THE PALEOGEOGRAPHIC CONFIGURATION OF THE RHEIC OCEAN DURING THE SILURIAN, SHOWING THE MAIN CONTINENTAL UNITS INVOLVED (NANCE ET AL., 2010).	9
FIG. 2.4: CONCEPTUAL REPRESENTATION OF THE OROGENIC BELTS THAT RESULTED FROM IAPETUS CLOSURE (RED) AND RHEIC CLOSURE (BLACK) (NANCE ET AL., 2010).	11
FIG. 2.5: RECONSTRUCTIONS AVAILABLE FROM SIX DIFFERENT SOURCES IN LITERATURE ARE RE-PROJECTED WITH SCHMIDT’S PROJECTION FOR ALL (DOPIERALSKA, 2003).	12
FIG. 2.6: ILLUSTRATION BY SHAIL AND LEVERIDGE (2009) SHOWING SEVERAL WAYS IN WHICH THE RHENOHERCYNIAN OCEAN (RHZ) COULD RELATE TO THE RHEIC OCEAN.	15
FIG. 2.7: EXAMPLE OF A RECONSTRUCTION THAT INCLUDES MULTIPLE PERI-GONDWANAN TERRANES AND ASSOCIATED OCEANS. TERRANES INCLUDE FRANCONIA (F), THURINGIA (T), IBERIAN PENINSULA (IB), ARMORICA (AR), BOHEMIA (B), AND PALEO-ADRIA (PA). MODIFIED FROM FRANKE ET AL. (2017).	16
FIG. 2.8: ALTERNATIVE APW CURVES FOR GONDWANA IN PALEOZOIC SHOWING THE A) GRADUAL NORTHWARD MOVEMENT OR B) RAPID NORTHWARD AND THEN SOUTHWARD MOVEMENT. IMAGE FROM TAIT ET AL. (2000).	17
FIG. 2.9: DIAGRAM REPRESENTING THE DIFFERENCES BETWEEN THE PANGAEA-C CONFIGURATION (LEFT) AND PANGAEA-A CONFIGURATION (RIGHT) (TORSVIK AND COCKS, 2004).....	17
FIG. 2.10: LATE DEVONIAN TO EARLY CARBONIFEROUS PALEOGEOGRAPHIC RECONSTRUCTION BY (ECKELMANN ET AL., 2014).	18

FIG. 2.11: SCHEMATIC OVERVIEW OF THE PRESENT-DAY GLOBAL WIND-DRIVEN SURFACE CURRENTS AND OUTLINE (RED BOX) OF THE LATITUDINAL REGION THAT THE RHEIC OCEAN WOULD HAVE OCCUPIED, MODIFIED FROM SEGAR (2018).	19
FIG. 2.12: SCHEMATIC RECONSTRUCTION OF THE SURFACE WATER CIRCULATION BETWEEN GONDWANA AND LAURUSSIA IN THE MIDDLE DEVONIAN (OCZLON, 1990).....	20
FIG. 2.13: GLOBAL GIVETIAN-FRASNIAN OCEAN SURFACE CURRENTS, RECONSTRUCTION FROM KIESSLING, FLÜGEL, AND GOLONKA (1999).	20
FIG. 3.1: ROTATED CONTINENTAL UNITS (BLACK OUTLINE) OVERLAIN ON PALEOGEOGRAPHIC RECONSTRUCTIONS BY TORSVIK ET AL. (2012) SHOWN IN GREEN AND BLUE.	25
FIG. 3.2: DEPICTION OF THE MODEL DOMAIN, IN THIS CASE FOR THE EMSIAN SCENARIO. IN AN EQUIDISTANT PROJECTION (LEFT) AND AN ORTHOGRAPHIC (RIGHT) PROJECTION. BOLD OUTLINE IN THE ORTHOGONAL PROJECTION REPRESENTS THE MODEL DOMAIN.	26
FIG. 3.3: MODIFIED DIAGRAM OF THE GEOTECTONIC MODEL BY ECKELMANN ET AL. (2014) ON WHICH THE VARIABLE BATHYMETRY WAS BASED.....	27
FIG. 3.4: DEPICTION OF DATA FROM THE NOAA BLENDED SEA WINDS DATABASE SHOWING A) THE GLOBAL WIND STRESS MAGNITUDES PRIOR TO MANIPULATION AND MODEL DOMAIN OUTLINE AND B) WIND STRESS MAGNITUDES WITHIN THE MODEL DOMAIN AFTER MANIPULATION.	28
FIG. 3.5: ZONAL WIND STRESS REPRESENTED AS A FUNCTION OF LATITUDE, y . IMAGE FROM MELLOR (1996).....	29
FIG. 3.6: VISUALIZATION OF THE IDEALIZED WIND STRESS FUNCTION.	30
FIG. 3.7: CURVE OF THE ZONAL WIND STRESS VARYING WITH LATITUDE, MODIFIED FROM POND AND PICKARD (2013).	30
FIG. 3.8: DEPICTION OF THE STANDARD COSINE FUNCTION. A IS THE AMPLITUDE, B IS THE WAVELENGTH, C THE HORIZONTAL SHIFT, AND D THE VERTICAL SHIFT.....	31
FIG. 3.9: IDEALIZED WIND STRESS FUNCTION ACCORDING TO EQUATION 3.4. RED REPRESENTS THE LATITUDINAL AREA OF THE MODEL DOMAIN.....	32
FIG. 3.10: COMPARISON OF THE IDEALIZED WIND STRESS FUNCTION USED IN THE REFERENCE (REF) EXPERIMENTS WITHIN THE MODEL (BLACK) AND OBSERVED NOAA SATELLITE DATA (BLUE).	33
FIG. 3.11: COMPARISON OF THE DIFFERENT ASYMMETRIES (RED AND DASHED LINES) TO OBSERVED NOAA SATELLITE DATA (BLUE).....	34
FIG. 4.1: ORTHOGRAPHIC PROJECTION OF ROTATED CONTINENTAL UNITS, SHOWING THE OUTLINED MODEL DOMAIN (LEFT). LINEAR PROJECTION OF MODEL DOMAIN WITH THE LAND-SEA DISTRIBUTION OF THE EMSIAN REFERENCE EXPERIMENT SHOWN RIGHT.....	37
FIG. 4.2: REFERENCE EXPERIMENT BASIN-AVERAGED VELOCITY, MEAN ELEVATION OF THE FREE SURFACE (SURFACE ELEVATION) AND BASIN-AVERAGED KINETIC ENERGY OVER THE MODEL RUNTIME OF 150 DAYS.	38
FIG. 4.3: MODEL DOMAIN OF THE EMSIAN REFERENCE EXPERIMENT, SHOWING THE DIRECTION AND INTENSITY OF APPLIED WIND STRESS ON THE BASIN.....	39
FIG. 4.4: REFERENCE MODEL DOMAIN SHOWING THE A) GENERATED DEPTH-AVERAGED HORIZONTAL VELOCITIES AND B) FREE SURFACE ELEVATION OF THE BASIN.	41

FIG. 4.5: FAMENNIAN PALEOGEOGRAPHIC EXPERIMENT SERIES WITH A) LAND-SEA DISTRIBUTION OF THE TORSVIK RECONSTRUCTION INCLUDING THE SAXOTHURINGIAN TERRANE (S.T.), MOESIA TERRANE (M.T.) AND ARMORICAN TERRANE ASSEMBLAGE (ATA), AND B) THE RESULTING DEPTH-AVERAGED HORIZONTAL VELOCITY PATTERN.....	43
FIG. 4.6: FAMENNIAN PALEOGEOGRAPHIC EXPERIMENT SERIES: A) LAND-SEA DISTRIBUTION BASED ON THE RECONSTRUCTION FROM DOPIERALSKA (2009) INCLUDING THE RHENOHERCYNIAN TERRANE (R.T.) AND B) DEPTH-AVERAGED HORIZONTAL VELOCITY PATTERN.....	45
FIG. 4.7: FAMENNIAN PALEOGEOGRAPHIC EXPERIMENT SERIES: A) LAND-SEA DISTRIBUTION OF THE HUNEKE RECONSTRUCTION INCLUDING THE NORIC TERRANE (N.T.) AND ARMORICAN TERRANE ASSEMBLAGE (ATA), AND B) DEPTH-AVERAGED HORIZONTAL VELOCITY PATTERN.....	47
FIG. 4.8: EFFECT OF CLOSURE OF THE TOURNAISIAN SEAWAY: A) DEPTH-AVERAGED HORIZONTAL VELOCITY PATTERN AND LAND-SEA DISTRIBUTION INCLUDING THE ARMORICAN TERRANE ASSEMBLAGE (ATA), AND B) SURFACE ELEVATION OF THE BASIN.....	49
FIG. 4.9: EFFECT OF SHELF BREAK AS A SURFACE CURRENT BARRIER. FIGURE A) SHOWS THE DEPTH-AVERAGED HORIZONTAL PATTERN OF THE REFERENCE EXPERIMENT WHICH INCLUDES A SHELF AND FIGURE B) SHOWS THE SURFACE CURRENT PATTERN WHEN NO SHELF IS INCLUDED.....	51
FIG. 4.10: EMSIAN GENERATED BATHYMETRY EXPERIMENT RESULTS. FIGURE A) SHOWS THE GENERATED BATHYMETRY MASK FOR THE EMSIAN CONFIGURATION, B) THE DEPTH-AVERAGED HORIZONTAL VELOCITY PATTERN FOR EMSIAN CONFIGURATION WITH GENERATED BATHYMETRY, AND C) EMSIAN EXPERIMENT TIME SERIES OF THE AVERAGE KINETIC ENERGY OF THE BASIN OVER A RUNTIME OF 150 DAYS.....	53
FIG. 4.11: FAMENNIAN GENERATED BATHYMETRY EXPERIMENT RESULTS, FIGURE A) SHOWS THE GENERATED BATHYMETRY MASK FOR THE EMSIAN CONFIGURATION, B) THE DEPTH-AVERAGED HORIZONTAL VELOCITIES, AND C) FAMENNIAN EXPERIMENT TIME SERIES OF THE AVERAGE KINETIC ENERGY OF THE BASIN OVER A RUNTIME OF 150 DAYS.....	55
FIG. 4.12: EFFECT OF A NET WESTWARD FLOW (THROUGHFLOW) OF 1 SVERDRUP: A) DEPTH-AVERAGED VELOCITY PATTERN OF AN EMSIAN BASIN GEOMETRY WITH AN IDEALIZED ZONAL WIND STRESS AND UNIFORM DEPTH OF 200 METERS, B) MEAN SURFACE ELEVATION AND C) SURFACE ELEVATION TIME SERIES FOR A RUN OF 150 DAYS.....	57
FIG. 4.13: EFFECT OF A NET WESTWARD FLOW (THROUGHFLOW) OF 5 SVERDRUP: A) DEPTH-AVERAGED VELOCITY PATTERN OF AN EMSIAN BASIN GEOMETRY WITH AN IDEALIZED ZONAL WIND STRESS AND UNIFORM DEPTH OF 200 METERS, B) MEAN SURFACE ELEVATION AND C) SURFACE ELEVATION TIME SERIES FOR A RUN OF 150 DAYS.....	58
FIG. 4.14: EFFECT OF A NET WESTWARD FLOW (THROUGHFLOW) OF 7 SVERDRUP: A) DEPTH-AVERAGED VELOCITY PATTERN OF AN EMSIAN BASIN GEOMETRY WITH AN IDEALIZED ZONAL WIND STRESS AND UNIFORM DEPTH OF 200 METERS, B) MEAN SURFACE ELEVATION AND C) SURFACE ELEVATION TIME SERIES FOR A RUN OF 150 DAYS.....	59
FIG. 4.15: WIND STRESS PATTERNS APPLIED TO AN EMSIAN CONFIGURATION WITH UNIFORM DEPTH SHOWING THE A) IDEALIZED ZONAL WINDSTRESS, B) PRESENT-DAY WINDSTRESS	

FROM SATELLITE DATA, C) UNIFORM ZONAL WINDSTRESS AND D) AND UNIFORM MERIDIONAL WIND STRESS.....	62
FIG. 4.16: EFFECT OF VARIABLE WIND STRESS ON SURFACE CURRENT PATTERN, SHOWING THE DEPTH-AVERAGED HORIZONTAL VELOCITIES RESULTING FROM A) AN APPLIED IDEALIZED ZONAL WIND STRESS, B) PRESENT-DAY WIND STRESS, C) UNIFORM ZONAL WIND STRESS AND D) AND UNIFORM MERIDIONAL WIND STRESS.	64
FIG. 4.17: EFFECT OF A VARYING CORIOLIS PARAMETER ON THE SURFACE CURRENT PATTERN. RESULTING DEPTH-AVERAGED HORIZONTAL VELOCITIES AFTER APPLYING THE A) PRESENT-DAY CORIOLIS PARAMETER VALUE, B) DEVONIAN VALUE, C) UNIFORM VALUE AND D) ZERO CORIOLIS PARAMETER.	67
FIG. 5.1: MODIFIED VERSION OF THE MERIDIONAL WIND STRESS EXPERIMENT SHOWN IN FIG. 4.16. RED LINES HIGHLIGHT AREAS SUBJECTED TO THE GREATEST BOUNDARY EFFECTS.....	70
FIG. 5.2: FIGURE SHOWING THE FULL EXTENT OF THE KASKASKIA SEA, INDICATED BY THE RED BOX. MODIFIED FROM TORSVIK AND COCKS (2016).....	71
FIG. 5.3: EARLY DEVONIAN PALEO GEOGRAPHIC RECONSTRUCTION, THE RED BOX HIGHLIGHTS HOW IN THIS RECONSTRUCTION EUROPE WAS PREDOMINANTLY ONE LARGE SHELF. MODIFIED FROM STETS AND SCHÄFER (2011).....	73
FIG. 5.4: EXAMPLE OF A SMALLER BASIN-SCALE STUDY. SHOWING CIRCULATION WITHIN THE UPPER DEVONIAN CATSKILL SEA. MODIFIED FROM SLINGERLAND (1986).....	74
FIG. 5.5: CROSS SECTION OF THE EARLY DEVONIAN RHENOHERCYNIAN BASIN THAT SERVES AS AN EXAMPLE OF HOW LOCAL TECTONICS CAN BE INCORPORATED INTO BASIN-SCALE MODELS (STETS AND SCHÄFER, 2011).....	75
FIG. 5.6: ILLUSTRATION OF THE RELATIONSHIP BETWEEN AGE, FLEXURE, AND DEPTH OF OCEANIC LITHOSPHERE (CROSBY ET AL., 2006).....	76
FIG. 5.7: AGE-AREA DISTRIBUTION OF OCEANIC CRUST AT 230 MA. MODIFIED FROM MÜLLER ET AL. (2016).	76
FIG. 5.8: EXAMPLE OF A GLOBAL SCALE MODEL, SHOWING A LATE ORDOVICIAN (440 MA) CIRCULATION PATTERN FROM POHL ET AL. (2016).	77
FIG. 5.9: EFFECT OF RHEIC CLOSURE ON THE GLOBAL CIRCULATION (SMITH AND READ, 2000).	77
FIG. 5.10: IDEALIZED SURFACE WIND IN THE NORTHERN HEMISPHERE, MODIFIED FROM CHERESKIN AND PRICE (2018).....	79
FIG. 5.11: MODERN-DAY WINDS STRESSES FROM THE NOAA DATABASE (BLUE) COMPARED TO THE IDEALIZED WIND STRESS CURVE WITH AN ALTERNATIVE WAVELENGTH OF $\pi/2$ (DASHED BLACK), AND CURVE WITH NO ASYMMETRY CALLED “IDEAL 0” (SOLID BLACK).	79
FIG. 5.12: GLOBAL PATTERN OF OCEANIC SURFACE CIRCULATION IN THE GIVETIAN-FRASNIAN EPOCHS, MODIFIED FROM HÜNEKE (2006).....	80
FIG. 5.13: MID-DEVONIAN SEAWATER CIRCULATION FROM JAKUBOWICZ ET AL. (2019) BASED ON THE SCHEMATIC RECONSTRUCTION BY OCZLON (1990). THE SOUTH EQUATORIAL CURRENT (SEC) AND NORTH GONDWANAN CURRENT (NGC) ARE LOCATED MORE SOUTHWARD IN THIS RECONSTRUCTION.	81

FIG. 5.14: AN ANNOTATED VERSION OF THE FAMENNIAN EXPERIMENT RESULTS SHOWN IN FIG. 4.6B. BLUE ANNOTATIONS HIGHLIGHT HOW THE PROTRUDING EDGES OF PERI-GONDWANAN TERRANES ARE SUBJECTED TO HIGHER VELOCITIES..... 85

FIG. 6.1: ILLUSTRATION FROM OLBERS ET AL. (2012). 89

1 INTRODUCTION

This study focuses on the Rheic Ocean, an ocean that receives relatively little attention compared to its Paleozoic counterparts such as the Iapetus and Panthalassa oceans, but which is nonetheless one of the most important oceans of its era (Nance et al., 2010). Spanning low- to mid-latitudes, this oceanic domain separated the Laurussian and Gondwanan continents prior to their convergence into the supercontinent Pangea (Torsvik and Cocks, 2016). This convergence led to one of the largest orogens of all time, still evidenced today by a suture zone spanning across Central and North America, Europe, and Northern Africa (Nance et al., 2010).

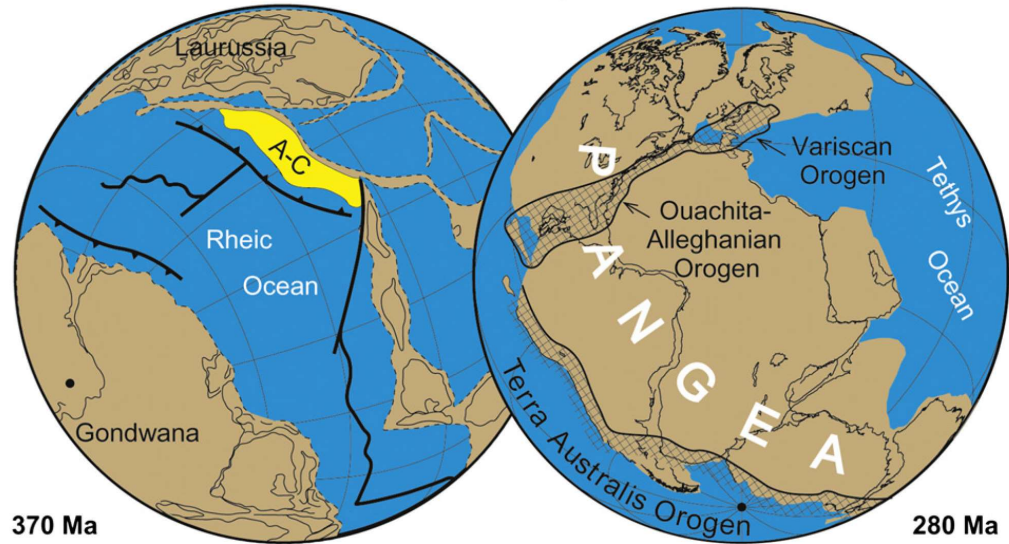


Fig. 1.1: Reconstructions depicting the Rheic Ocean configuration at 370 Ma (left) and after closure at 280 Ma (right) from Nance et al. (2012).

1.1 Rationale

The motivation behind this research originated from Rheic shelf deposits evidenced in the Bocq and Tailfer quarries in the Belgian Ardennes (Fig. 1.3). These quarries are visited during the Ardennes excursion, an annual excursion that is part of the BSc Earth Sciences program at Utrecht University. They are located in the Variscides (Fig. 1.2), within the European segment of the Rheic suture zone which was part of a wide, shallow continental shelf during the mid-Paleozoic, termed the Condrosz shelf (Paproth et al., 1986; Prestianni et al., 2010; Thorez et al., 2006).

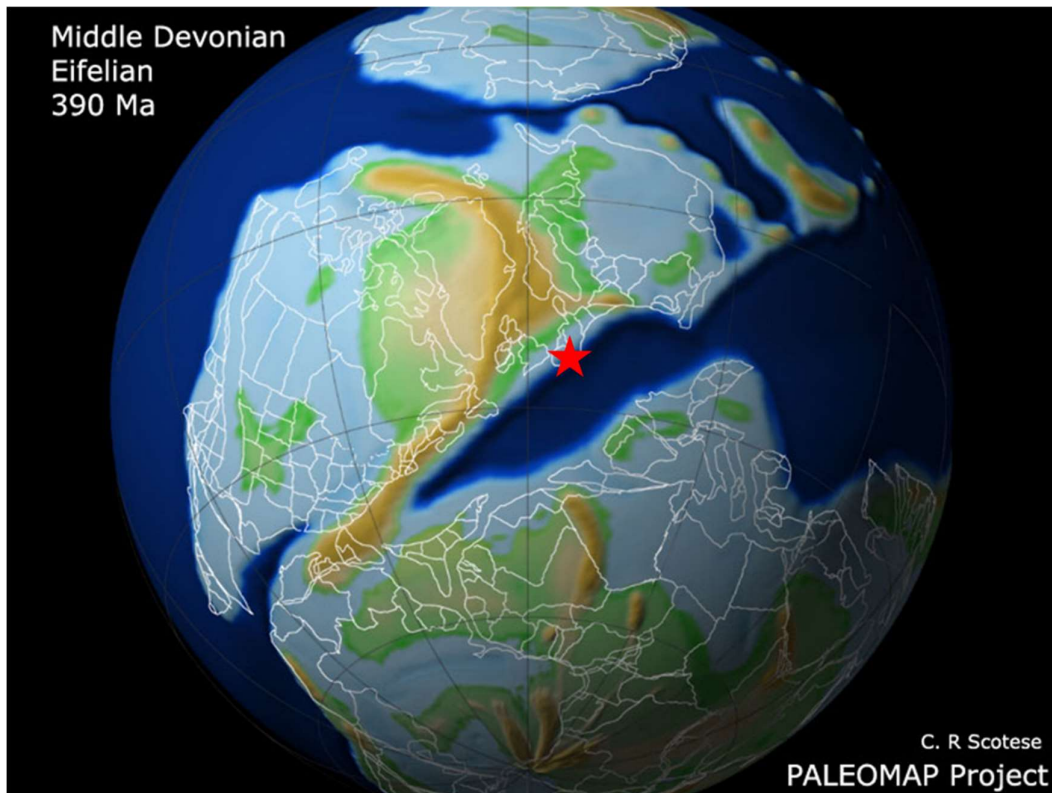


Fig. 1.2: Eifelian paleogeographic reconstruction showing the location of the Ardennes excursion. PALEOMAP project illustration by Scotese (n.d.).

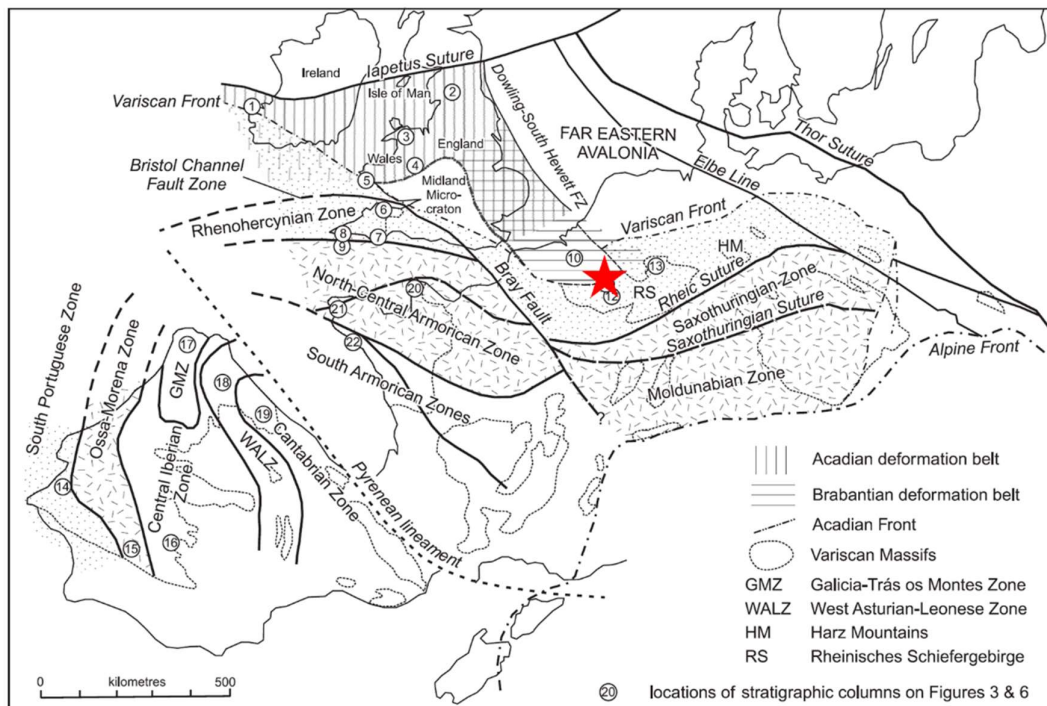


Fig. 1.3: Map of the modern-day European Variscides. The red star indicates the location of the Condroz shelf. Image modified from Woodcock, Soper, and Strachan (2007), originally based on the tectonic subdivisions by Franke (2000).

In their publication, Paproth et al. (1986) attributed delta lobe sediment dispersal on the Condruz shelf to the influence of a strong boundary current originating from the Paleotethys ocean to the east (Fig. 1.4). This boundary current, termed the Western Boundary Current or WBC, is inferred by assuming that general oceanographic phenomena related to the global surface circulation occurred within this region of the Rheic oceanic basin. Such phenomena can also be seen in the surface circulation patterns of modern-day oceans. This assumption sparked the question whether numerical modelling could be implemented to test the inference of the WBC phenomenon in this region, and to gain more insight into the oceanic circulation which the Condruz shelf was subjected to in general.

The location of the narrow seaway and connection to the Paleotethys led us to assume that this narrow oceanic basin was, in fact, the Rhenohercynian Ocean as described in Franke (1989) located at the northern margin of the much larger Rheic Ocean. The amount of incongruous information that has been published about the Rhenohercynian Ocean, however, led to the realisation that very little paleogeographic constraint exists with regards to this oceanic basin. In fact, a lack of paleomagnetic evidence meant there is no consensus on the formation of any of the smaller oceanic basins located between terranes within the larger Rheic Ocean, as the oceanic basins and terranes most likely remained smaller than the critical size of 500-1000 km needed to be recorded in the paleomagnetic record (Matte, 2001). Although the paleogeography for the larger Rheic Ocean is better-known than the Rhenohercynian Ocean, there are still many paleogeographic uncertainties still open to debate. These issues include an unknown number of terranes and related oceanic basins that could have existed within the Rheic Ocean region and an indefinite position of Gondwana with respect to Laurussia, which is further elucidated in section 2.2.

The objective of this study evolved from testing oceanic circulation patterns shown in schematic reconstructions such as a Western Boundary Current (WBC) in the Rhenohercynian Ocean, to testing these circulation patterns within the entire Rheic Ocean. The lack of paleogeographic constraint led to an additional aim: determining whether the model results of this study provide useful paleoceanographic insight on several aspects of Rheic paleogeography.

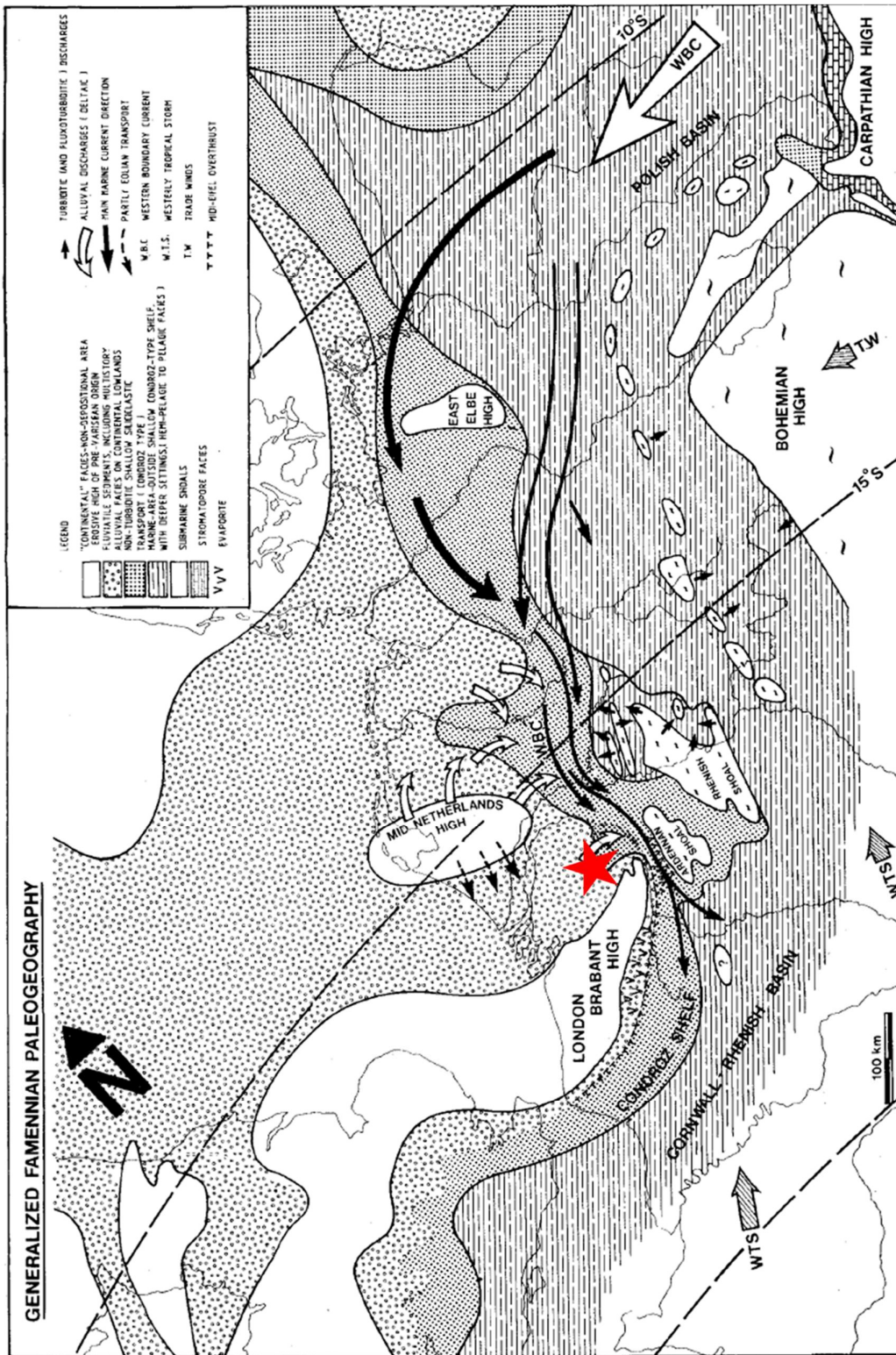


Fig. 1.4: Schematic reconstruction of Famennian oceanic currents within the Rheohercynian Ocean. The red star indicates the Condruz shelf (Paproth et al., 1986).

1.1.1 Why use numerical modelling?

The intricate relationship between oceans and atmosphere, and regulation of the global distribution of water, nutrients, and heat make oceanic circulation an important factor to consider. Many studies have been dedicated to exploring the influence of oceanic circulation on Paleozoic climate, biodiversity, and dispersal of sediments and fossils. For example, the environmental conditions of the Rheic Ocean are thought to have provided an ecological niche for the coral-stromatoporoid reefs that were so characteristically abundant in the Devonian (Copper, 2002; Zeh and Gerdes, 2010). Copper (1986) and Qiao and Shen (2014) specifically linked Late Devonian mass extinctions (the Kellwasser and Hangenberg events) to Rheic closure. Copper (1986) and De Vleeschouwer et al. (2014) additionally state that Late Devonian climate change and rapid cooling could have been the result of Rheic closure, which caused a deflection of the major paleoequatorial east-west oceanic current (Fig. 1.5)

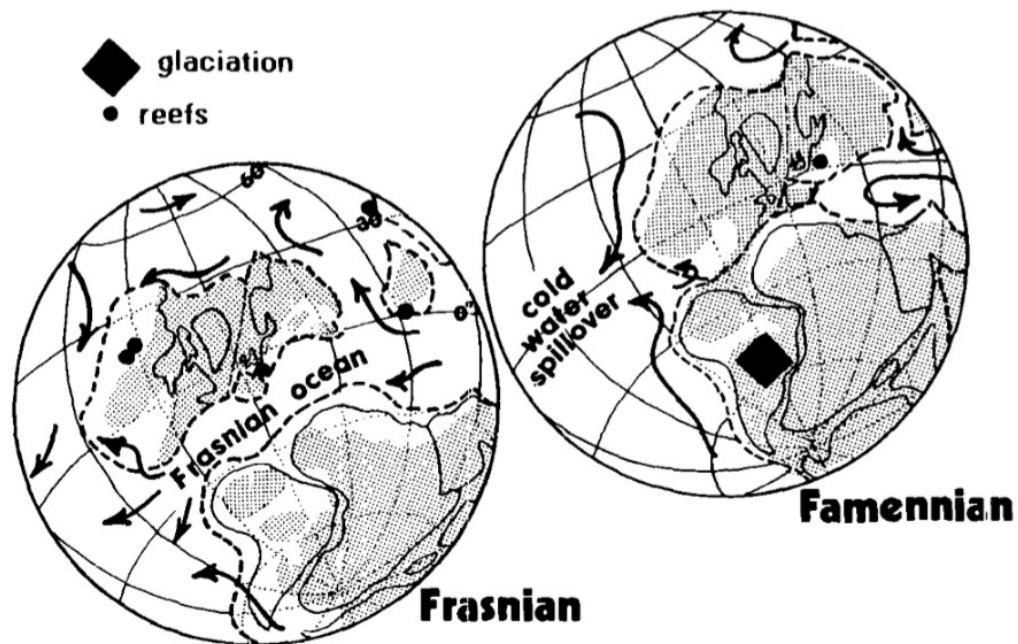


Fig. 1.5: Devonian reconstructions showing the deflected cold-water currents thought to have triggered climate change. From Copper (1986).

When going as far back in time as the mid-Paleozoic, the subduction and destruction of oceanic lithosphere make it impossible to directly study the deep-sea environment from direct geological data (Pohl et al., 2016). Circulation within the deeper parts of the ocean basin must be inferred, through for example schematic or numerical ocean circulation models. Including the reconstruction that motivated this study by Paproth et al. (1986) (Fig. 1.4), schematic Rheic reconstructions have been available for several decades. Fig. 1.6 shows an example of a more recent published circulation reconstruction for the Rheic Ocean by Dopieralska (2009). With regards to numerical ocean circulation models, however, available numerical models are presently only available for smaller oceanic basins. These scarce number of mid-Paleozoic numerical model studies have been particularly focused on the importance of tides on ancient epeiric seas (Slingerland, 1986; Wells et al., 2005).

Numerical models could provide valuable information with regards to current paleogeographic controversies. They can also give an additional perspective on schematic circulation models.

Despite their usefulness, implementation of global numerical models is thus far lacking in mid-Paleozoic research.

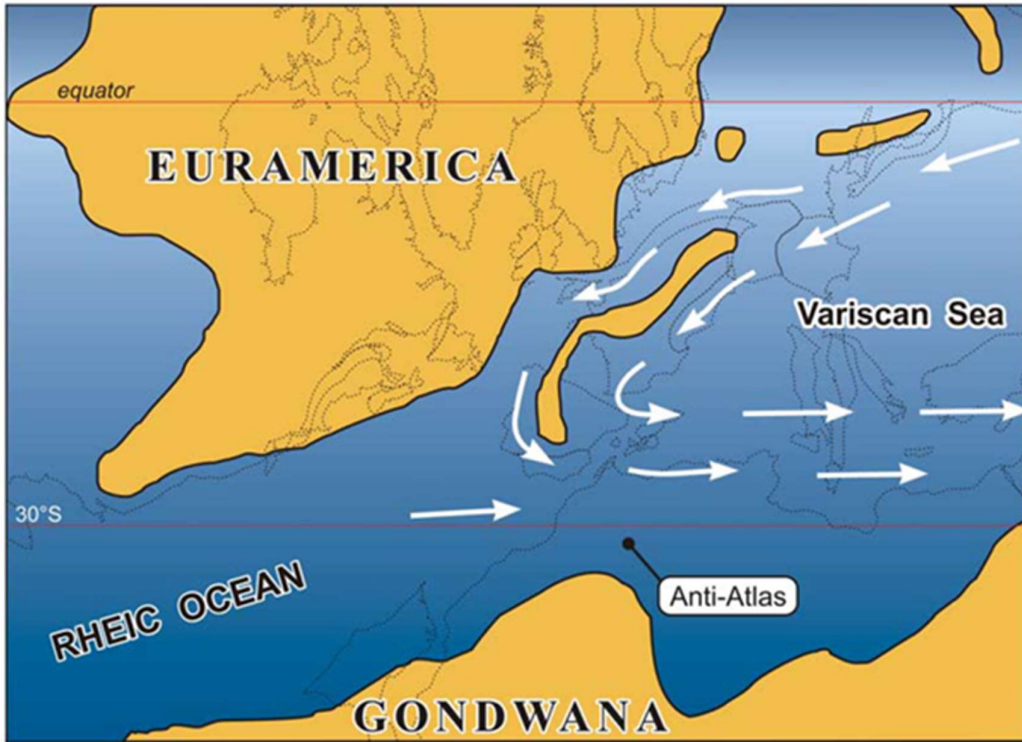


Fig. 1.6: Schematic oceanic circulation reconstruction showing the main Devonian currents in the Rheic Ocean, by Dopieralska (2009).

1.2 Objective and research questions

In this study, numerical modelling will be used as a tool for testing the assumption that oceanic circulation in the past was governed by the same oceanographic principles as today (Servais et al., 2014). To do so, the Rheic circulation patterns shown in schematic reconstructions will be compared to those obtained through the numerical model used in this study. In addition, the study is aimed at determining whether the model can contribute to the debate on several paleogeographic aspects in the region of the Rheic Ocean during the mid-Paleozoic.

The aim of this study is, therefore, to construct a numerical ocean model to answer the following research questions:

1. How do the surface circulation patterns generated with the numerical model in this study compare to the surface circulation patterns shown in schematic reconstructions?
 - Can the occurrence of a WBC by Paproth et al. (1986) be verified?
2. How can the model provide valuable information to contribute to the paleogeographic debates surrounding the Rheic Ocean?
 - Can the model be used to help determine the presence of peri-Gondwanan terranes?
 - Can the results help constrain other paleogeographic issues such as the position of Gondwana and timing of Rheic closure?

2 BACKGROUND

2.1 History of the Rheic Ocean

The opening of the Rheic Ocean was an important event in the Paleozoic and its closure was one of the main contributing factors leading to the formation of the supercontinent Pangea. Despite it leaving behind a more than 10,000 km long suture zone from Mexico to Poland (see Fig. 2.1), many aspects of its existence remain uncertain (Nance et al., 2010).

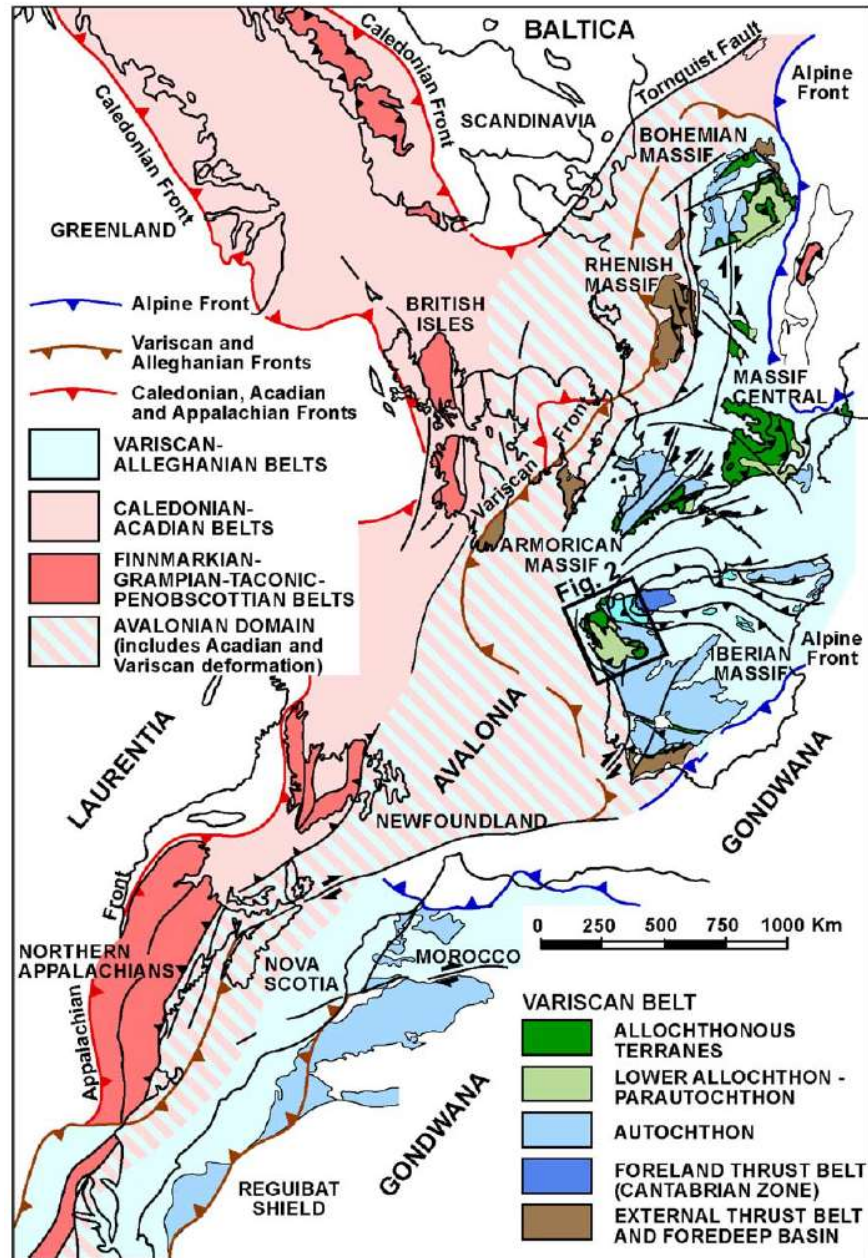


Fig. 2.1: Illustration of the Paleozoic orogenic belts related to the closure of the Rheic Ocean (Martínez Catalán et al., 2009).

Research regarding aspects of Rheic Ocean geodynamics has been ongoing for approximately three decades. Less in America -where the Rheic suture lacks exposure- and more so in Europe through detailed work by for example Franke (1989) as shown in Fig. 2.2 (Matthews et al., 2016; Nance, 2010; von Raumer et al., 2017). Research, however, is challenged by the large gap in time which has caused much of its lithosphere to be destroyed through subduction and obduction, consequently leading to relatively scarce paleomagnetic, lithological and paleobiogeographic data. An added complication comes from the tectonic complexity involved in the Rheic closure that resulted in the Variscan-Appalachian-Alleghanian orogen and is thought to have formed from the collision of a multitude of often indiscernible terranes. An example of the difficulty that accompanies Rheic tectonic research is the intricate structure of the Variscides in Europe which, as one of the most well-studied sections of this wide orogen, has been described by Torsvik and Cocks (2016) as a “messy series of events”.

All in all, the lack of consensus on the various aspects of Rheic Ocean formation, evolution and closure has led to several, in some cases contrasting, tectonic models and paleogeographic reconstructions. The following section will be aimed at giving an overview of the events leading to Rheic formation, evolution, and closure.

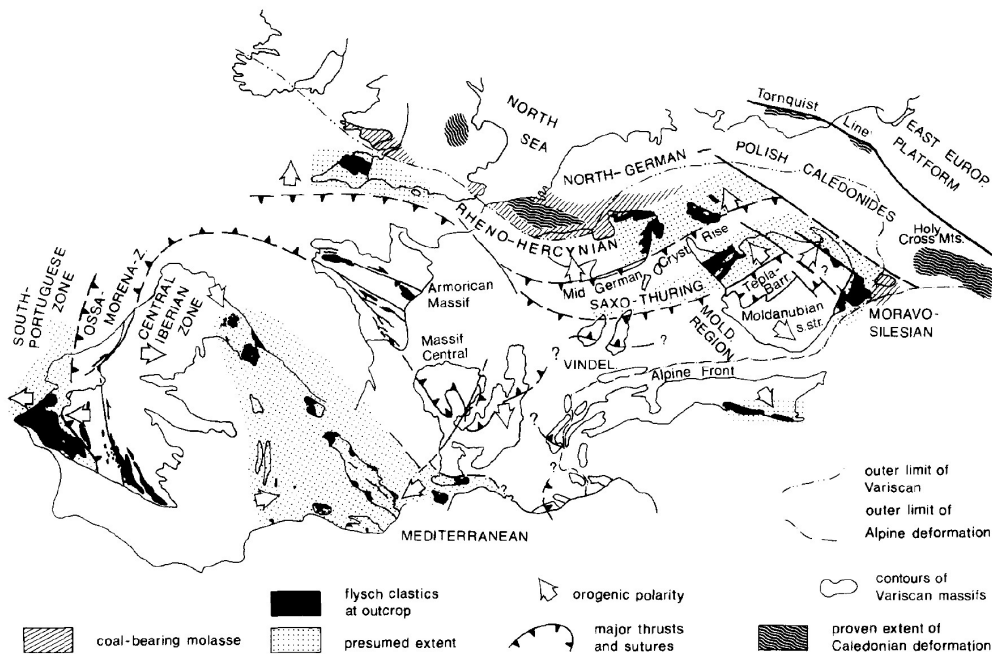


Fig. 2.2: Diagram by Franke (1989) showing the main structural elements of the Variscan belt.

2.1.1 Geodynamic scenario

The plate tectonics involved in the formation and closure of the Rheic have been integral to Variscan, Appalachian, and Alleghanian based research for decades which has resulted in numerous tectonic models describing the possible mechanisms. Although it is important to understand the tectonic interplay when carrying out an in-depth study on the Rheic Ocean, it is beyond the scope of this study to discuss all available models and contrasting ideas. This section will, therefore, be limited to giving a general overview of the main geodynamic events that were involved in the evolution of the Rheic ocean. For discussions on several tectonic models, you are

instead referred to the reviews and discussions in for example Murphy (2010), Pereira et al., (2017), Shail and Leveridge (2009) and Blakey (2008).

The global configuration of the Early Paleozoic constituted three major continents: Laurentia, Baltica, and Gondwana (Servais and Sintubin, 2009) (see Fig. 2.3). Laurentia was comprised of modern-day Northern and Central America, Greenland, and the northern British Isles. It was separated from Baltica by the Iapetus Ocean. Baltica comprised modern-day Southern Britain, North-Central Europe up to the Urals, and Scandinavia. Baltica, in turn, was separated from Gondwana by the Tornquist Ocean which is sometimes considered the eastern arm of the Iapetus Ocean (Murphy et al., 2010). Gondwana was the largest continent at the time and constituted of South America, Africa, Antarctica, Australia, India, Arabia and Iran (Dopieralska, 2003).

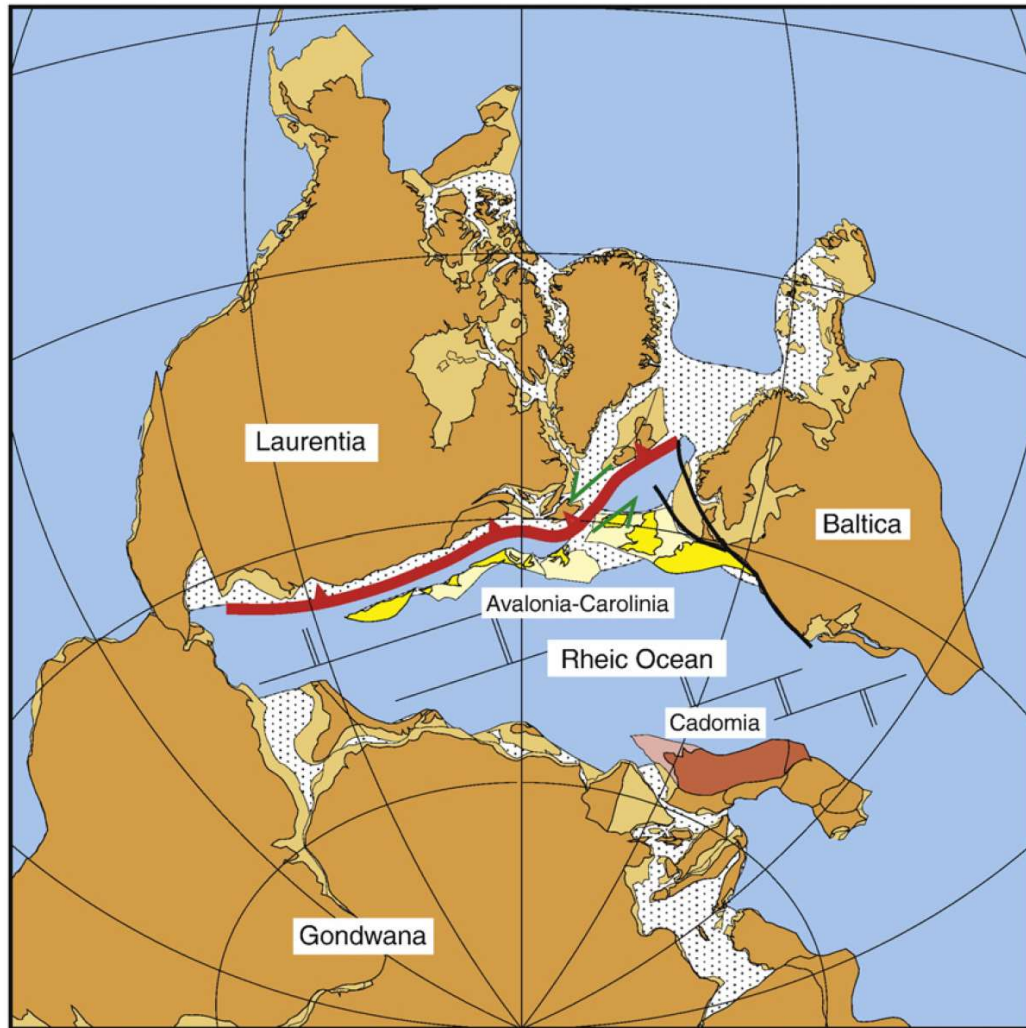


Fig. 2.3: Reconstruction of the paleogeographic configuration of the Rhenish Ocean during the Silurian, showing the main continental units involved (Nance et al., 2010).

It is thought that subduction and related extension at the northern Gondwanan margin in the Paleozoic caused several terranes to rift along a previous Neoproterozoic suture (Golonka and Gaweda, 2012; Murphy et al., 2010; Nance et al., 2010). This group of “peri-Gondwanan” terranes included terranes such as Ganderia, Carolina, Hunia, and Meguma in addition to a larger Avalonian terrane as described in the publications by Stampfli et al. (2013) and van Staal, Barr,

and Murphy (2012). These terranes, however, are often treated as one large group of terranes termed simply Avalonia or Avalonia-Carolinia as in Fig. 2.3.

The Rheic Ocean formed as a result of the final separation of Avalonia from the Gondwanan margin. The mechanism and exact timing of formation remain unclear, but in general its opening is interpreted to have occurred sometime between the Middle Cambrian and Middle Ordovician (Arenas et al., 2014; Linnemann et al., 2007; Murphy et al., 2010; Ribeiro et al., 2007; von Raumer and Stampfli, 2008).

The Rheic kept widening as Avalonia continued drifting northwards towards Laurentia and Baltica, up until the collision of Avalonia first with Baltica and ultimately with Laurentia. Their amalgamation formed the northern supercontinent Laurussia and closed the Iapetus and Tornquist Oceans between them, resulting in the Appalachian-Caledonian orogeny (red area in Fig. 2.4). After assembly of Laurussia, Gondwana began moving northwards towards Laurussia, eventually leading to the closure of the Rheic Ocean and subsequently forming Pangea. At the end of the Paleozoic, Pangea was surrounded by the Panthalassa ocean to its west and the smaller Paleotethys ocean to its east.

The entire process of Rheic closure depends on the tectonic model and has been divided into three categories by Murphy et al. (2010), namely favouring 1) subduction under Laurussia, 2) subduction under Gondwana or 3) bipolar subduction underneath both Laurussia to the north and Gondwana to the south (Pereira et al., 2017). Its closure is nonetheless generally perceived to have been diachronous, starting from the west and ending in the east, and closure times differed from one end of the ocean to another (Murphy et al., 2010; Nance et al., 2010). It is thought to have fully closed as early as the Silurian and as late as the Carboniferous, leaving behind the largest Paleozoic orogen in its wake (black shaded area in Fig. 2.4) (Eckelmann et al., 2014; Franke, 2006; Nance et al., 2010; Tait et al., 2000).

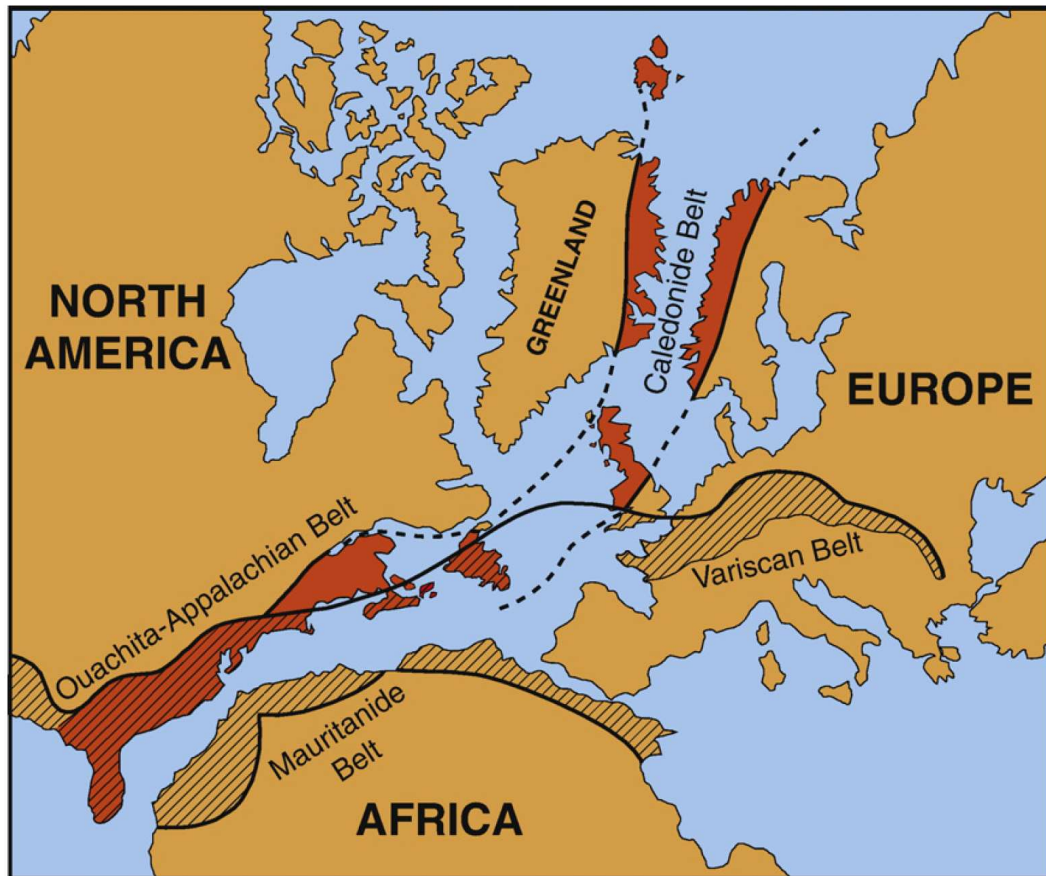


Fig. 2.4: Conceptual representation of the orogenic belts that resulted from Iapetus closure (red) and Rheic closure (black) (Nance et al., 2010).

2.2 Main paleogeographic controversies

This section will be dedicated to highlighting the main differences between the currently available mid-Paleozoic reconstructions. In general, the wide range of paleogeographic reconstructions results from the ambiguity of Rheic paleobiogeographic, paleomagnetic and lithological data (Dopieralska, 2003). These inconsistent reconstructions, in turn, lead to contradicting factors necessary for modelling paleoceanographic circulation patterns, such as Rheic widths and land-sea distributions.

One problem when comparing mid-Paleozoic reconstructions is that they are shown with different projections. Because of this issue, Dopieralska (2003) has taken several published reconstructions and re-projected them using Schmidt's projection, as shown in Fig. 2.5. In general, the differences between the reconstructions can be brought down to two main issues which can also be observed in Fig. 2.5, namely: 1) there is uncertainty regarding the terranes that rifted off northern Gondwana and amalgamated to Laurussia (brown terranes in Fig. 2.5), which results in a controversial number of oceanic basins, and 2) the paleoposition of Gondwana is poorly constrained which leads to different Rheic widths. These issues will be discussed in the following sections.

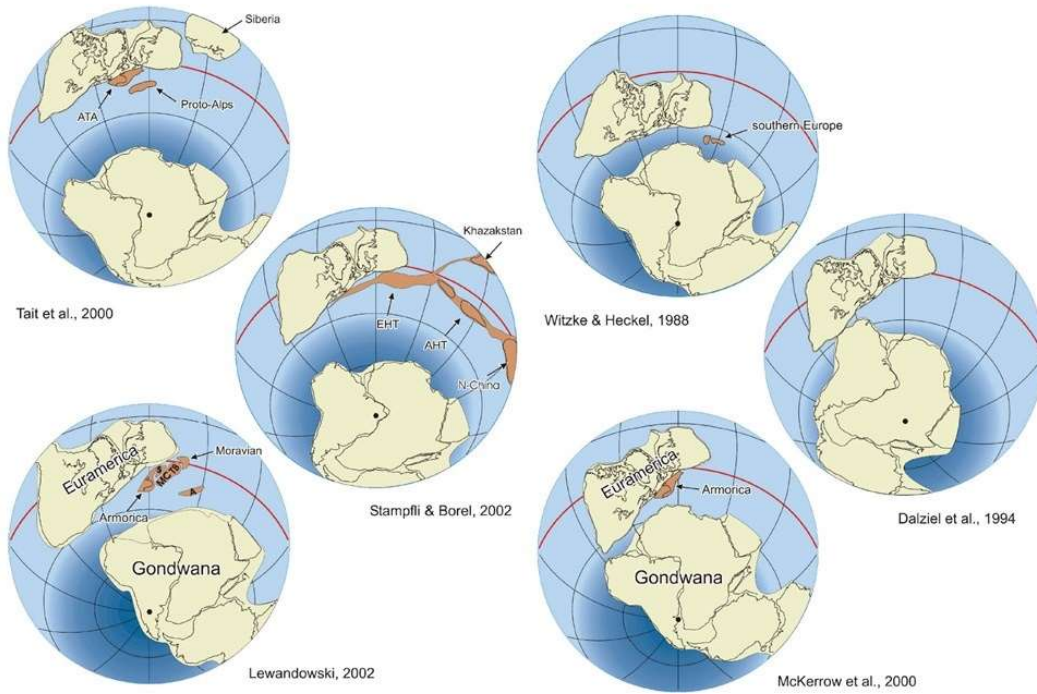


Fig. 2.5: Reconstructions available from six different sources in literature are re-projected with Schmidt's projection for all (Dopieralska, 2003).

1. Number of peri-Gondwanan terranes and oceanic basins

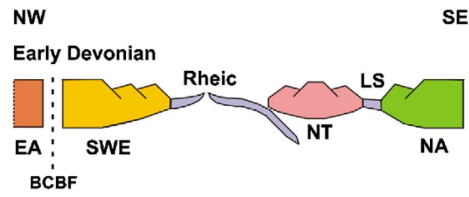
There is little consensus on how many peri-Gondwanan terranes rifted off the northern margin of Gondwana after the separation of Avalonia in the early Paleozoic. This includes uncertainty about the associated mechanism as well as the timing of rifting and their amalgamation to the Laurussian continent. “One-ocean” models, for example, do not incorporate oceanic back-arc basins off the coast of southern Laurussia or any smaller ocean basins between terranes located within the space separating Gondwana and Laurussia. These models, therefore, represent this area with solely one large Rheic Ocean, whilst other schools of thought dismiss the idea of having only one ocean (Franke, Cocks, and Torsvik, 2017). The total number of oceans between the Avalonian margin of Laurussia and Gondwana has insofar been interpreted to have been anywhere from one to five, as seen in Table 2-1 below. In this table, the total number of oceans specifically refers to all the potential mid-Paleozoic oceans in the region between Gondwana and the Avalonian segment of Laurussia and does not include the Iapetus, Tornquist or Panthalassa oceans. This categorization is therefore not consistent with Murphy et al. (2010).

Table 2-1: Overview of the inconsistent number of mid-Paleozoic oceanic domains between Laurussia and Gondwana as referred to in literature.

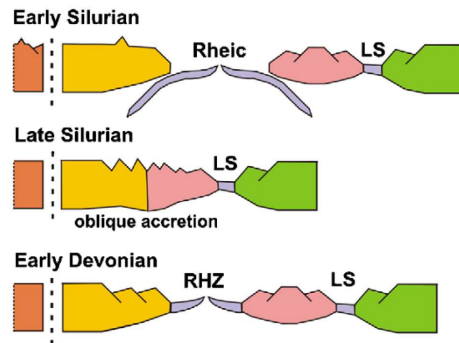
Nr. of oceans	Publication	Peri-Gondwanan terranes	Listed oceans
1	Nance et al. (2010)	Avalonia-Carolinia-Ganderia, Meguma, Cadomia (remained attached to Gondwana)	Rheic Ocean
1	Domeier (2016)	Ganderia-West Avalonia-East Avalonia-Carolinia, possibly Meguma, Cuyania	Rheic (including Themis and Ran branches)
2	Tait et al. (2000)	Avalonia, Proto-alps/alpine terranes, ATA	Rheic Ocean, Paleotethys Ocean
2	Torsvik et al. (2012)	Avalonia, Armorican Terrane Assemblage (ATA)	Rheic Ocean, Paleotethys Ocean
2	Kroner & Romer (2013)	Avalonia, South China terrane, Armorican Spur (remained attached to Gondwana)	Rheic, Paleotethys
2	Franke & Dulce (2016)	Avalonia, ATA	Rheic, Rhenohercynian Ocean
3	Huneke (2006)	Avalonia, ATA, Noric terrane (both remained adjacent to Gondwana)	Proto-atlantic (Rheic), Proto-tethys (Paleotethys), Rhenohercynian
3	Dopieralska (2009)	Avalonia, ATA	Rheic, Paleotethys, Variscan Sea
3	Golonka & Gaweda (2012)	Avalonia, Cadomia	Rheic, Paleotethys, Lizard-Giessen Ocean
3	Stampfli et al. (2013)	Ganderia-Avalonia-Hunua, Galatia, Hanseatic, Cadomia (remained attached to Gondwana)	Rheic, Paleotethys, Rhenohercynian
3	Eckelmann et al. (2014)	North Avalonia, South Avalonia, ATA	Rheic, Paleotethys, Rhenohercynian
3	Torsvik & Cocks (2017)	Avalonia, Armorican Terrane Assemblage (Armorica, Iberia, Saxothuringia, and Bohemia), Tisia Terrane	Rheic Ocean, Saxothuringian Ocean, Paleotethys Ocean (including Galicia-Moldanubian which forms its western arm)
4	Matte (2001)	Avalonia, Armorica microplate	Rheic, Paleotethys, Rhenohercynian, Galicia-Brittany Ocean
4	Alexander et al. (2019)	Avalonia, SW England, Armorica, Normannia	North Rheic, Central Rheic, South Rheic, Rhenohercynian
5	van Staal et al. (2012, 2009)	Ganderia-Carolinia, Avalonia, Meguma	Rheic, Acadian Seaway, Taconic Seaway, Neocadian seaway?, Salinic seaway?
5	Franke et al. (2017)	Avalonia, North Armorica, South Armorica, Paleo-Adria	Rheic, Paleotethys, Rhenohercynian, Saxo-Thuringian Ocean, Galicia-Moldanubian Ocean

As can be seen in Table 2-1, the existence of the Rheohercynian Ocean as a separate oceanic basin is not as widely accepted as that of the Rheic and Paleotethys oceans. Additionally, there is no general agreement on whether it was a successor or a marginal basin, and therefore whether it was contemporaneous with the Rheic Ocean or not (Shail and Leveridge, 2009). An overview of the three main theories regarding the Rheohercynian Ocean is shown in Fig. 2.6. These discrepancies regarding the Rheohercynian Ocean caused the focus of this study to be shifted towards a much larger scale, namely the larger Rheic Ocean between Gondwana and Laurussia, which is the only ocean wide enough to be recorded by biogeographic and paleomagnetic data (Franke and Dulce, 2017).

(A) RHZ is N margin of Rheic Ocean

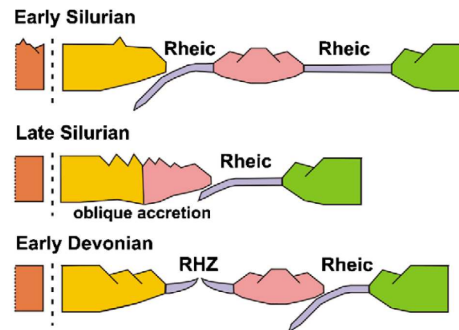


(B) RHZ is successor basin to Rheic Ocean

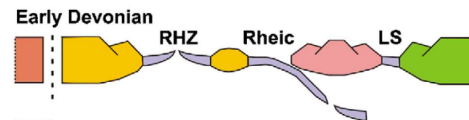


(C) RHZ is marginal basin to Rheic Ocean

(1) Rifting after accretion of NT to EA



(2) Rifting of EA after Rheic ridge subduction



KEY
 EA: Eastern Avalonia; BCBF: Bristol Channel-Bray Fault
 SWE: SW England; NT: Normannian Terrane; LS Léon Sea
 NA: North Armorica

Fig. 2.6: Illustration by Shail and Leveridge (2009) showing several ways in which the Rhenohercynian Ocean (RHZ) could relate to the Rheic Ocean.

Table 2-1 also shows the large number of peri-Gondwanan terranes that might have possibly existed within the Rheic. It is between these terranes that the smaller ocean basins are thought to have formed, as shown in Fig. 2.7. One of the terranes is called the Armorican Terrane Assemblage (ATA) which is in fact thought to be a group of smaller terranes including the Iberian Peninsula, Armorica, and Bohemia. The ATA serves as an example of the uncertainty regarding the peri-Gondwanan terranes as, despite having been the subject of research for over three decades, it remains debated and is continually being redefined. Uncertainties not only include its position, but also which minor terranes it was made of and whether it remained attached to Gondwana or not (Franke et al., 2017; Linnemann et al., 2007; Matte, 2001; Morzadec et al. 1988; Servais and Sintubin, 2009; Torsvik and Cocks, 2016).

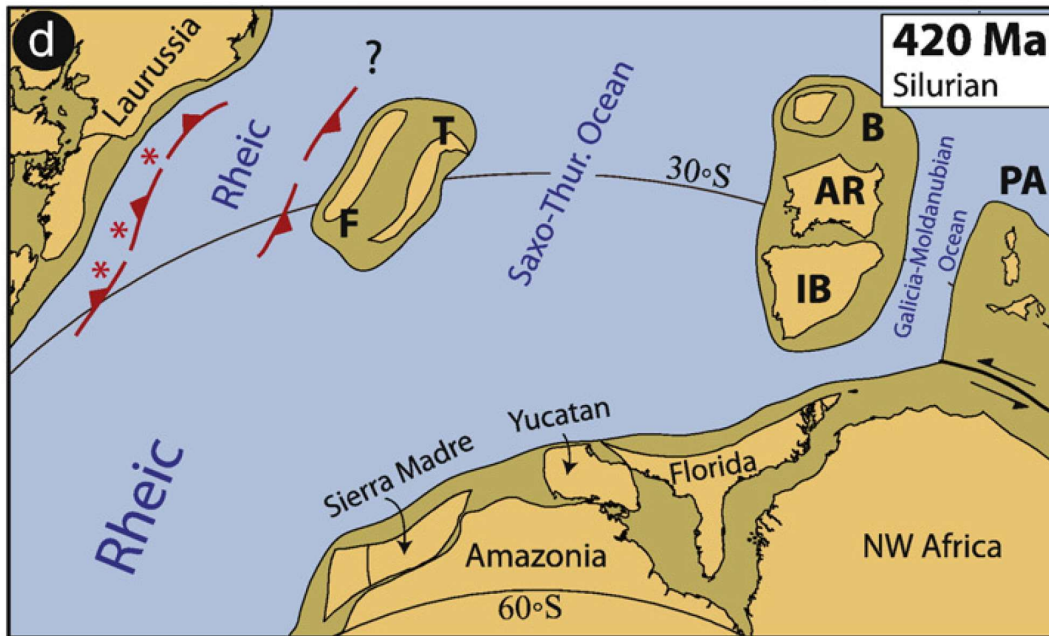


Fig. 2.7: Example of a reconstruction that includes multiple peri-Gondwanan terranes and associated oceans. Terranes include Franconia (F), Thuringia (T), Iberian Peninsula (IB), Armorica (AR), Bohemia (B), and Paleo-Adria (PA). Modified from Franke et al. (2017).

2. Contradicting positions of Gondwana

The paleogeographic position of Gondwana is, in contrast to Laurussia, difficult to ascertain, which is a problem when modelling the Rheic Ocean as its width depends on the position of Gondwana in relation to Laurussia. This has led to various interpretations of the full width of the Rheic Ocean basin, as well as the timing of closure of the basin due to the amalgamation of Gondwana to Laurussia. The inconsistency in the Gondwanan position used in reconstructions has two main reasons. Firstly, little paleomagnetic constraint exists for the Late Devonian, which makes different Gondwanan apparent polar wander paths (APWPs) possible. The net northward movement of Gondwana throughout this period could, for example, have been achieved by a quick northward and then southward movement, or by a gradual northward movement according to Tait et al. (2000) (Fig. 2.8).

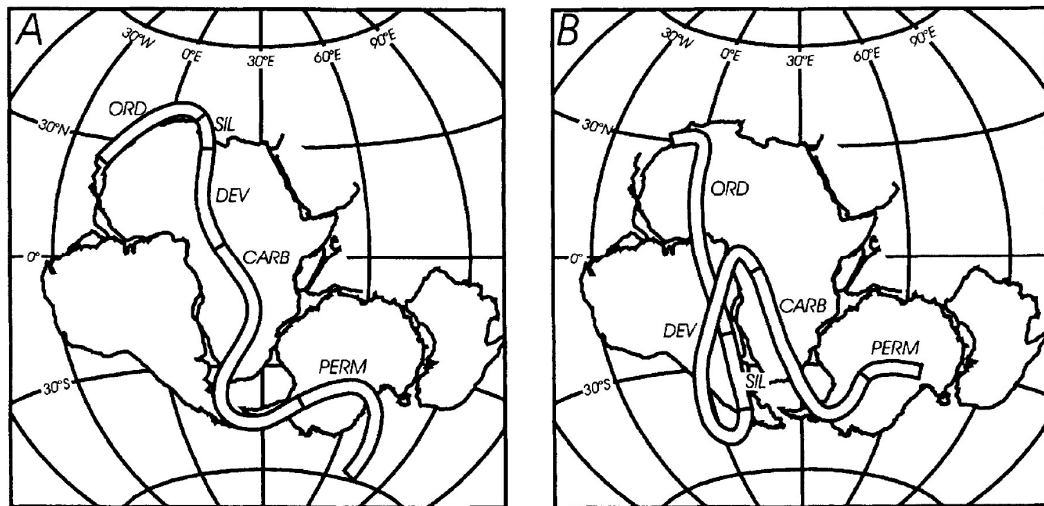


Fig. 2.8: Alternative APW curves for Gondwana in Paleozoic showing the a) gradual northward movement or b) rapid northward and then southward movement. Image from Tait et al. (2000).

The second reason for the contrasting Gondwanan positions in literature is that different assumptions about the Earth's magnetic field lead to different plate configurations (Torsvik and Cocks, 2004). Treating the magnetic field as a ge axial dipole field has led to configurations in which South America is adjacent to Europe prior to its collision with Laurussia in the Carboniferous, which is termed "Pangea-C" (Fig. 2.9 on the left). Treating the magnetic field as a more complex field with a non-dipole component results in a reconstruction in which South America is close to North America instead of Europe, termed "Pangea-A" or "Wegenerian Pangea" (Kroner and Romer, 2013) (Fig. 2.9 on the right). Reconstructions by Torsvik et al. (2012), on which this study bases its paleogeography, follow a Pangea-C configuration. Pangea-A, on the other hand, is the preferred configuration when combined with structural geology or paleontology (Torsvik and Cocks, 2004). This is the case for the early schematic reconstruction by Kiessling et al. (1999) on which reconstructions by Copper (2002) and Hüneke (2006) are based. The difference between the reconstructions translates to a difference in Gondwanan position of 6000 km (Torsvik and Cocks, 2004), demonstrated by the arrow in Fig. 2.9a.

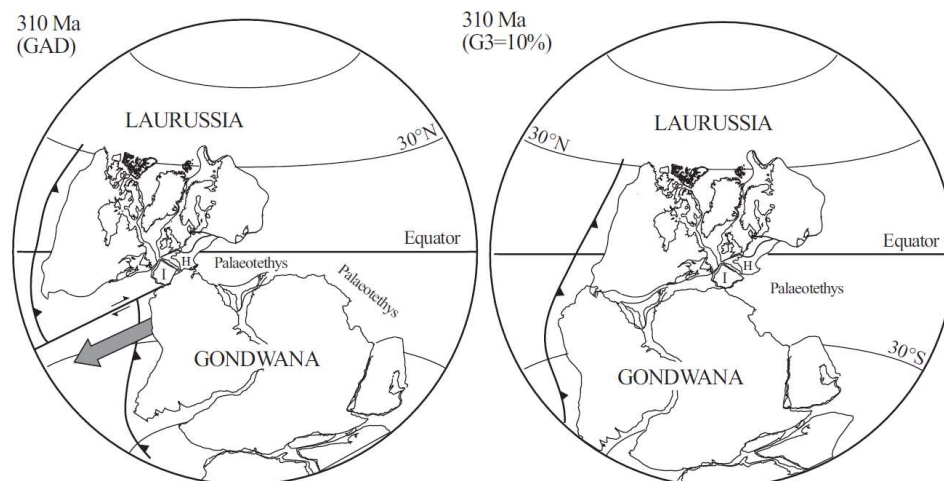


Fig. 2.9: Diagram representing the differences between the Pangea-C configuration (left) and Pangea-A configuration (right) (Torsvik and Cocks, 2004).

2.3 Rheic paleoceanography and climate

The reconstruction by Eckelmann et al. (2014) in Fig. 2.10 shows how the Rheic Ocean is located in the Southern Hemisphere, between the Pethalassic and Paleotethys Oceans. Its position between the equator and highlatitudes places it in the tropical wind belt of a modern Hadley cell (Paproth et al., 1986) and is thought to have allowed equatorial waters to flow between the western Panthalassic and eastern Paleotethys ocean (Gerhard et al., 2001, p. 41).

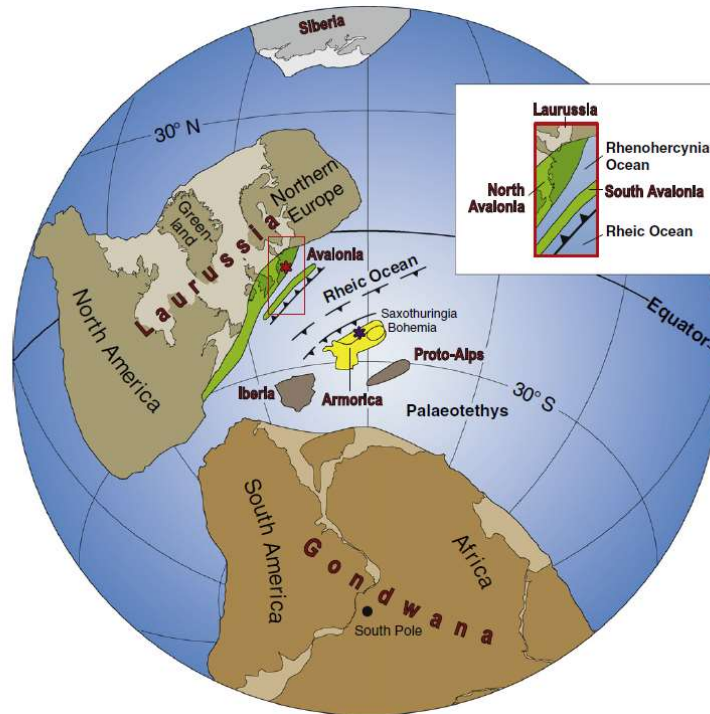


Fig. 2.10: Late Devonian to Early Carboniferous paleogeographic reconstruction by (Eckelmann et al., 2014).

As previously mentioned, the Rheic Ocean dimensions remain an enigma: according to some research groups, the Rheic would have reached a maximum width of more than 4000 km in the Silurian (Domeier, 2016; Nance et al., 2010), contrasting with a narrow Rheic shown in reconstructions by for example Copper (2002) and Hüneke (2006). Despite the uncertainty of its dimensions, paleobiogeographic and lithological evidence indicate wide, shallow shelves on both the active Laurussian and predominantly passive, Gondwanan margins (Arenas et al., 2014; Dopieralska, 2009; Jakubowicz et al., 2019; von Raumer et al., 2017). The stromatoporoid reefs on these shelves are indicative of the Devonian period and reached unusually high paleolatitudes, which is thought to have been possible due to the closed character of the Rheic Ocean (Jakubowicz et al., 2019).

Regarding mid-Paleozoic climate, research by De Vleeschouwer et al. (2014) indicates a cyclic climate which was variable, and tropical storms such as monsoons were frequent during the Devonian greenhouse climate (Lash, 2016). This greenhouse climate is also thought to have caused a more stable oceanic thermohaline stratification than compared to the present day (Copper, 2002; Hüneke, 2006).

2.3.1 Available mid-Paleozoic schematic reconstructions

Schematic reconstructions use features of the idealized steady-state ocean circulation to deduce the near-surface currents in a paleo-oceanic setting such as the Rheic Ocean (Olbers, Willebrand, and Eden, 2012, p. 443). These large-scale circulation patterns are also observed in modern-day oceans. Fig. 2.11 shows how subtropical gyres and subpolar gyres occur at latitudes that are comparable to the mid-Paleozoic Rheic Ocean, between 0-70° south latitude, as indicated by the red box.

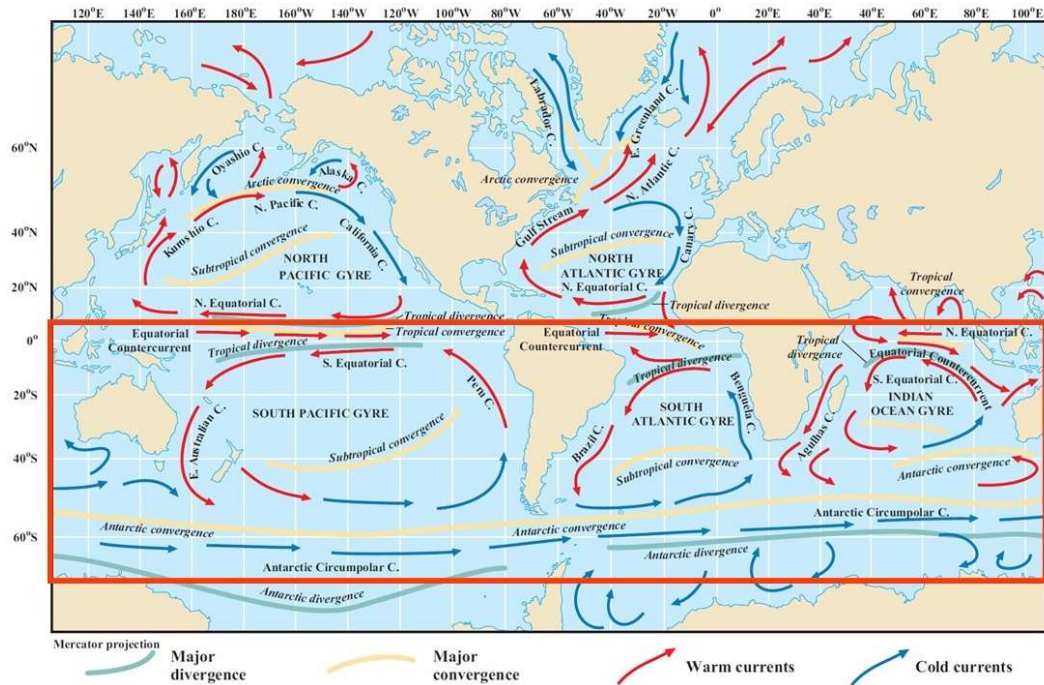


Fig. 2.11: Schematic overview of the present-day global wind-driven surface currents and outline (red box) of the latitudinal region that the Rheic Ocean would have occupied, modified from Segar (2018).

Several mid-Paleozoic schematic ocean circulation reconstructions have been published by for example Copper (2002), Dopieralska (2009), Hüneke (2006), and Jakubowicz et al. (2019). These reconstructions, however, are either based on earlier work by either Kiessling, Flügel, and Golonka, (1999) or Oczlon (1990). These two mid-Paleozoic schematic reconstructions are shown in Fig. 2.12 and Fig. 2.13 below.

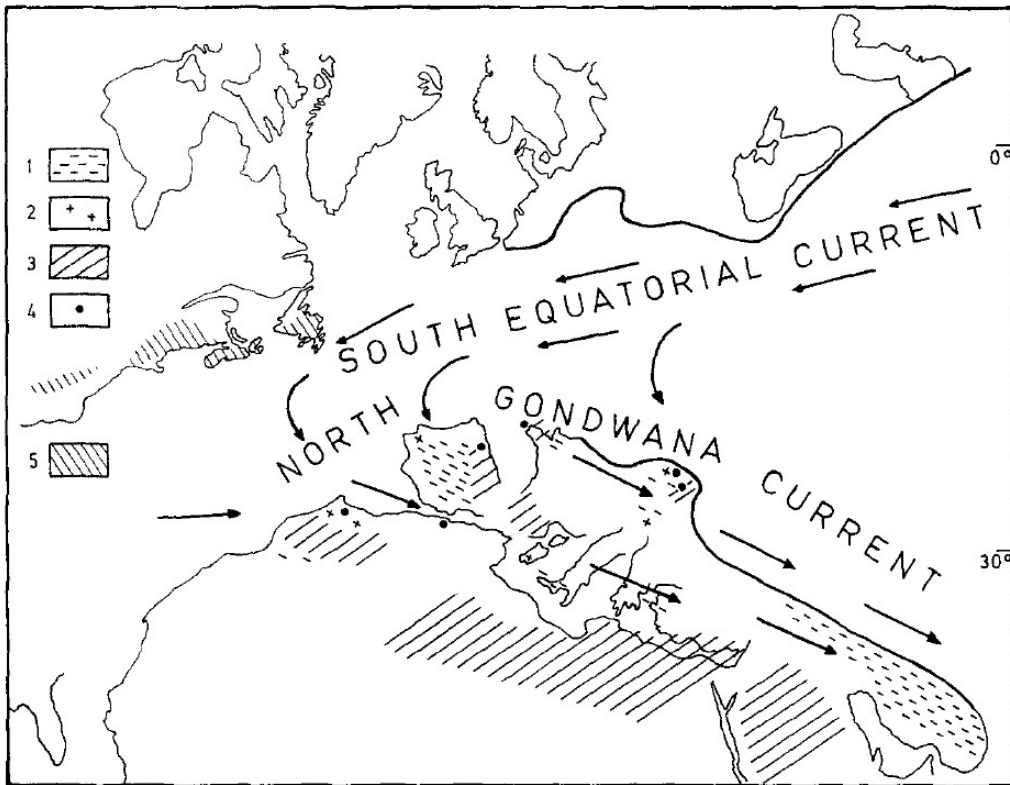


Fig. 2.12: Schematic reconstruction of the surface water circulation between Gondwana and Laurussia in the Middle Devonian (Oczlon, 1990).

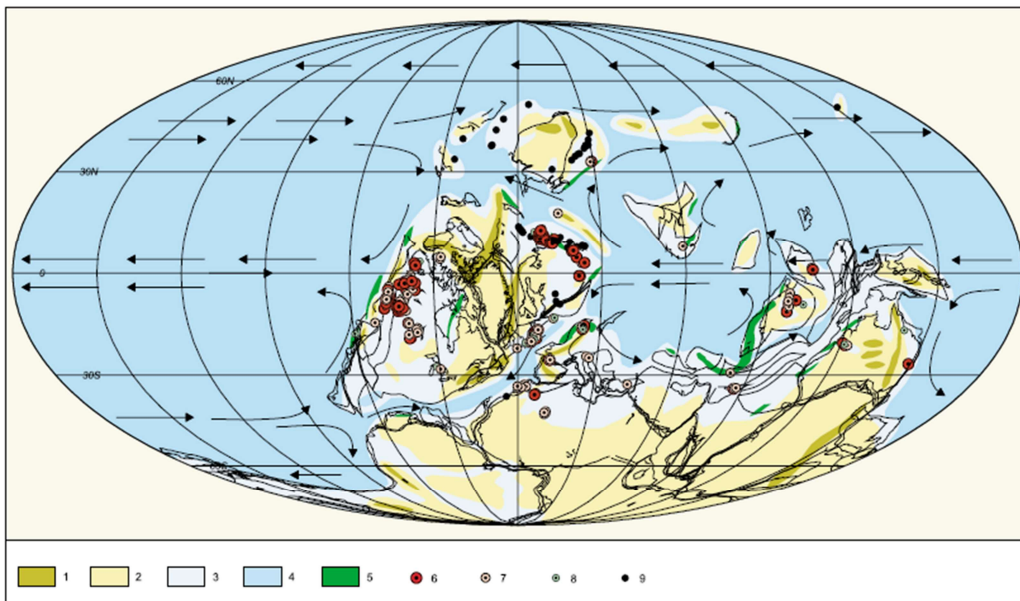


Fig. 2.13: Global Givetian-Frasnian ocean surface currents, reconstruction from Kiessling, Flügel, and Golonka (1999).

The main differences between the two reconstructions in Fig. 2.11 and Fig. 2.12 arise from the use of different projections and incorporation of contradictory positions of the Armorican Terrane Assemblage (ATA). Both reconstructions use the Pangea-A configuration where the African

section of Gondwana is close to central Europe as opposed to South America as in the Pangea-C configuration (see section 2.2). It should be noted that in both reconstructions the Rheic Ocean is represented as a narrow area between Laurussia and Gondwana. Similar circulation patterns are depicted in the reconstructions:

1.) Gyre patterns within the Rheic

Both reconstructions show the formation of large gyres. Large gyres exist on either side of the narrow Rheic Ocean in Fig. 2.13. The gyre connected to the eastern Paleotethys partly reaches into the Rheic area in Fig. 2.12, but is limited by the very narrow section of the Rheic and no gyre is shown to exist in the eastern area of the Rheic basin, only an eastward current enters from the Panthalassa Ocean.

2.) Current direction along the Laurussian shelf

A south-western current along the southern margin of Laurussia is referred to as the Western Boundary Current (WBC) in the publication by Paproth et al. (1986) in Fig. 1.4. It is also depicted in several reconstructions as a South Equatorial Current (Fig. 2.12).

3.) Current direction along the Gondwanan shelf

The reconstructions based on the one by Oczlon (1990) depict a current along the northern margin of Gondwana towards the southeast termed the North Gondwanan Current (Fig. 2.12).

4.) Interaction between the Rheic, Panthalassa and Paleotethys Oceans

The schematic reconstructions include the interaction between the Rheic and the Paleotethys to the east and the Panthalassa to the west. Fig. 2.12 and Fig. 2.13 depict a westward current that enters the Rheic from the eastern connection with what would have been the Paleotethys Ocean, and an eastward current entering the Rheic Ocean from the western connection with the Panthalassa Ocean, as seen in both the figures.

3 MODELLING APPROACH

3.1 Experimental setup

In this study, the Princeton Ocean Model (POM) was used to model a two-dimensional wind-driven circulation in a scenario representing the Rheic Ocean. Three known controls on surface currents were tested, namely the wind stress, paleogeography and Coriolis force (Hüneke, 2006).

The influence of paleogeography on the modelled oceanic circulation involves several factors, namely the distribution of land vs. sea (“land-sea distribution”), the influence of bathymetry, and throughflow. Experiments were dedicated to determining the effect on generated surface circulation patterns by a total of six different Rheic land-sea distributions, each distribution was based on a published paleogeographic reconstruction. With regards to the bathymetry, the majority of experiments were run with a uniform depth of 200 meters, but two experiments have been carried out with a variable bathymetry as well. A scenario representing the Tournaisian closure of the western arm of the Rheic Ocean basin was additionally tested. The paleogeographic experiments also included a scenario in which an open boundary with a net westward flow was implemented at both the eastern and the western Rheic boundary. This was aimed at testing the interaction between the Rheic and adjoining Panthalassa and Paleotethys Oceans.

The majority of the experiments were forced with an idealized wind stress, but several experiments were dedicated to testing the effect of wind stress on the modelled circulation as well. A total of three additional types of wind stress were used to force the model: a uniform zonal, meridional, and modern-day wind stress.

Lastly, the influence of the Coriolis force was tested by running the model with a Devonian Coriolis parameter value, a uniform value, or with a zero Coriolis effect, in addition to the modern-day Coriolis parameter value used in the land-sea distribution and wind-stress experiments.

3.2 Model configuration and input data

The Princeton Ocean Model (POM) is an open-source, numerical ocean model originally developed by Blumberg and Mellor (1987) applied in coastal and climate modelling as well as in global oceanic modelling. The model solves for the primitive equations through a finite-difference scheme. Its main features are its incorporation of turbulence through a turbulence closure scheme, optionable tidal simulation, a vertically implemented sigma coordinate system, and its mode-splitting technique (Ezer and Mellor, 2004).

The model configuration used in this study encompasses an oceanic basin of either variable or uniform depth in which horizontal water flow is forced by surface wind, other forcing parameters such as tides, and density gradients due to, for example, a variation in salinity and temperature are ignored. The model in this study uses a staggered, horizontal grid with a rectilinear coordinate system and a horizontal resolution of $1/4^\circ$. The vertical grid is divided into 16 sigma coordinate levels, a feature of POM which allows the model to better manage any steep topography (Ezer and Mellor, 2004). A total runtime of 150 days was used for all experiments, and the model was allowed to reach a steady-state after an initial ramping period of 7 days. The following sections describe some of the input data used, additional details for reproducing the experiments can be found in Appendix B.

3.2.1 Land-sea distributions

Six land-sea distributions are used in the model experiments which are based on paleogeographic reconstructions from several sources of literature. The shape of the Rheic basin (“sea”) and its surrounding continents (“land”) is referred to as the land-sea distribution. This distribution depends on the geological period of interest and associated paleogeographic reconstruction based on reconstructions from several literature sources. The study uses a total of six land-sea distributions, which are in turn combined with either of two bathymetric options: a uniform or a variable bathymetry. Section 2.2 highlights the wide range in mid-Paleozoic reconstructions; this study makes use of three different paleogeographic reconstructions that were found to be representative of the variety in the reconstructions. The main, standard reconstructions used throughout the study, including the reference experiment, are from Torsvik and Cocks (2016) and Torsvik et al. (2012) and are based on combined paleomagnetic and faunal data (Cocks and Torsvik, 2002; Domeier and Torsvik, 2014; Seton et al., 2012; Torsvik and Cocks, 2004). Two additional reconstructions were used to gain insight on the paleogeographic controversies. These were schematic ocean circulation models based on paleogeographic reconstructions from earlier publications. The reconstruction by Dopieralska (2009) is based on the paleogeographic reconstruction by Oczlon (1990) which in turn is based mainly on lithological data. The reconstruction by Hüneke (2006) is a slightly modified version of the paleogeographic reconstruction by (Kiessling et al., 1999), and is also based on mainly lithological data (reef distributions).

The paleogeographic reconstructions were reproduced on paleotectonic maps based on Torsvik et al. (2012), whose publication was one of the most up-to-date compilations of paleomagnetic data available at the start of this study. Paleopoles and rotation angles from Torsvik (pers.comm.) were used to rotate 9 main tectonic units bordering the Rheic ocean, namely the Greenland, North America, Eurasia, Amazonia, North-West Africa, North-East Africa, Iberia, Armorica, and Florida units (Torsvik and Cocks, 2016). These units were manipulated with open source software (GMT, n.d.) to their paleopositions at 400, 370, and 350 Ma using the respective rotation angles, resulting in identical positions to the original tectonic units in Torsvik et al. (2012). This is shown when the rotated units of this study (black) are overlain on the paleogeographic reconstructions (coloured) by Torsvik et al. (2012) as in figure Fig. 3.1. Although this study initially aimed to test the oceanic circulation pattern and especially the formation of a Western Boundary Current (WBC) in the Famennian as described by Paproth et al. (1986), the study incorporated the evolution of the Rheic by using land-sea distributions of three sequential epochs. The Emsian (400 Ma), Famennian (370 Ma) and Tournaisian (350 Ma) epochs were selected from the compilation by Torsvik et al. (2012) as they were found to be a good representation of the evolution of the Rheic Ocean; from its widest stage (Emsian) up to its closure (Tournaisian). The reference experiment was based on the Emsian distribution as this study is mainly focused on the Devonian, but the Famennian paleotectonic map could not be visually verified as it was not displayed in Torsvik et al. (2012), making the Emsian configuration the preferred option.

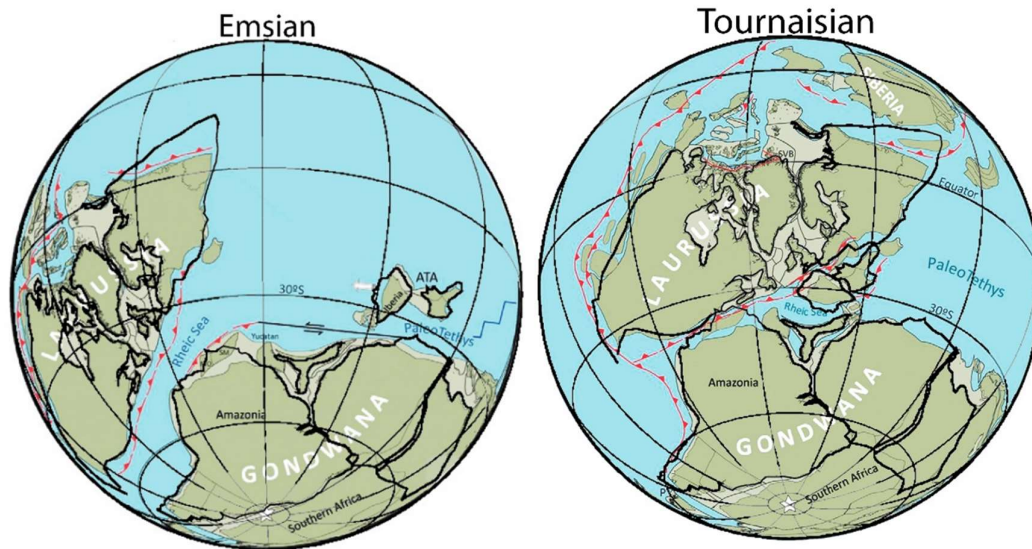


Fig. 3.1: Rotated continental units (black outline) overlain on paleogeographic reconstructions by Torsvik et al. (2012) shown in green and blue.

The continental units were rotated with GMT software in this study and were projected onto the coloured paleogeographic reconstructions by Torsvik et al. (2012) for comparison. The paleotectonic maps were then projected with an equidistant projection and clipped to the model domain. This model domain consists of an equidistant area of 60° by 60° encompassing the Rheic Ocean basin and its bordering continental margins as shown in Fig. 3.2. For an overview of all three model domains, the reader is referred to Appendix A. Although the total area of the model domain did not change per land-sea distribution, the centre of the Rheic Ocean was kept as the centre of each distribution, meaning that the latitude and longitude differed per epoch (see Table 3-1). Each land-sea distribution was then freehandedly drawn onto the paleotectonic map of its respective epoch using Grabit, a MATLAB program for extracting data points from image files (MathWorks, n.d.). The reconstructions by Torsvik et al. (2012) and Torsvik and Cocks (2017) were used as a basis for the masks of the Emsian (400 Ma) experiments, for one of the Famennian (370 Ma) experiments, and for the Tournaisian (350 Ma) experiment. The reconstructions by Dopieralska (2009) and Hüneke (2006) were used for the two remaining Famennian experiments. The reproduced land-sea distributions generally deviate slightly from the literature reconstructions due to a difference in map projection between the literature and model maps (see section 2.2). Additionally, part of some land-sea distributions had to be inferred as not all original paleogeographic reconstructions covered the full region of the model domain, namely those by Dopieralska (2009) and Torsvik and Cocks (2016). The longitudes in this study will be shown in images but further ignored as it is relative to the paleotectonic model used (Torsvik et al. 2012, 2008). Seeing as the study includes reconstructions by Dopieralska (2009) and Hüneke (2006) as well, longitudes are therefore not exact.

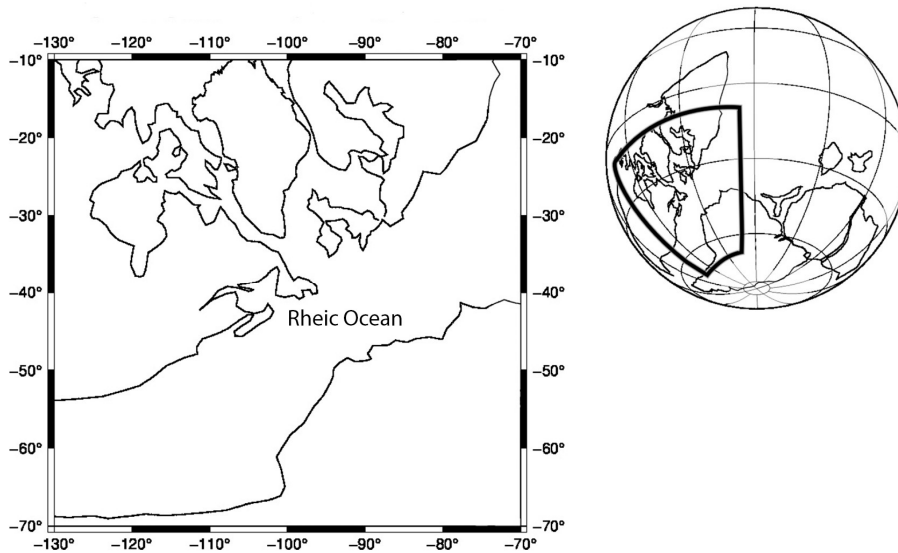


Fig. 3.2: Depiction of the model domain, in this case for the Emsian scenario. In an equidistant projection (left) and an orthographic (right) projection. Bold outline in the orthogonal projection represents the model domain.

Table 3-1: Information on the land-sea distributions used in the experiments

Model experiment name	Age (Ma)	Original paleogeographic reconstructions	Latitude range (°)	Longitude range (°)
Emsian reference experiment	400	Torsvik & Cocks (2017), figures 8.2, 8.5, 8.9	-10 to -70	-130 to -70
Emsian shelf break barrier experiment	400	Torsvik et al. (2012), figure 18	-10 to -70	-130 to -70
Famennian experiment (Torsvik)	370	Torsvik & Cocks (2017), figures 8.3, 8.6, 8.9	0 to -60	-110 to -50
Famennian experiment (Dopieralska)	370	Dopieralska (2009), figure 2	0 to -60	-110 to -50
Famennian experiment (Huneke)	370	Huneke (2006), figure 6	0 to -60	-110 to -50
Tournaisian experiment	350	Torsvik et al. (2012), figure 18	0 to -60	-75 to -15

3.2.2 Bathymetries

The model uses two different bathymetric depths: either a uniform depth of 200 metres or a generated bathymetry of depths that vary between 0 to 6000 meters. The basin was originally assumed to have been a shallow epicontinental sea as mentioned in research by Paproth et al. (1986). A depth of 200 metres was chosen to represent this shallow sea, a value also used by de la Vara and Meijer (2016).

Despite continued debate (see section 2.1), research from the past two past decade agrees that the Rheic ocean was not a shallow sea but in fact a major ocean with subduction zones leading to oceanic trenches and a back-arc basin at its northern margin with Laurussia, as shown in the tectonic models by Eckelmann et al. (2014). These tectonic models were further used to test the occurrence of the Rheohercynian Ocean that was shown in the paleogeographic reconstruction by Paproth et al. (1986) (Fig. 1.4). An alternative bathymetry was therefore tested which represented an ocean basin geometry consisting of a large subduction zone and a back-arc setting which represents the Rheohercynian Ocean, in the Rheohercynian zone, based on the geotectonic model by Eckelmann et al. (2014) (Fig. 3.3). The subduction zone trench was set to a depth 6000 metres and a depocenter behind the Rheohercynian island set to 3500m based on flysch sedimentation thickness data by Narkiewicz (2007). This alternative bathymetry was generated in GMT with the “surface” function, in which values vary between contour lines with a specified depth. These contour lines were digitized from the land-sea distributions with the use of Grabit and given depths between 0 and 6000 meters. The contour lines were additionally based on the concept of a wide, shallow Gondwanan and shallow, but narrower Laurussian shelf (Jakubowicz et al., 2019).

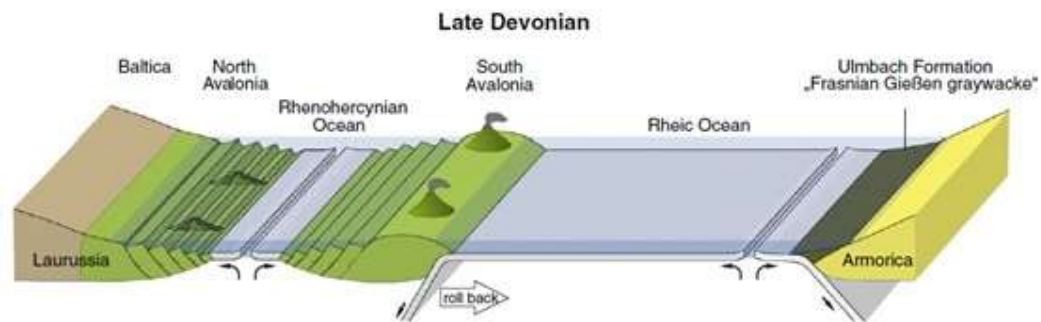


Fig. 3.3: Modified diagram of the geotectonic model by Eckelmann et al. (2014) on which the variable bathymetry was based.

3.2.3 Boundary Conditions

Surface boundary conditions in the model include a free surface condition in which the oceanic surface is not fixed. The lateral boundary conditions represent either an open or a closed ocean by regulating the flux at the eastern and western boundaries of the model domain. The open boundaries simulate flow through the basin by making use of an imposed net in- or outflow (Ezer and Mellor, 2004). This boundary condition allows a westward flux of either 1, 5, or 7 Sverdrup at both the eastern and western model boundaries, amounting to a net zero flux. The values for 1 and 5 Sverdrup are used in research by de la Vara and Meijer (2016) to represent a small net flow and large net flow, respectively. The Rheic Ocean in the study by Paproth et al. (1986) was set to a latitude between 10-15° south latitude, which was why the present-day water mass exchange was originally based on a modern-day analogue for those latitudes. This led to the use of the 7 Sverdrup value, as it is water mass exchange of the Timor Sea according to data from Cresswell et al. (1993).

3.2.4 Wind stress

The circulation in the model is driven by the surface wind which is applied as a wind stress. The wind stress is applied by ramping it over 7 days and dividing it by the density of seawater,

resulting in Nm/kg units rather than the standard wind stress unit N/m^2 found in literature. Eastward and northward wind stresses are expressed as negative values and are therefore opposite in sign to wind stress values found in literature. In this study, four different types of wind stress are implemented: uniform zonal and meridional wind stresses, averaged zonal wind stresses from satellite data, and idealized zonal wind stresses.

Uniform wind stress

The simplest wind stress applied to the model was a uniform wind stress independent of latitude, and was either zonal or meridional, depending on the experiment. A typical wind stress value for the mid-latitudes of 0.1 N m^{-2} , or -0.1 N m^{-2} as used in the model, was used for both zonal and meridional wind stress experiments (Mellor, 1996; Olbers et al., 2012, p. 432). This was applied to the model as shown in equations 3.1 and 3.2

$$wusurf = \frac{ramp * -0.1}{rhoref} \quad (3.1)$$

$$wvsurf = \frac{ramp * -0.1}{rhoref} \quad (3.2)$$

Where $wusurf$ is the zonal wind stress and $wvsurf$ the meridional wind stress, $rhoref$ is the assumed seawater density (1025 kg m^{-3}), and $ramp$ is a coefficient which represents an inertial ramp that gradually increases the wind stress value to its maximum value within a set amount of time, which in this study was set to 7 days:

$$\text{Ramp} = \text{time}/\text{period} \quad (3.3)$$

Where $time$ is the internal time step of the model and $period$ is represented by a number of days.

Observed wind stress

Modern-day zonal wind-stresses were taken from the NOAA Blended Sea Winds database (NOAA, 2015) (Fig. 3.4a). This 11-year (from 1995 to 2005) monthly climatological dataset containing ASCII data of global, multiple-satellite wind stresses needed to be further manipulated before incorporating it in the model. Firstly, the data was averaged over the total number of years, after which it was zonally averaged. Outliers were then taken out by removing any wind stresses above 0.2 N m^{-2} . The wind stresses in Fig. 3.4 represent the wind stress magnitudes as all values are positive and therefore do not include the wind stress directions.

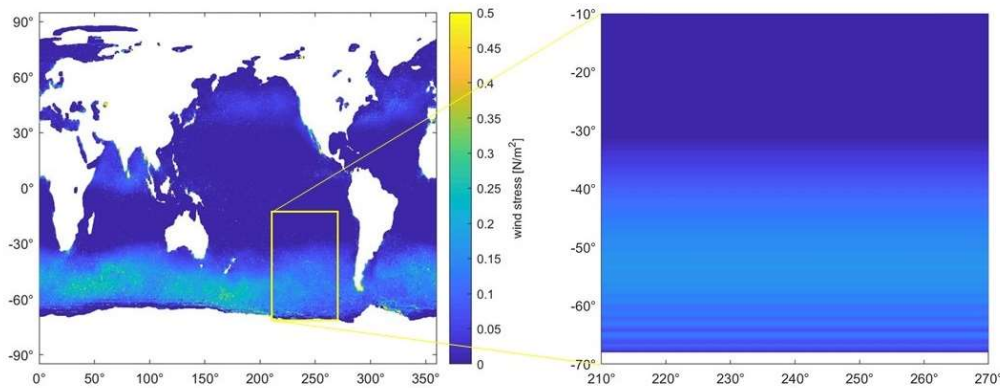


Fig. 3.4: Depiction of data from the NOAA Blended Sea Winds database showing a) the global wind stress magnitudes prior to manipulation and model domain outline and b) wind stress magnitudes within the model domain after manipulation.

Idealized wind stress function

The idealized wind stress function is the simplified form of the long term mean wind stress in an idealized global scenario with a flat-bottomed ocean (Mellor, 1996, p.89; Pond and Pickard, 2013, p.133). The distribution of the east-west component of the wind stress within a gyre is displayed in Fig. 3.5 below, showing that zonal wind stress varies sinusoidally with latitude.

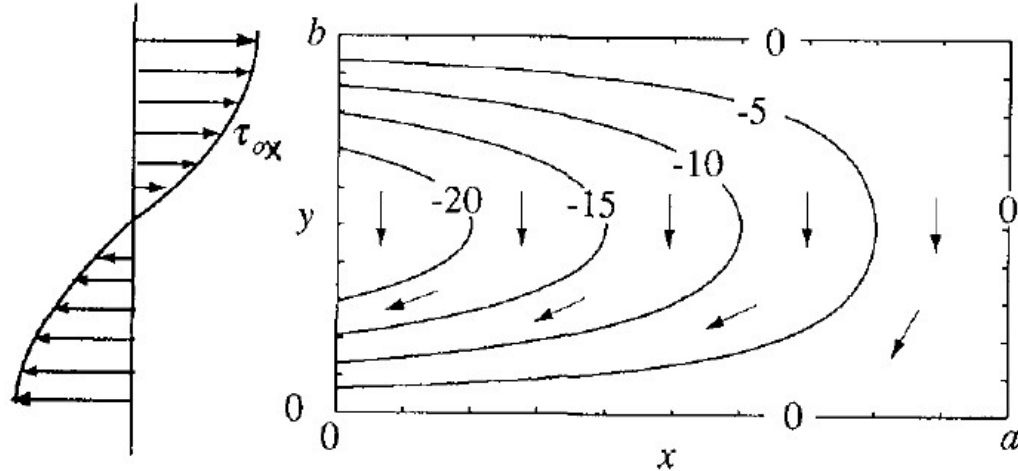


Fig. 3.5: Zonal wind stress represented as a function of latitude, y . Image from Mellor (1996).

From Fig. 3.5 it can be deduced that half a wave cycle represents one gyre. Assuming no doldrums exist in this simplified scenario (see Fig. 3.7) and taking the gyre in the image to be a subtropical gyre as an example, it would mean that half a wave cycle (= wavelength) spans a region of 0° to 60° latitude. Mellor (1996) described this sinusoidal curve with the following equation:

$$\tau_{0x} = -\tau_0 \cos\left(\frac{\pi y}{b}\right) \quad (3.3)$$

Where τ_0 is taken to be wind stress magnitude, y is the latitude (in radians) and b is half the period of variation (in radians), $\lambda/2$.

This translates to the following equation:

$$\tau_{0x} = -\tau_0 \cos\left(\frac{y}{\lambda} \cdot 2\pi\right) \quad (3.4)$$

Where τ_0 is taken to be wind stress magnitude, typically 0.1 N m^{-2} , and y is the latitude (in radians), and the wavelength λ is equal to $2/3\pi$.

This generates the cosine curve seen in Fig. 3.6.

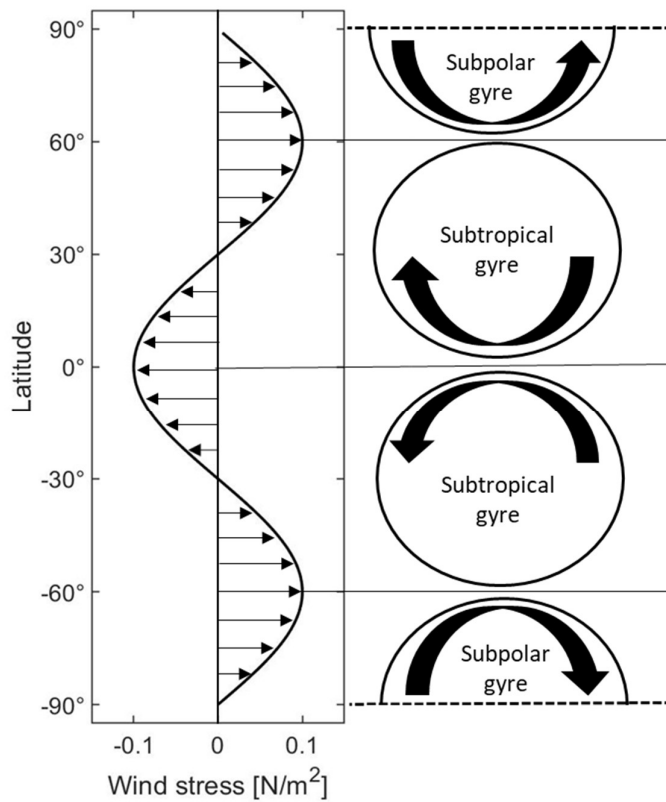


Fig. 3.6: Visualization of the idealized wind stress function.

Wind stress magnitude, however, is shown to vary with latitude as shown in Fig. 3.7. On average, these magnitudes vary between 0.1 N m^{-2} and 0.2 N m^{-2} stated by Olbers et al., (2012, p. 432), and suggest that the global wind stress function is asymmetric.

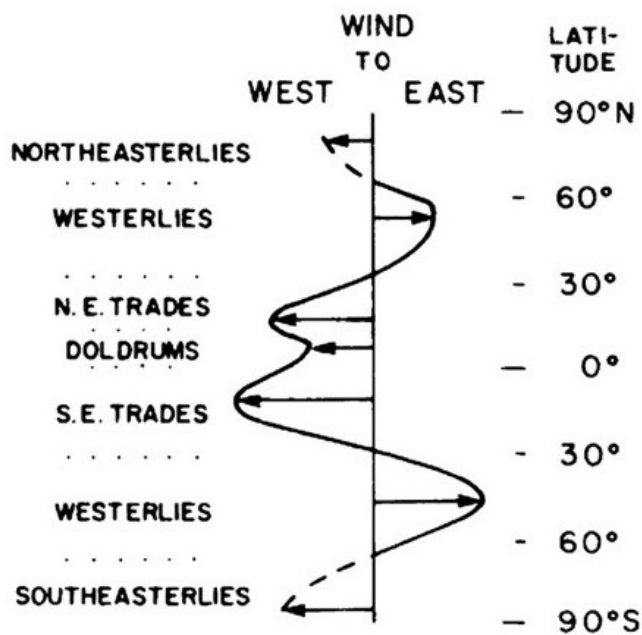


Fig. 3.7: Curve of the zonal wind stress varying with latitude, modified from Pond and Pickard (2013).

To reach a minimum of 0.1 N m^{-2} and a maximum of 0.2 N m^{-2} , a wind stress magnitude, τ_0 , of 0.15 N m^{-2} was taken. A shift of 0.05 N m^{-2} or -0.05 N m^{-2} would then result in the curve ranging between a wind stress of 0.1 and 0.2 N m^{-2} . This asymmetry or shift is shown in Fig. 3.8 as the vertical shift, D .

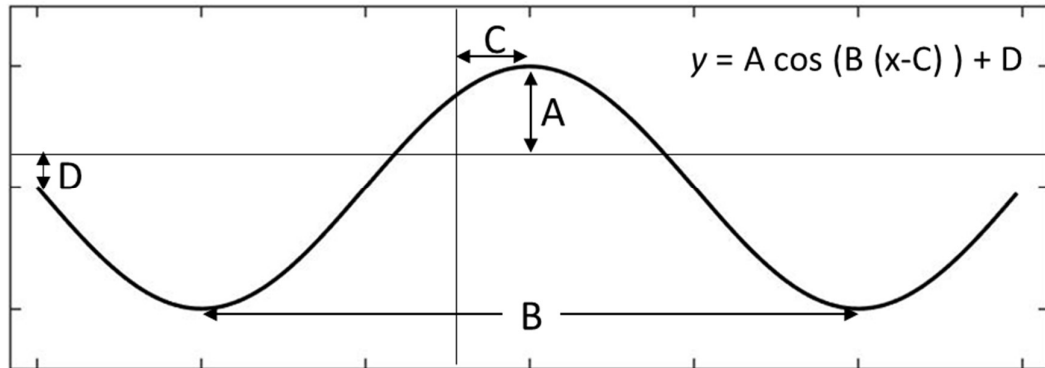


Fig. 3.8: Depiction of the standard cosine function. A is the amplitude, B is the wavelength, C the horizontal shift, and D the vertical shift.

The idealized wind stress function now becomes:

$$\tau_{0x} = -0.15 \cos(3y) + 0.05 \quad (3.5)$$

Or as applied in the model:

$$\tau_{0x} = -1 \frac{-0.15 \cos(3y) + 0.05}{\rho_{horef}} \quad (3.6)$$

The wind stress function in equation 3.6 was used for most experiments, including the reference experiment. Fig. 3.9 depicts the region of the model domain within the idealized wind stress function.

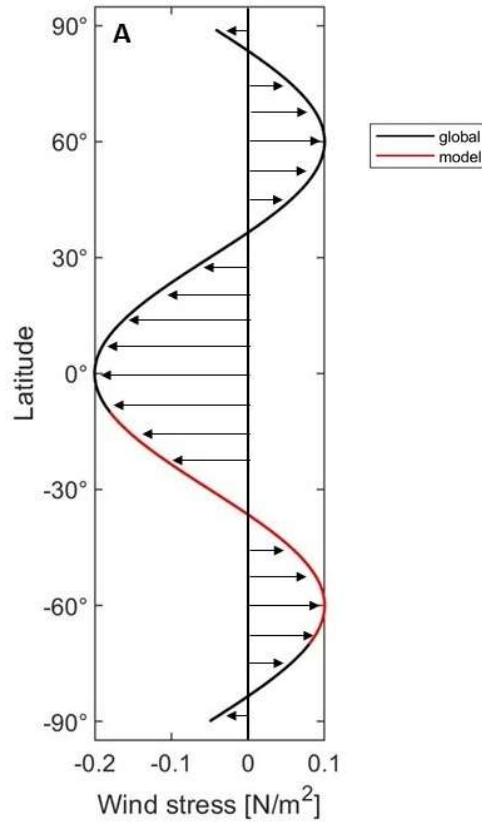


Fig. 3.9: Idealized wind stress function according to equation 3.4. Red represents the latitudinal area of the model domain.

The idealized wind stress function was used in the majority of the experiments including the reference (ref) experiment. This applied wind stress was compared to the data from the previously mentioned NOAA Blended Sea Winds as seen in Fig. 3.10, which showed that there was an error in the idealized wind stress function. Instead of varying between wind stress magnitudes of -0.1 and 0.2 N m^{-2} , the wind stress varies between -0.2 and 0.1 N m^{-2} .

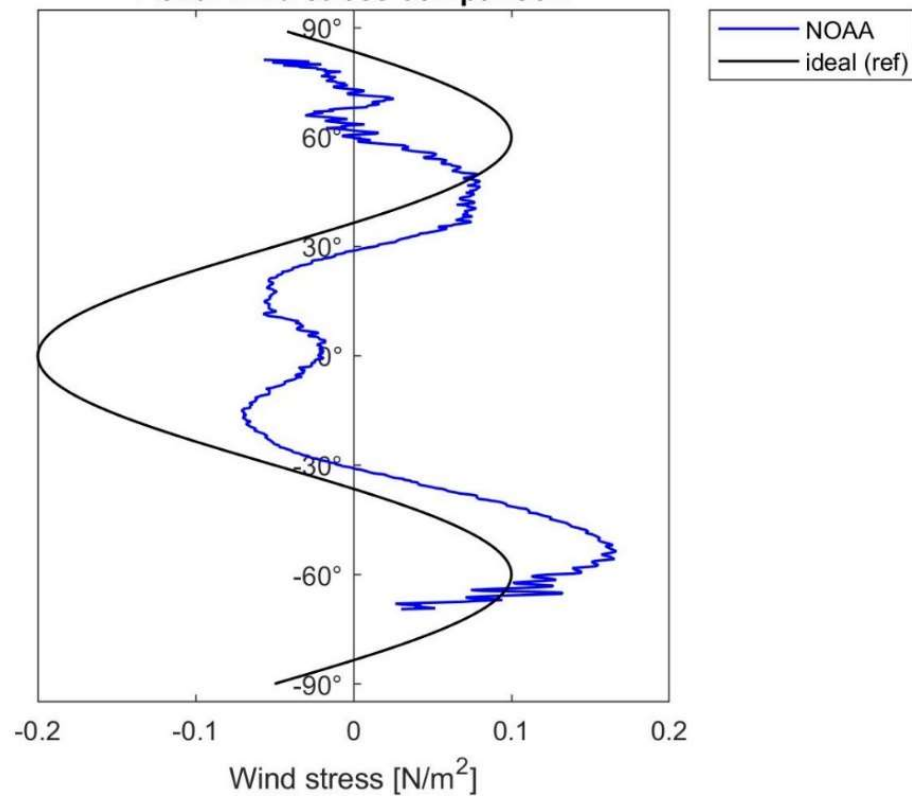


Fig. 3.10: Comparison of the idealized wind stress function used in the reference (ref) experiments within the model (black) and observed NOAA satellite data (blue).

Two additional wind stress functions were therefore applied to the model to test for the effect of the asymmetry with either a vertical shift of -0.5 N m^{-2} (3.7) or no vertical shift (3.8).

$$\tau_{0x} = -1 \frac{-0.15 \cos(3y) - 0.05}{rhore} \quad (3.7)$$

$$\tau_{0x} = -1 \frac{-0.15 \cos(3y)}{rhoref} \quad (3.8)$$

The different asymmetries are once again compared to the observed NOAA satellite data to determine whether there is a good fit with observed data in Fig. 3.11.

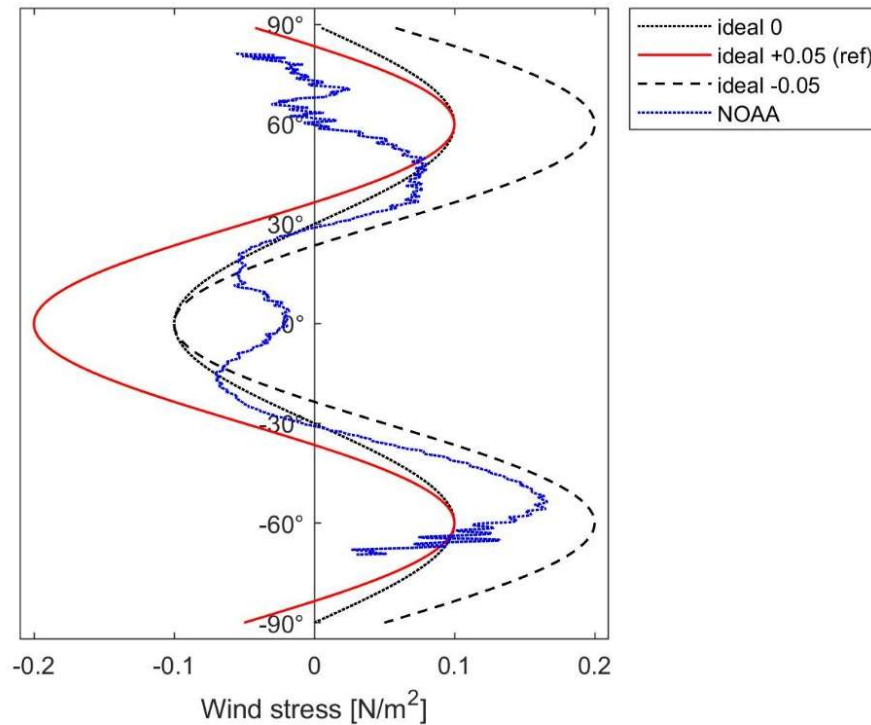


Fig. 3.11: Comparison of the different asymmetries (red and dashed lines) to observed NOAA satellite data (blue).

3.2.5 Coriolis Parameter

The Coriolis Force is incorporated into the model through the Coriolis parameter, f , as a function of the rotation rate and paleolatitude, shown in equation 3-1. Four different Coriolis parameters are incorporated into the model: a modern-day value, Devonian value, uniform value, and no Coriolis effect.

$$f = 2 \cdot \Omega \cdot \sin(\varphi) \quad (3.9)$$

Where Ω is the rotation rate in $\text{rad} \cdot \text{s}^{-1}$, and φ in the latitude in radians.

The standard Coriolis parameter value used in POM incorporates the present-day rotation rate, Ω , of $7.292 \times 10^{-5} \text{ rad} \cdot \text{s}^{-1}$. Different Coriolis parameter values were tested as well since research has suggested that Devonian days were shorter than the present-day, leading to a greater Coriolis force which could affect oceanic surface circulation in the Rheic. According to Zhenyu, Yaoqi, and Guosheng (2007), a Devonian year consisted of 407.1 days rather than 365 days due to a rotational speed of $8.106 \times 10^{-5} \text{ rad} \cdot \text{s}^{-1}$. An additional experiment using a uniform Coriolis parameter irrespective of latitude was carried out to understand the general effect of the Coriolis parameter on the circulation. The latitude value in the middle of the reference model domain was to be used for the uniform Coriolis parameter value. Due to an error, however, a latitude of -35° was used instead of a latitude of -45° .

3.3 Data analysis

Seven output parameters were extracted from the POM NetCDF file and used to display data, these are listed in Table 3-2 below. The kinetic energy (E_k), surface elevation (elb) and horizontal velocities (uab and vab) were plotted against the runtime of 150 days in GMT to verify that a steady state was reached. The land-sea mask (dum) was overlain with the rotated coastlines

described in section 3.2.1 and used as a base map for displaying the (steady state) horizontal velocities (u_{ab} and v_{ab}), wind stresses (w_{surf} and wv_{surf}), and surface elevation (elb) with GMT. The surface elevation was shown as a simple colour gradient map, while the wind stress was shown as a colour gradient overlain with vector arrows. The horizontal velocities were plotted with the `ptrace` (process trace) function in GMT which plots small increments of the horizontal (u_{ab} and v_{ab}) velocities on the map. The small increments are displayed in such a way that they appear as vector tails whose length and colour intensity varies with the magnitude of the horizontal velocities.

Table 3-2: The POM output parameters used for plotting data in GMT

Parameters	Description	Units
dum	Mask with values of 0 = over land and 1 = over sea	binary
Ek	Kinetic energy per unit mass	$m^2 \cdot s^{-2}$
elb	Surface elevation	m
uab	Depth-averaged, horizontal velocity in the east-west direction	$m \cdot s^{-1}$
vab	Depth-averaged, horizontal velocity in the north-south direction	$m \cdot s^{-1}$
wusurf	Zonal wind stress	$Nm \cdot kg^{-1}$
wvsurf	Meridional wind stress	$Nm \cdot kg^{-1}$

4 RESULTS AND ANALYSIS

4.1 Reference experiment

The reference experiment is forced by an idealized zonal wind stress and present-day Coriolis parameter. The basin geometry consists of a basin with a uniform depth of 200 m laterally closed on all sides either due to land, or due to virtual model boundaries. The land-sea distribution used in the experiment represents an Emsian (400 Ma) geometry derived from the paleogeographic reconstructions by Torsvik and Cocks, 2017 (see section 3.2.1). This has resulted in the land-sea distribution shown in Fig. 4.1 in which the Rheic oceanic basin (white) is enclosed to the north and south by the Laurussian and Gondwanan continental masses (grey), respectively. The figure displays a longitudinal Rheic basin oriented in the SW-NE direction located between 70° and 10° south latitude and 130° and 70° east longitude. The basin has a length (W-E extent) of 7,800 km and width (N-S extent) between 2,300 and 3,300 km. This makes it twice the length and three times the width of the Mediterranean in comparison (Encyclopaedia Britannica, n.d.).

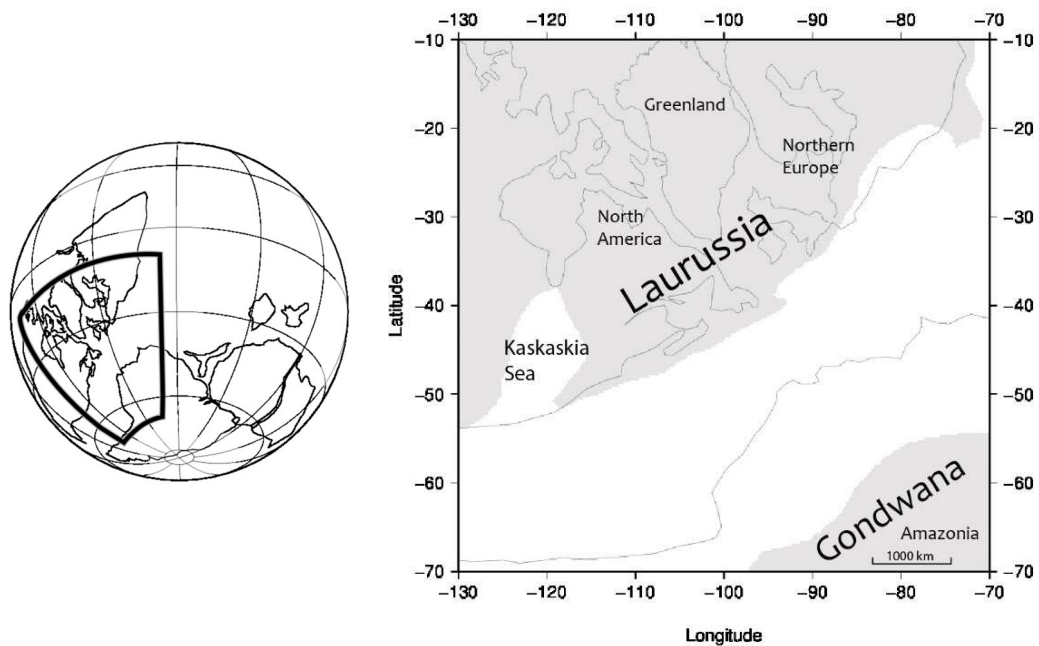


Fig. 4.1: Orthographic projection of rotated continental units, showing the outlined model domain (left). Linear projection of model domain with the land-sea distribution of the Emsian reference experiment shown right.

In this study, the continental shelf edge will be considered to be roughly where continental outlines are in contact with the Rheic ocean basin. In the central part of the Laurussian coast, however, the grey area representing land extends past the continental outlines. The edge of the grey area is then taken to be the shelf edge or shelf break. Taking this into account, the land-sea distribution in Fig. 4.1 shows that the Laurussian margin consists of a narrow shelf (little distance between edge of grey area and continental outlines) when compared to the Gondwanan shelf (large distance between edge of the grey area and continental outline). When looking at the northern Rheic Ocean margin into more detail: from the north-eastern tip of Laurussia and moving to the southwest of the margin in Fig. 4.1, the Laurussian shelf is shown to widen slightly. Here, the Rheic Ocean reaches over the shelf break into what is present-day Belarus, Poland, Germany,

and Belgium. The Rheic then retreats and continues closely along the Laurussian shelf break until it reaches the epeiric sea in the North American segment of Laurussia corresponding to the Kaskaskia Sea (Martin, 2013, p.380; Monroe and Wicander, 2014, p.515). On the southern side of the Rheic, the border with the Amazonian segment of Gondwana reaches far more land inward and the shelf reaches a width of up to 1800 km.

The time series of the two basin-averaged horizontal current velocities is shown in Fig. 4.2, as well as surface elevation and kinetic energy. The time series confirm that the basin has stabilized within the duration of the run. The north-south (blue) and east-west (red) directed horizontal velocities in Fig. 4.2a are hard to discern from each other, but of main importance is that they both reach a steady state value of 0.0005 m/s after 75 days. The mean surface elevation (Fig. 4.2b) of the basin reaches a steady state value of -0.035 metres after 85 days and the basin-averaged kinetic energy takes 100 days to reach an equilibrium point at 0.001 N/m².

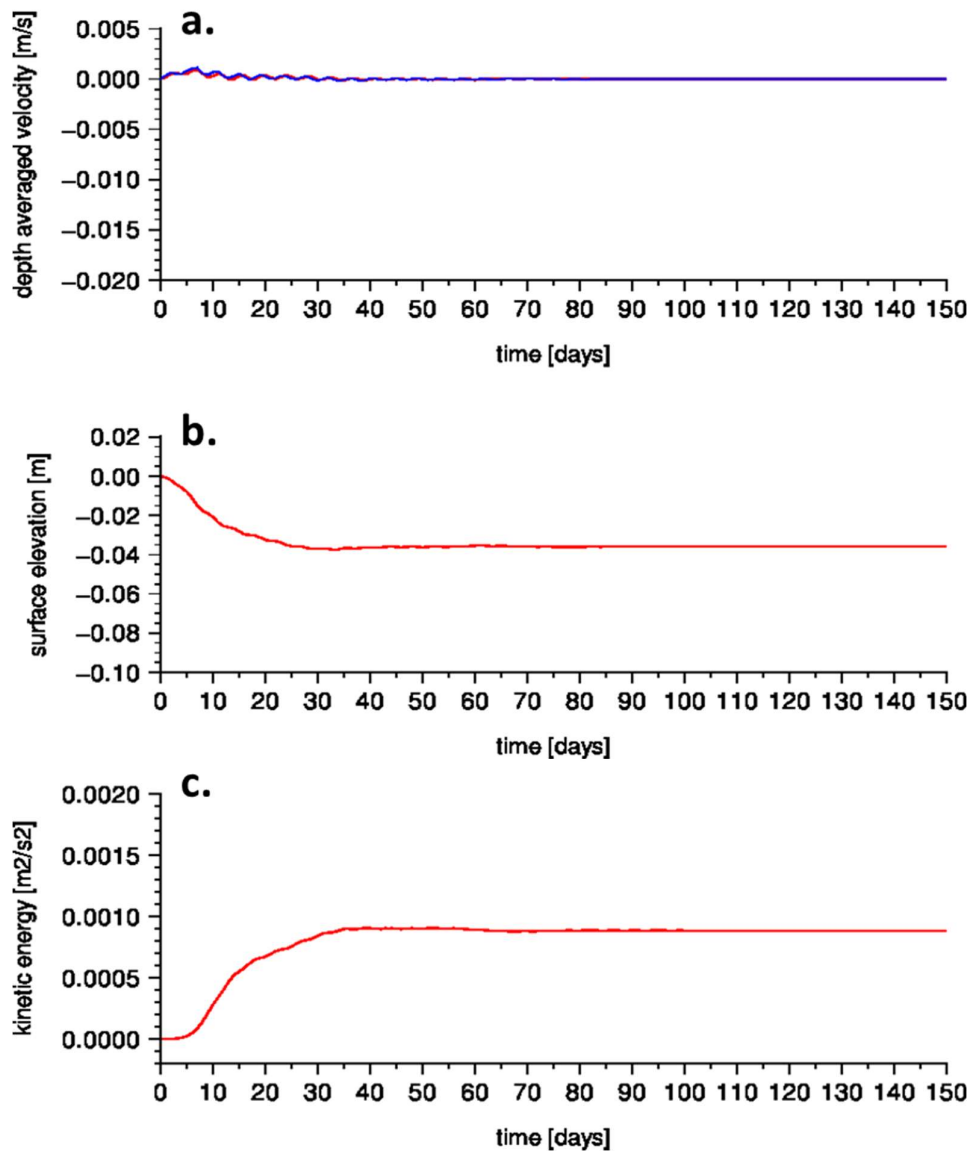


Fig. 4.2: Reference experiment basin-averaged velocity, mean elevation of the free surface (surface elevation) and basin-averaged kinetic energy over the model runtime of 150 days.

Fig. 4.3 displays the wind stress intensity as blue-red colours and direction of the applied wind stress as vectors. The figure shows that the idealized wind stress function (section 3.2.4) has been translated correctly to the model wind stress pattern. A westward wind stress in the northern domain of the ocean can be observed, which corresponds to a negative wind stress value (blue). A basin maximum of 0.976×10^{-4} Nm/kg is reached at the north-eastern edge of the ocean, and gradually decreases to zero until the inflection point at roughly -35° (white). The wind stress then gradually increases again, in the eastward direction (red). A maximum wind stress occurs at approximately -60° , after which the wind stress decreases again.

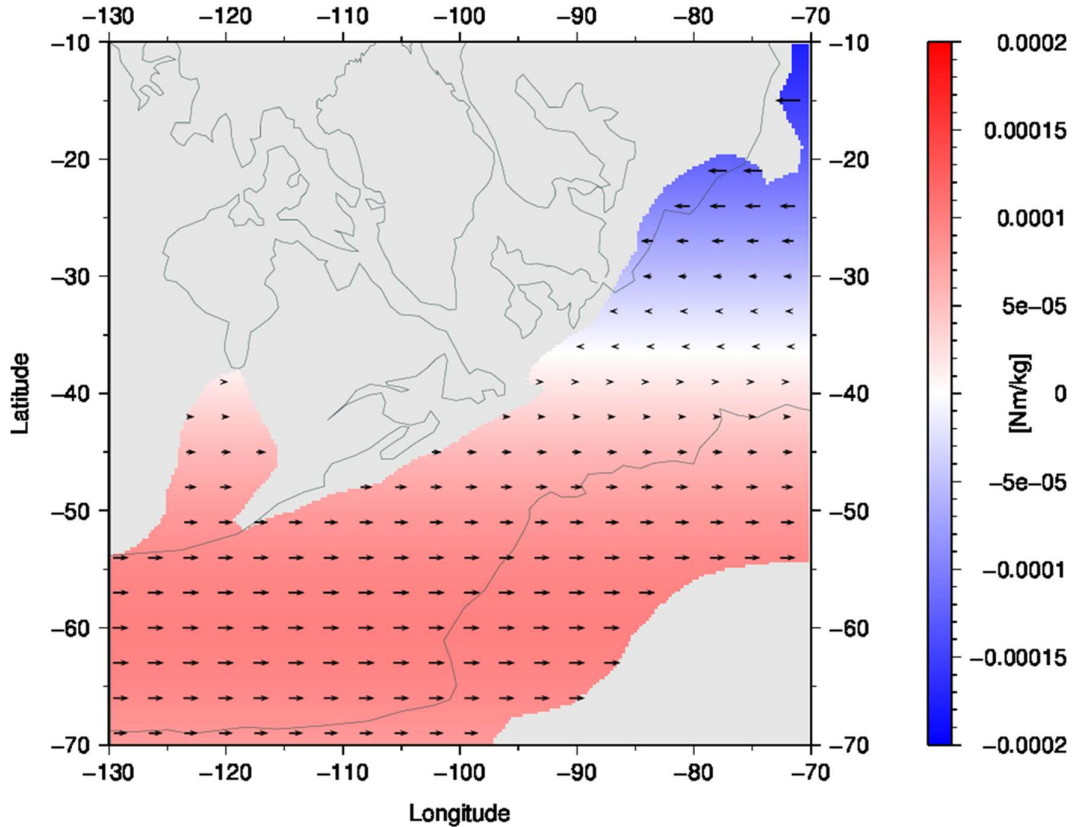


Fig. 4.3: Model domain of the Emsian reference experiment, showing the direction and intensity of applied wind stress on the basin.

Fig. 4.4a shows the depth-averaged, horizontal current velocities within the basin which have been combined into trace vectors to display the direction as well as the intensity of the water mass. There is a difference in flow direction between the north-eastern and south-western half of the ocean. In the north-eastern half of the basin, above 50 - 55° south latitude, the water flows counter-clockwise while in the south-western half of the ocean it moves clockwise. This pattern is reflected in the free surface elevation map as well (Fig. 4.4b) where a positive surface elevation is generated in the northern-eastern region of the Rheic Ocean (red), reaching a maximum surface elevation of 0.29 meters, while a negative elevation or depression (blue) forms in the south-western half of the ocean. The maximum depression in the south-western area is 0.55 meters. These counter-clockwise and clockwise directed water masses represent two distinct gyres, either cyclonic (clockwise) or anti-cyclonic (anti-clockwise). The northern, anti-cyclonic gyre generates a positive elevation and the southern, cyclonic gyre a negative elevation. This flow pattern and elevation point to essentially geostrophic flow.

Overall, the highest velocities of the basin occur in the northern gyre along the border with Laurussia between approximately 20-55° south latitude. This is shown as an increase in the length of vector tails in Fig. 4.4a, which is assumed to be the WBC. This western boundary phenomenon can also be observed in the Kaskaskia Sea within the Laurussian continent, where the western boundary is subjected to slightly higher velocities than its eastern boundary. High current velocities are also reached near the southern edge of Gondwana where the water flows away from the Gondwanan margin along the southern model boundary towards the west. In both cases this increase in velocity could also be due to effects of the model boundaries on the modelled circulation, further referred to as boundary effects.

The convergence of the southern and northern gyres is reflected by a change in the flow direction along both the Laurussian and Gondwanan margins between 50-55° south latitude. Two flows from opposite directions combine at the Laurussian margin at this point: a strong south-west directed flow along the northern half of the margin and a slower north-east directed flow coming from the southern gyre converge and continue to flow eastward. This eastward directed flow then gradually decreases in speed as it reaches the Gondwanan margin on the other side and diverges into a slow north-eastern and an increasingly faster south-west directed flow. The north-east directed current then flows up north past the eastern model boundary to eventually reach the strong current at the Laurussian margin. The south-western Gondwanan flow picks up speed as it flows along the southern model boundary and reaches Laurussia where it loses speed and combines with the faster south-east directed current at the inflection point. The convergence of gyres at lower latitudes (subtropical) and relatively higher latitudes (subpolar) gyres is also observed in modern-day oceans, for example when the northward Gulf Stream and southward Labrador Current combine at the North American margin and become the eastward North Atlantic drift, which then separates into a northward Norway Current and southward Canary Current at the European margin.

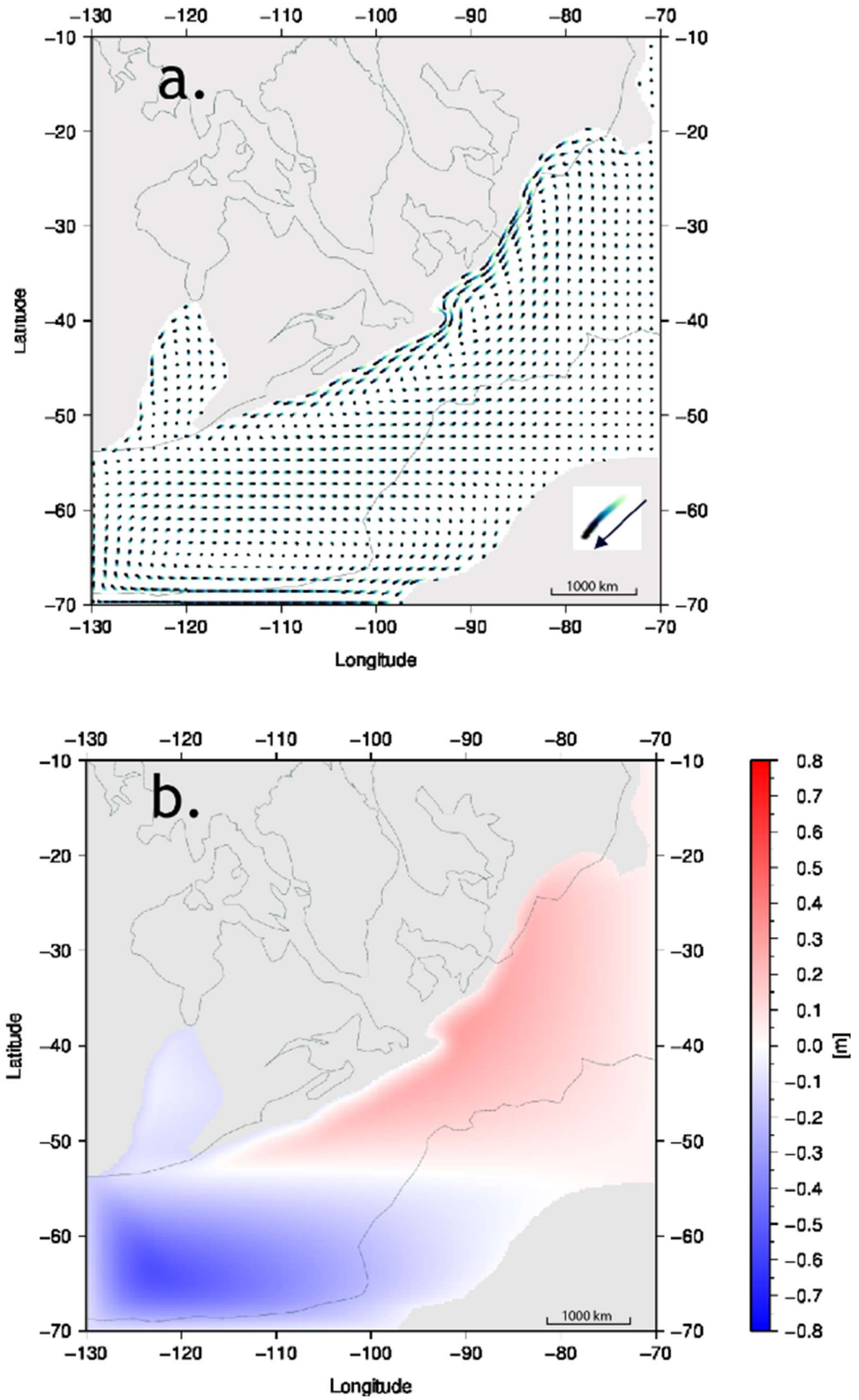


Fig. 4.4: Reference model domain showing the a) generated depth-averaged horizontal velocities and b) free surface elevation of the basin.

4.2 Effect of paleogeography

In this section, the effect of three aspects of paleogeography on the Rheic surface current pattern is studied, namely the land-sea distribution, bathymetry, and throughflow of the Rheic basin.

4.2.1 Influence of the land-sea distribution

The modelled land-sea distribution of the Rheic basin varies through time and is based on several chosen published paleogeographies (section 3.2.1). The following experiments are carried out to achieve a better understanding of the role of the land-sea distributions in generating a current pattern in the Rheic Ocean.

Comparison of Famennian (370 Ma) paleogeographic reconstructions

In the basin geometry based on Torsvik and Cocks (2016) (Fig. 4.5a), a back-arc setting is reconstructed which includes two small islands, the Saxothuringian Terrane and Moesia Terrane, bordering the north-eastern edge of the Laurussian margin (Cocks and Torsvik, 2006). In contrast to the Emsian reference experiment, the Rheic basin in this experiment is located between the equator and -60° . The applied wind stress pattern, therefore, corresponds to the idealized wind stress at these lower latitudes. As such, an anti-cyclonic gyre covers most of the basin in Fig. 4.5b. The beginnings of a cyclonic gyre can be seen around -60° , as evidenced by a westward directed flow at the southern margin of the Rheic basin. Highest velocities are again reached on the north-western Rheic border with Laurussia, where the flow is directed towards the south-west. In contrast to the reference experiment, the strong WBC extends all along the Laurussian margin in this experiment. As it reaches the western model boundary, it is deflected southward and eastward towards the Gondwanan margin. As it then moves along the Gondwanan margin, it is ultimately deflected northward along the eastern model boundary.

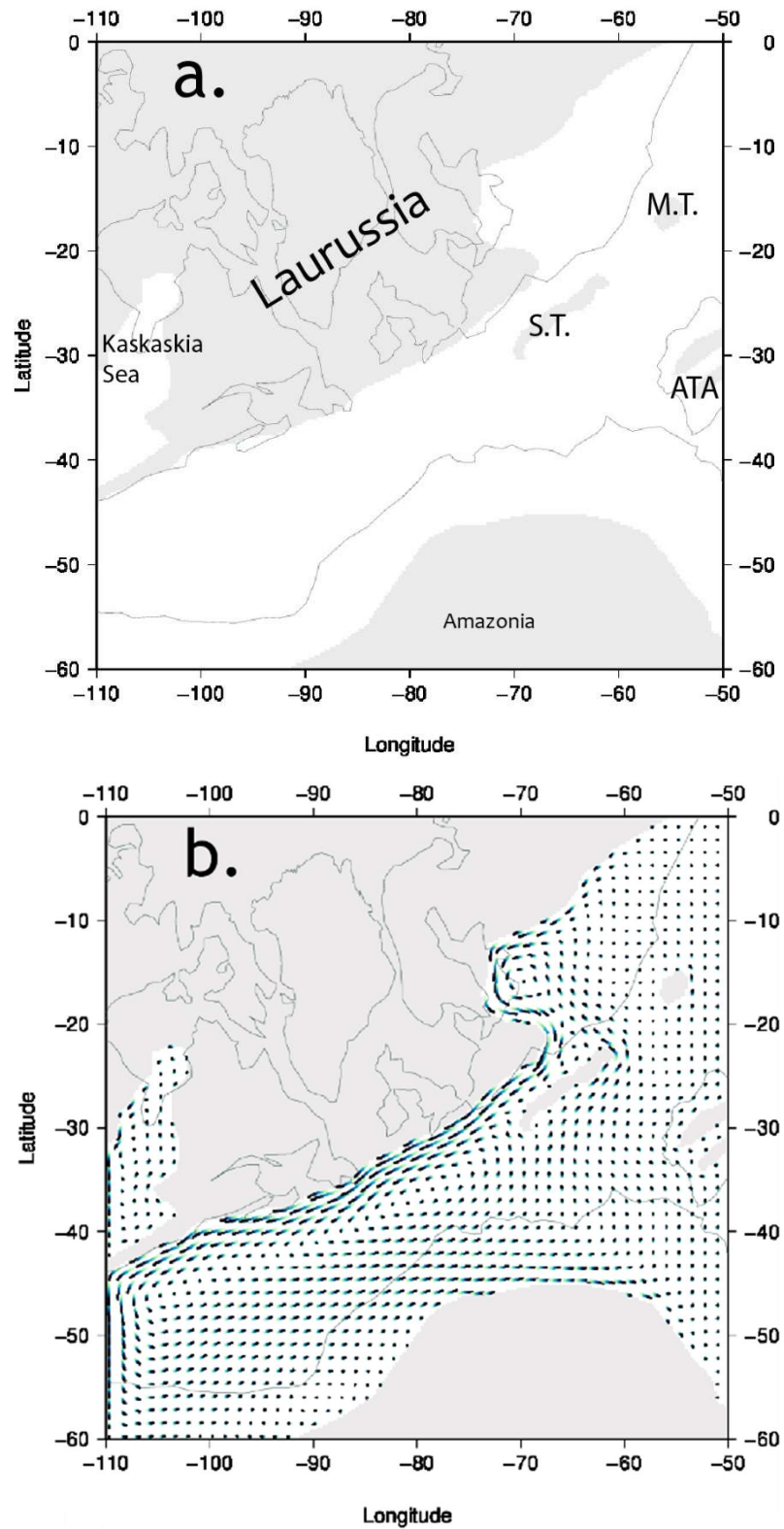


Fig. 4.5: Famennian paleogeographic experiment series with a) land-sea distribution of the Torsvik reconstruction including the Saxothuringian Terrane (S.T.), Moesia Terrane (M.T.) and Armorican Terrane Assemblage (ATA), and b) the resulting depth-averaged horizontal velocity pattern.

As the northward directed flow leaves Gondwana and reaches the islands, it is diverted either left or right around the island, reaching higher speeds at the corners of the islands. Higher velocities are especially observed at the north-eastern margin of the Saxothuringian Terrane. As the current is deflected around the terrane it joins the WBC, generating a small “boundary vortex” near the convoluted Laurussian margin in an area that would cover present-day Latvia, Lithuania, Belarus, and Poland (Munk and Carrier, 1950).

The land-sea distribution in Fig. 4.6a is based on the continental configuration by Dopieralska (2009). The main differences are the presence of only one island near the Laurussian margin which represents the Armorican Terrane Assemblage (ATA) and the configuration does not include the Kaskaskia sea in eastern Laurussia. Additionally, the Laurussian margin is more convoluted than in the previous land-sea distribution.

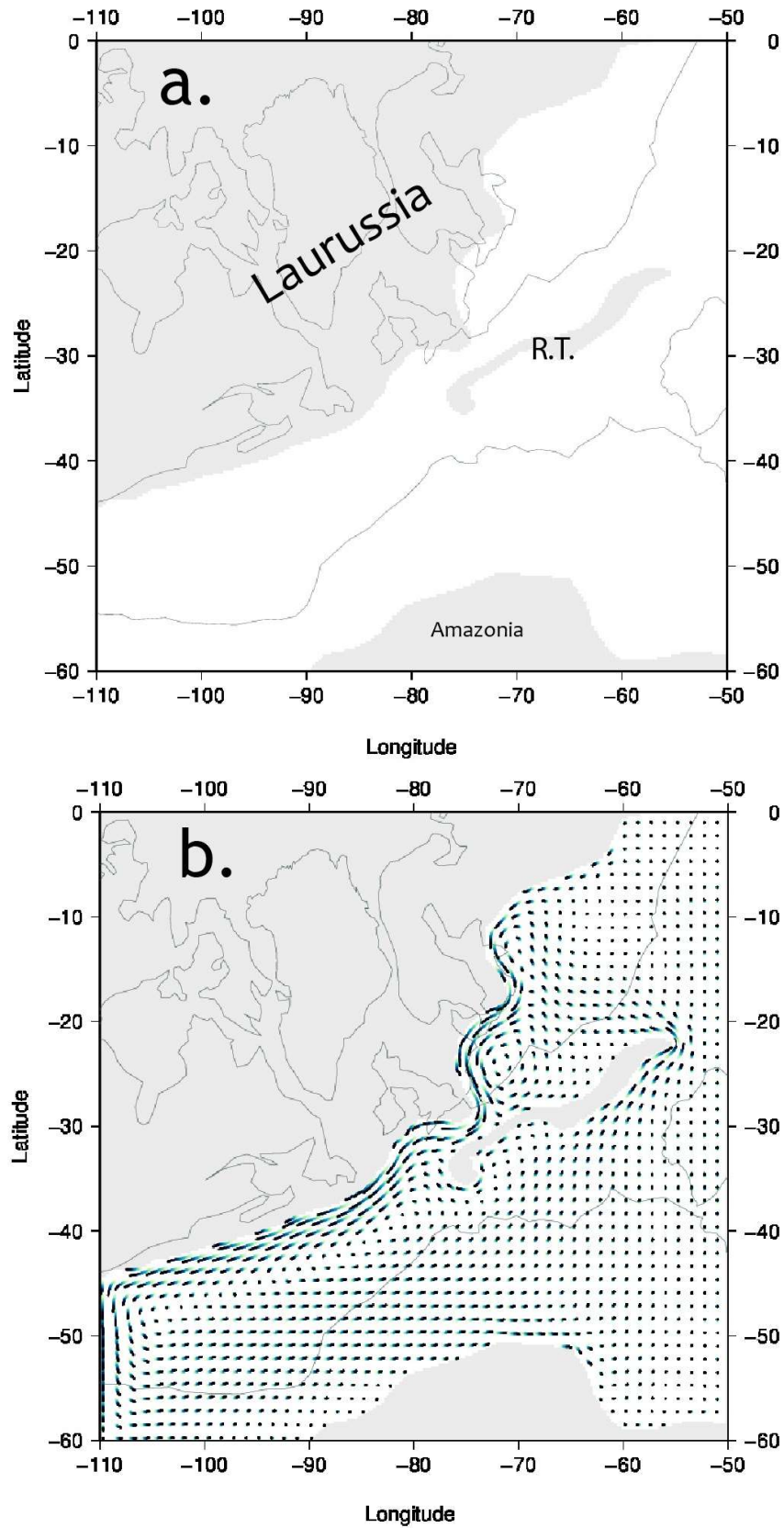


Fig. 4.6: Famennian paleogeographic experiment series: a) land-sea distribution based on the reconstruction from Dopieralska (2009) including the Rhenohercynian Terrane (R.T.) and b) depth-averaged horizontal velocity pattern.

The strongest flow is once again found along the western margin of the Rheic Ocean with Laurussia in Fig. 4.6b. A similar boundary vortex is reached at the convolution in north-eastern Europe with an added, stronger boundary vortex in present-day Germany. As the current reaches the south-western edge of the basin with Laurussia it is deflected eastwards around Gondwana in the same manner as in Fig. 4.5a.

In the land-sea distribution shown in Fig. 4.7a, based on Huneke (2006), the eastern Laurussian margin is strongly north-south oriented between 0-30° south latitude. The margin then becomes south-west oriented at latitudes higher than 30° south latitude, eventually incorporating a large Kaskaskia Sea in south-west Laurussia. The margin is overall less convoluted than the previous configurations, and the Kaskaskia Sea reaches farther inland. The land representing the Amazonian section of Gondwana does not resemble that of previous configurations in shape and location. It is located at lower latitudes and is therefore closer to Laurussia, causing a narrow region at the centre of the Rheic basin. Two islands can be observed in the eastern part of the ocean corresponding to the Noric terrane (N.T.) and ATA.

Fig. 4.7b shows how the strong current at the western margin of the Rheic bordering Laurussia is faster and narrower in the N-S oriented part of the Laurussian margin but widens as the margin becomes S-W oriented. The water flowing along the Laurussian margin is deflected to the east and north-east as it reaches the western model boundary. This “returning flow” picks up speed and reaches the point at which the Rheic narrows between 30 and 40 south latitude. Velocities of the eastward flow along Gondwana margin are relatively higher at this constriction, but once the water deflects back up the eastern model boundary to the north, velocities decrease. The north-eastern edges of the two islands are not visible in this model, but we see a slight increase in water velocity as water flows left and around the south-western edge of the islands at the eastern model boundary.

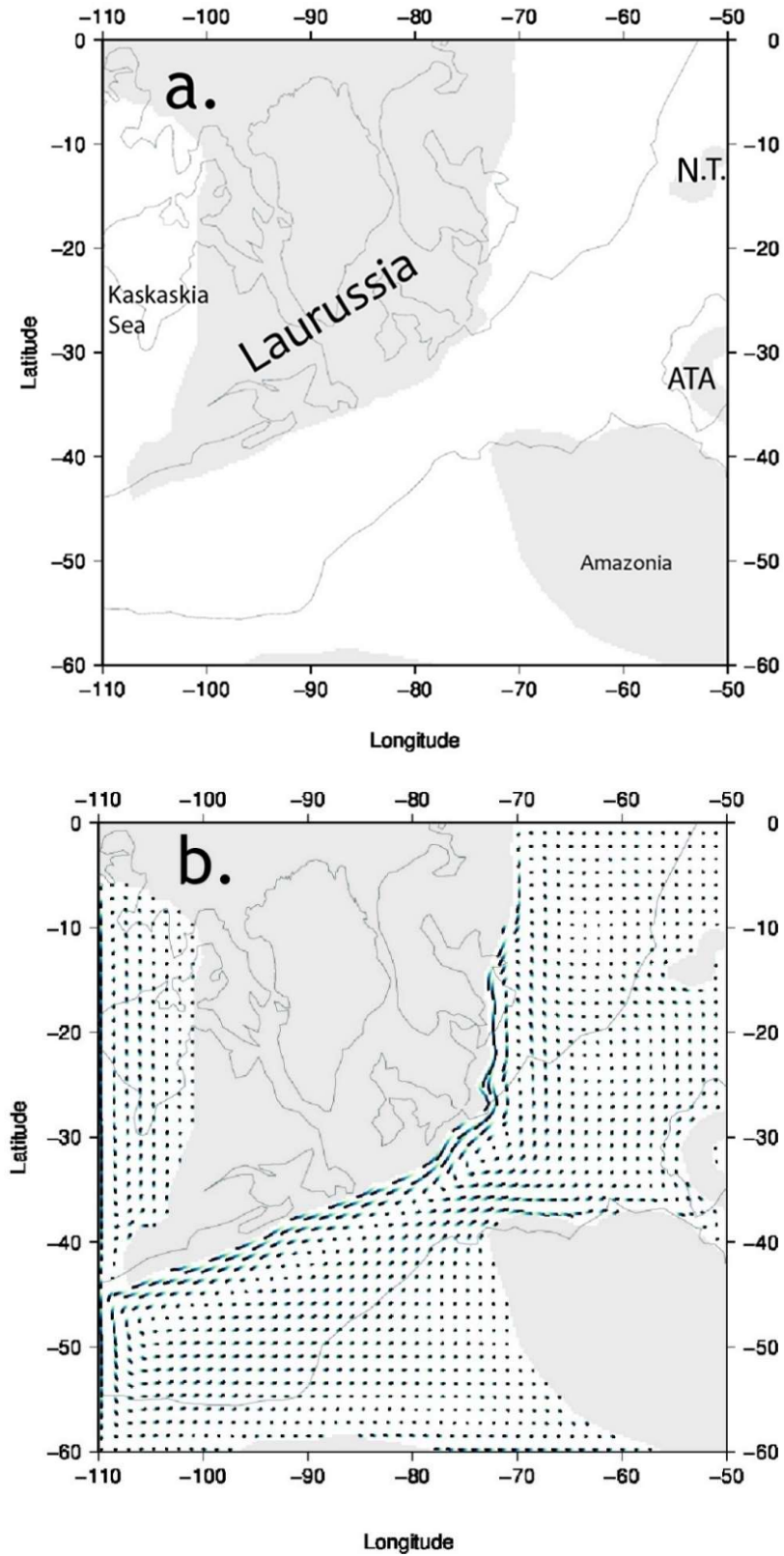


Fig. 4.7: Famennian paleogeographic experiment series: a) land-sea distribution of the Huneke reconstruction including the Noric Terrane (N.T.) and Armorican Terrane Assemblage (ATA), and b) depth-averaged horizontal velocity pattern.

Effect of a closed Tournaisian (350 Ma) gateway

The eventual closure of the Rheic Ocean at the Devonian-Carboniferous boundary is linked to major changes in the global oceanic circulation and related climate change (see Fig. 1.5). To understand the effect of its closure, a land-sea distribution of the Rheic Ocean is tested in which the south-western arm of the Rheic Ocean has been closed. The land-sea distribution is based on the Tournaisian paleogeographic reconstruction by Torsvik et al. (2012).

The land-sea distribution in Fig. 4.8a consists of a smaller Rheic Ocean whose south-western margin is closed to the west by Amazonia. The basin is located between the equator and 45° south latitude and contains a landmass at its centre representing the ATA.

Only one anti-cyclonic gyre is generated in this experiment. Starting at the north-eastern Laurussian margin, the current picks up speed along the margin as in the previous experiments until it reaches the convergence point between Laurussia and Amazonia. The current is then deflected along Amazonia to the south-east, with a minor current flowing back along the south-eastern edge of the ATA as a small vortex. It eventually joins the stronger current along the Laurussian margin. As the other water mass leaving Amazonia towards the north-east bends around the vortex point, it widens as it flows along the Gondwanan margin. Here, the current splits into two arms, a northern and north-eastern arm, losing speed as it reaches the eastern model boundary. Another part of the north-eastern current is deflected around the ATA to once again join the strong south-western current along the Laurussian margin.

The average horizontal velocities and kinetic energy are higher than in the reference experiment (not shown). The depth-averaged velocity vectors on both the Laurussian and Gondwanan margin are longer than in the reference experiment, indicating stronger currents.

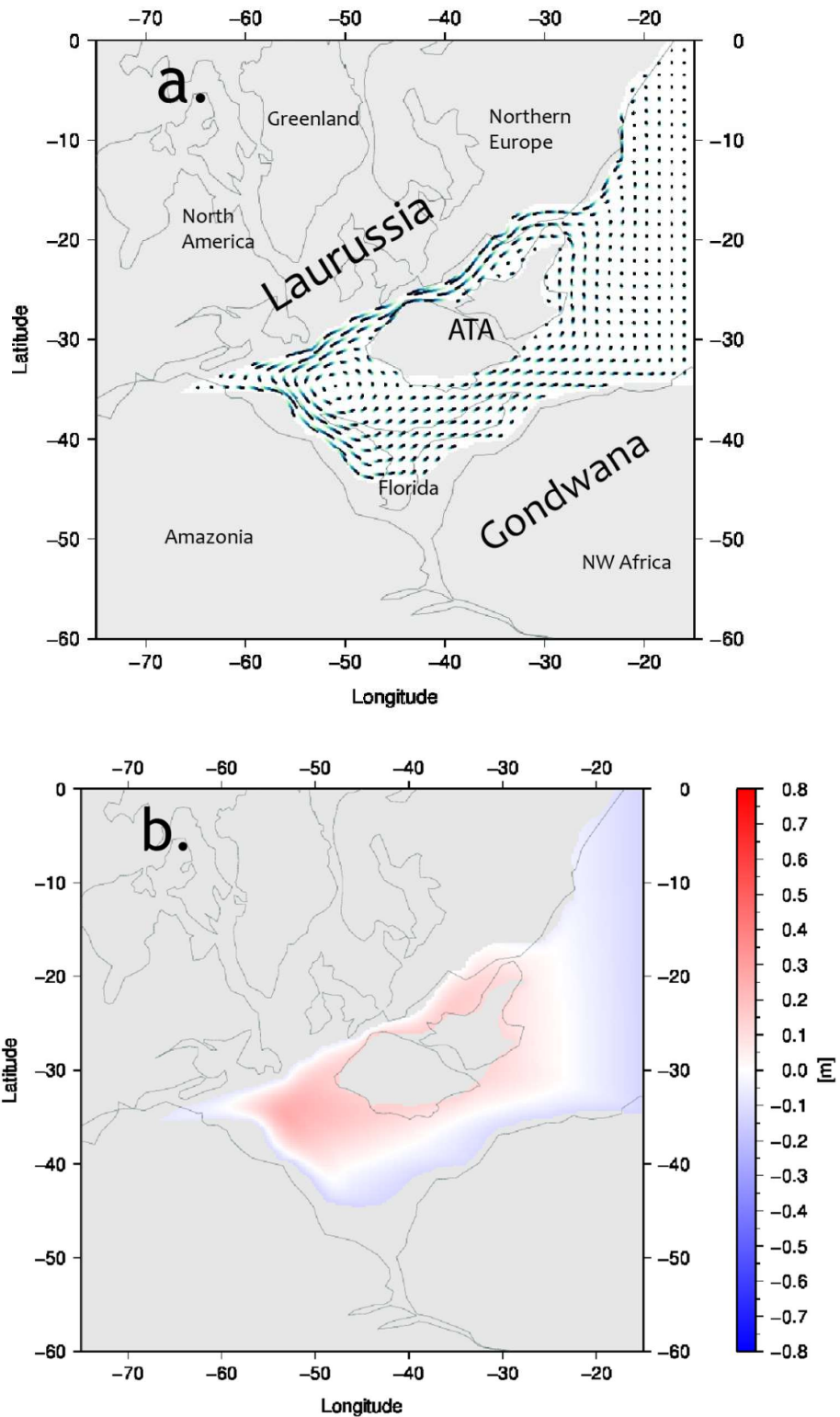


Fig. 4.8: Effect of closure of the Tournaisian seaway: a) depth-averaged horizontal velocity pattern and land-sea distribution including the Armorican Terrane Assemblage (ATA), and b) surface elevation of the basin.

Effect of a shelf break surface current barrier

The choice of model coastline in the previous experiments included shelves. These land-sea distributions, therefore, show the Rheic as reaching farther inland past the reconstructed continental coastlines. The following experiment is an intermediate step towards depth variation, in which the chosen model coastline no longer includes the reconstructed shelves. The model coastline is instead roughly set at the continental coastline to represent a basin whose currents are limited by the shelf break, as it has previously been stated (Segar, 2018, p.183) that the shelf break is able to act as a barrier to the deep WBC.

This limiting shelf break experiment is based on the same Emsian paleogeographic reconstruction by Torsvik et al. (2012) as used in the reference experiment. The resulting ocean basin in Fig. 4.9b is narrower than that of the reference experiment, especially between 40-55° south latitude. As in the reference experiment, two gyres are generated that converge between 50-55° south latitude. A strong current is once again observed at the (north-) western boundary with Laurussia in the northern anti-cyclonic gyre, although the extent is not as great as in the reference experiment. As in the reference experiment, high velocities are also reached in the southern cyclonic gyre where the water mass reaches the southern boundary with Gondwana/Amazonia and is deflected westward. Other than at this southern boundary edge, the southern cyclonic gyre is slower than in the reference experiment. Another difference is the constricted flow at the centre of the Rheic basin due to the narrow basin geometry at 50° south latitude, causing higher velocities to be reached at the northern Amazonian margin than in the reference experiment.

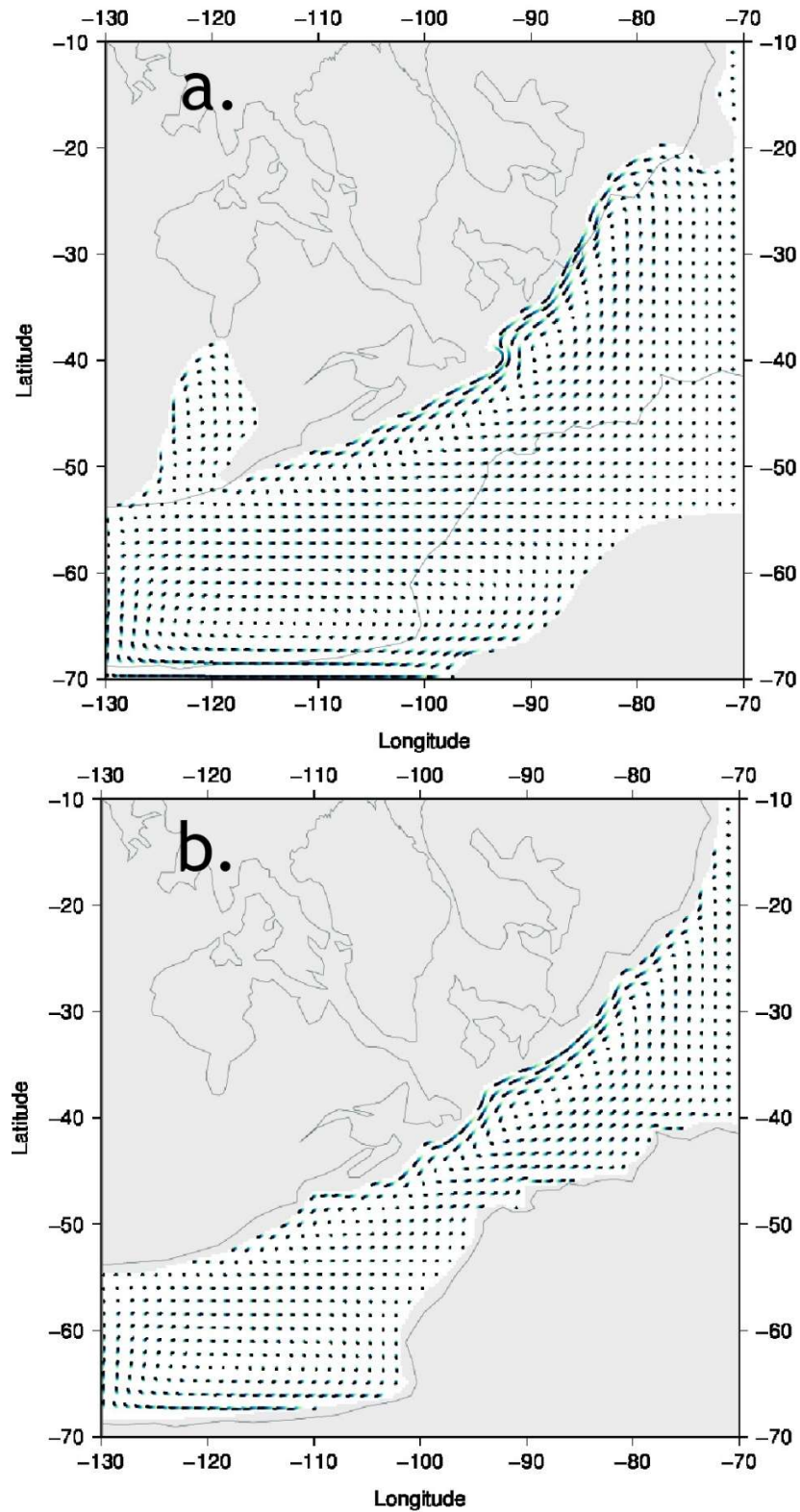


Fig. 4.9: Effect of shelf break as a surface current barrier. Figure a) shows the depth-averaged horizontal pattern of the reference experiment which includes a shelf and figure b) shows the surface current pattern when no shelf is included.

4.2.2 Influence of bathymetry

To determine the effect of bathymetry on the surface current pattern, a grid with a varying ocean depth was generated for both the Emsian and Tournaisian configurations that were based on Torsvik and Cocks (2016).

As described in section 3.2.2, the depths of the oceans were set to vary between 0 and 6000 metres with the greatest depth representing a subduction zone, as seen in Fig. 4.10a. In the bathymetric model, Laurussia has a relatively steep continental slope while the Amazonian continental slope is more gradual.

The surface current pattern that can be seen in Fig. 4.10b no longer shows a strong current at the Rheic western boundary with Laurussia and the circulation pattern is generally much more diffuse. Instead, higher velocities are limited to the north-eastern margin of the ocean with Laurussia, in the Kaskaskia sea, and at the Amazonian shelf. These regions correspond to the shallower areas highlighted by the bathymetric model shown in Fig. 4.10a. The flow direction in the Kaskaskia sea is in the clockwise direction, which is opposite to the flow direction observed in the reference experiment. Except for the westward flow leaving Gondwana at the southern boundary, velocities in areas deeper than approximately 200-300 metres are very low, and the basin is therefore generally quiescent.

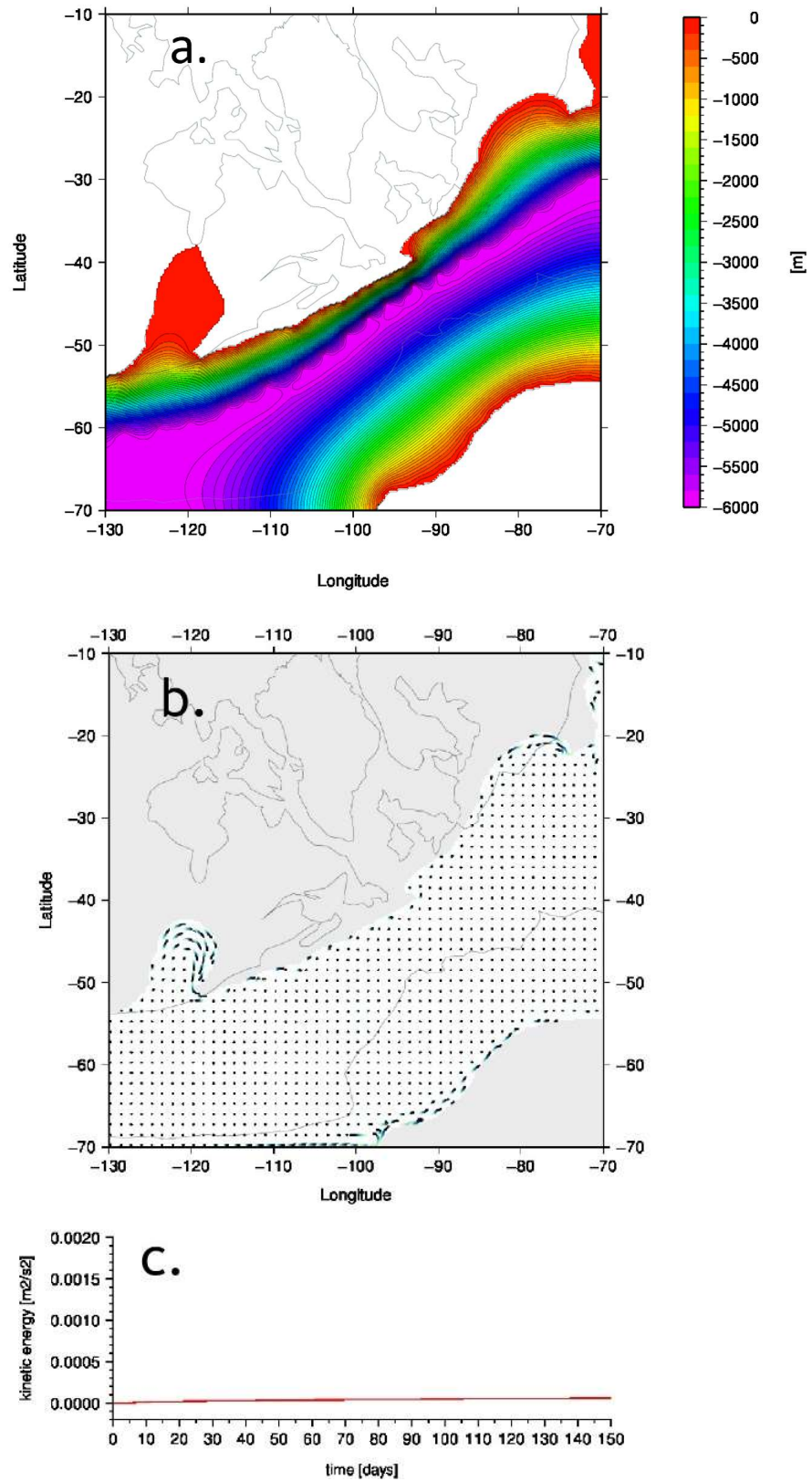


Fig. 4.10: Emsian generated bathymetry experiment results. Figure a) shows the generated bathymetry mask for the Emsian configuration, b) the depth-averaged horizontal velocity pattern for Emsian configuration with generated bathymetry, and c) Emsian experiment time series of the average kinetic energy of the basin over a runtime of 150 days.

The bathymetry for the Famennian configuration in Fig. 4.11 was carried out to test the effect of the bathymetry in a back-arc setting. The back-arc basin to the north of the Rhenohercynian Zone has been set to a depth of 3500 meters. Compared to the Emsian generated bathymetry there is a wider Laurussian shelf in the eastern margin of Laurussia in this configuration, but an absence of the Kaskaskia Sea. The configuration still retains the gradual southern shelf at the Amazonian margin, with a wide shallow shelf between Amazonia and the ATA.

The surface currents in the Famennian experiment in Fig. 4.11a are once again generated in the shallower regions. The highest velocities are generated along the Laurussian margin in the north-eastern part of the Rheic and the current speed decreases again past the S-shaped convolution of this margin. The general direction of the current past this convolution is not clear but seems to be towards the north-east. Velocities along the shallower Gondwanan margin are also higher than the experiments with a uniform depth and water flows around Gondwana towards the east. There is once again a small current at the model boundary in the south which is directed eastward. Velocities around the islands remain relatively low due to the high depths at the island margins, with slight increases in velocity mimicking the decreases in depth.

Although the surface area of the ocean only increases slightly, the much larger depth causes the volume of the basins to be between 12-17 times greater than that of the uniform experiments. The kinetic energy time series in Fig. 4.10c and Fig. 4.11c show that the experiments do not reach a steady state within the standard model run of 150 days, especially in the Famennian scenario in Fig. 4.11c. A steady state is reached for the depth-averaged velocities and average surface elevation.

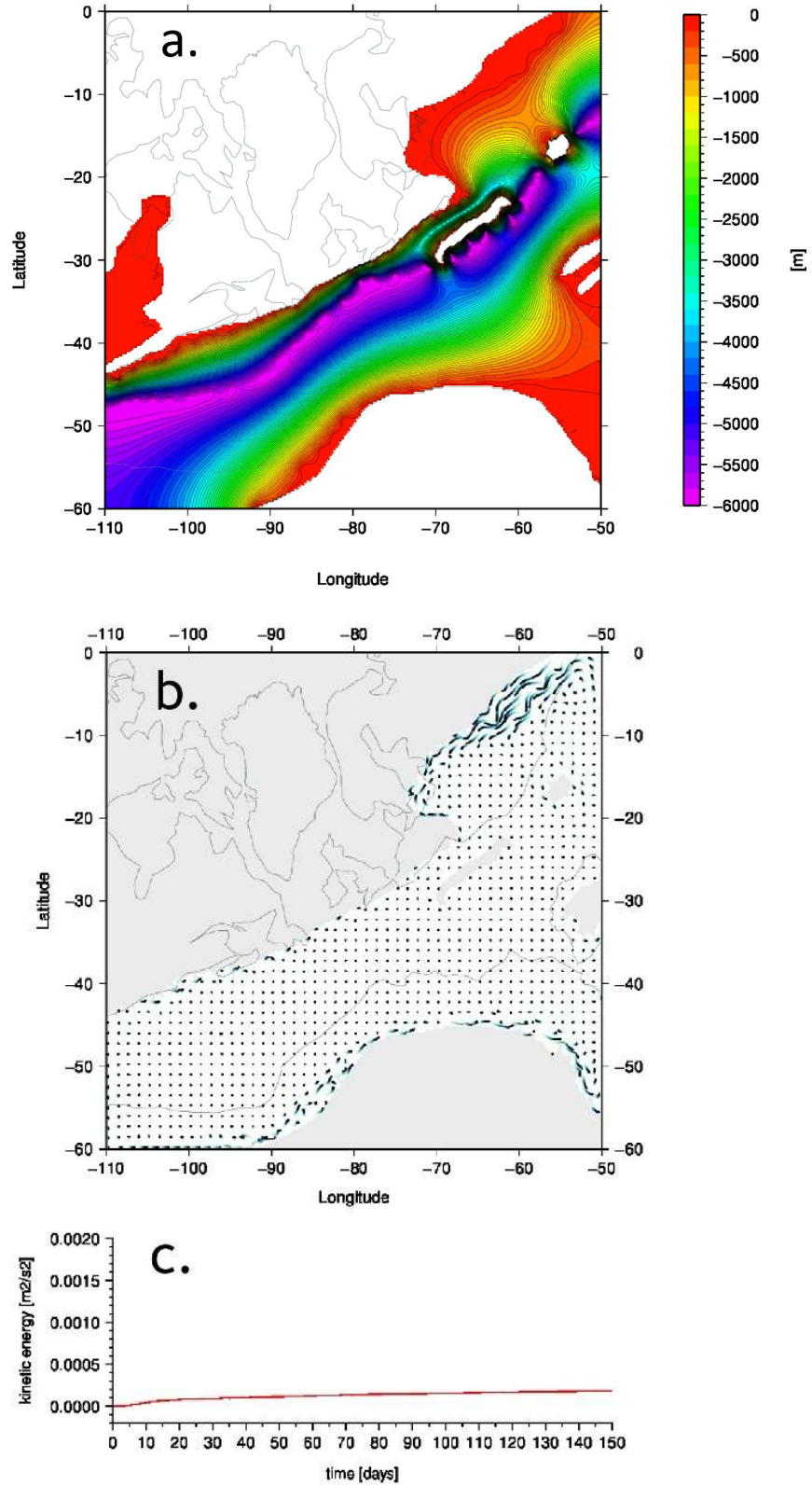


Fig. 4.11: Famennian generated bathymetry experiment results, figure a) shows the generated bathymetry mask for the Emsian configuration, b) the depth-averaged horizontal velocities, and c) Famennian experiment time series of the average kinetic energy of the basin over a runtime of 150 days.

4.2.3 Influence of throughflow

The boundaries of the oceanic basin in the Emsian reference experiment are closed at the eastern and western model boundary. However, in the Devonian the Rheic Ocean would have been the passageway for equatorial waters, allowing currents to move between the poles (see section 2.3). An in- and outflow would, therefore, have occurred at the eastern and western oceanic margins. In the following experiments, the movement of water through the Rheic has been simplified as a throughflow, whereby the eastern and western boundaries have been set to allow a westward directed flow of water of 1, 5 or 7 Sverdrup. Other than having open boundaries, the experiments are identical to the Emsian reference experiment.

For the 1 Sverdrup throughflow experiment (Fig. 4.12a), the velocity pattern of the reference experiment with closed boundaries is nearly identical to that of the reference experiment. The main areas with relatively higher velocities remain concentrated at the Laurussian margin and the southern edge of the model basin, and the two gyres are once again generated. Low velocities are found at the south-eastern margin with Amazonia as well as the eastern model boundary in this experiment as well. This same pattern is repeated for a throughflow of 5 Sverdrup (Fig. 4.13b), the only difference being that the velocity of the water is greater throughout the basin. This same effect is observed with a throughflow of 7 Sverdrup (Fig. 4.14c). We, therefore, see no change in the surface current direction and relative velocity of the water, but the absolute velocity of the basins is increased with an increasing throughflow.

When looking at the steady state elevation time series in Fig. 4.12c, Fig. 4.13c, and Fig. 4.14c, the surface elevation in all three experiments continues to decrease at a faster rate with an increasing throughflow. This can also be seen in Fig. 4.12b, Fig. 4.13b, and Fig. 4.14b. The northern anti-cyclonic gyre differs from the reference experiment in that water is not able to flow geostrophically at its centre. The decrease in elevation is most likely an artefact of an unidentifiable error, but it does not influence the steady-state kinetic energy and horizontal velocities. The current velocity patterns in Fig. 4.12a, Fig. 4.13a, and Fig. 4.14a also seem to be unaffected by this artefact.

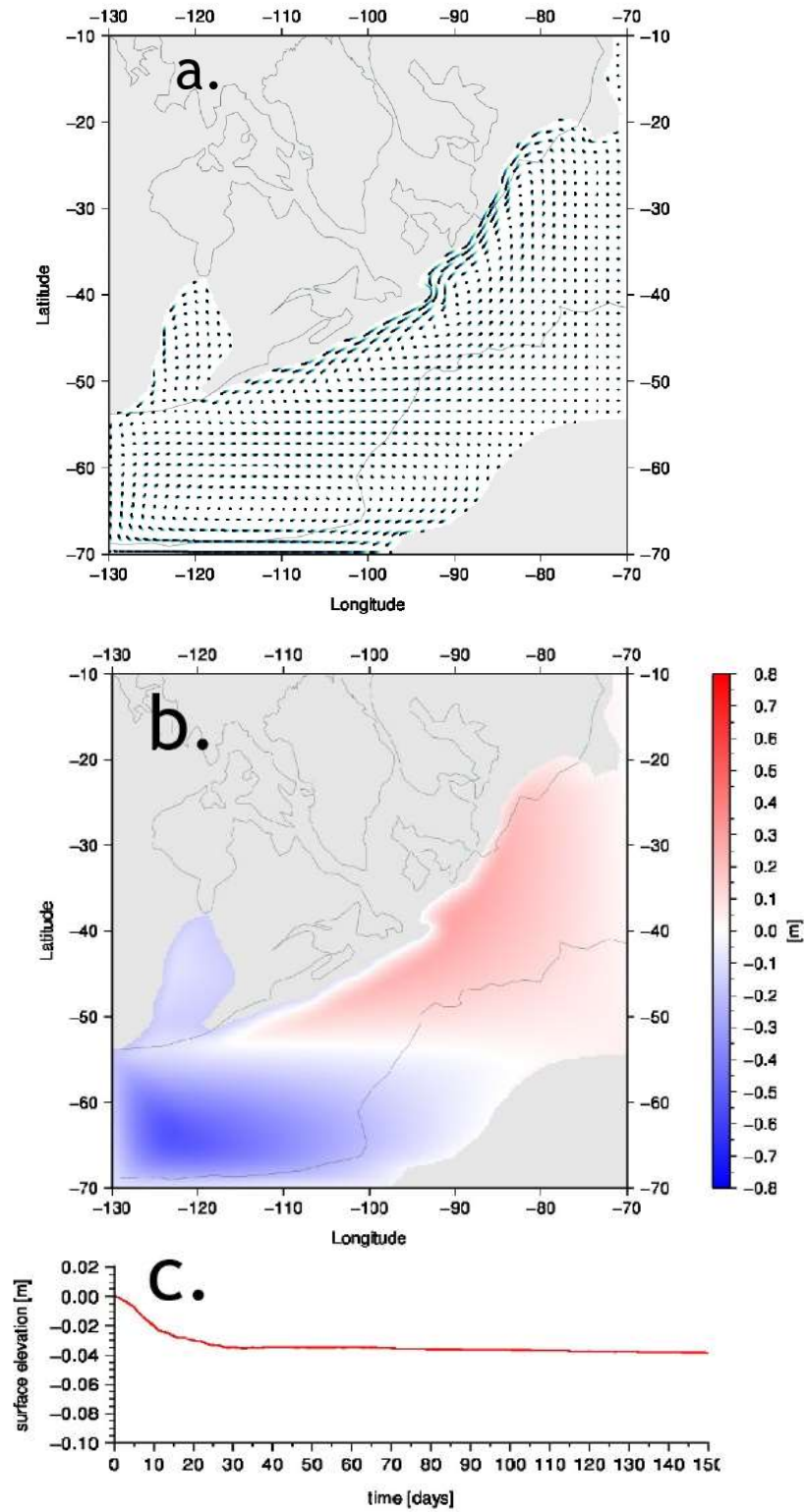


Fig. 4.12: Effect of a net westward flow (throughflow) of 1 Sverdrup: a) depth-averaged velocity pattern of an Emsian basin geometry with an idealized zonal wind stress and uniform depth of 200 meters, b) mean surface elevation and c) surface elevation time series for a run of 150 days.

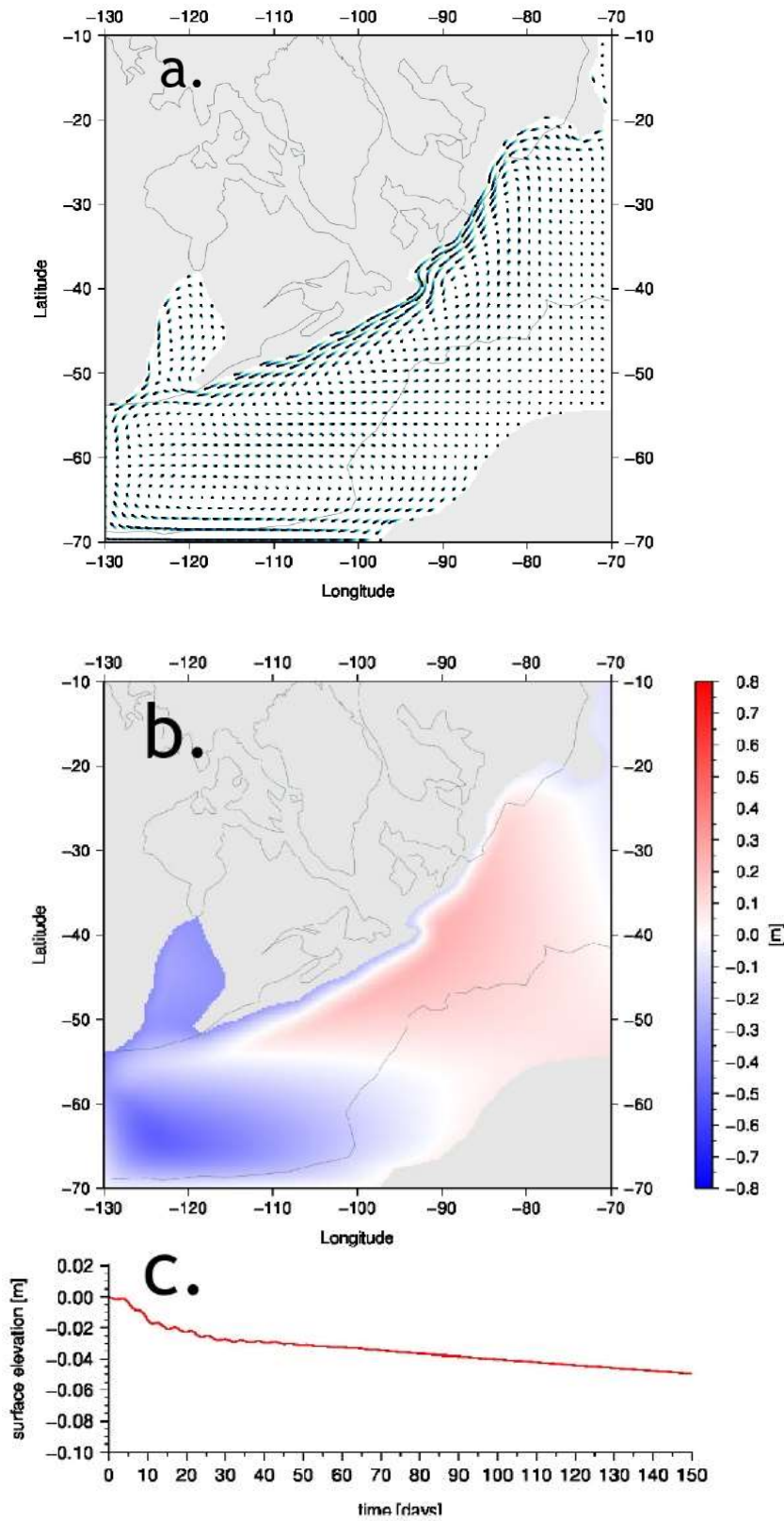


Fig. 4.13: Effect of a net westward flow (throughflow) of 5 Sverdrup: a) depth-averaged velocity pattern of an Emsian basin geometry with an idealized zonal wind stress and uniform depth of 200 meters, b) mean surface elevation and c) surface elevation time series for a run of 150 days.

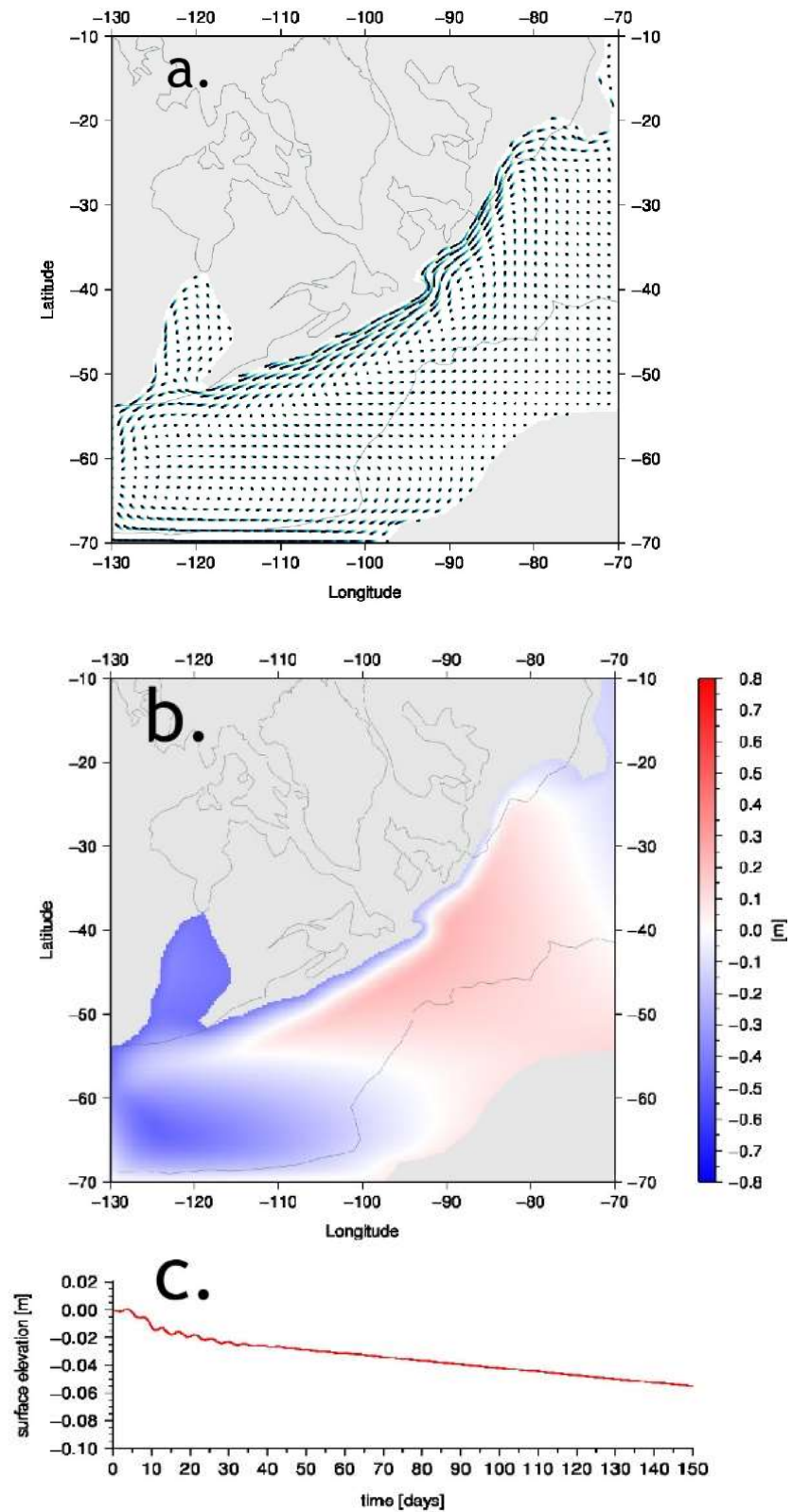


Fig. 4.14: Effect of a net westward flow (throughflow) of 7 Sverdrup: a) depth-averaged velocity pattern of an Emsian basin geometry with an idealized zonal wind stress and uniform depth of 200 meters, b) mean surface elevation and c) surface elevation time series for a run of 150 days.

4.3 Effect of the applied wind stress

In order to analyse how much the current velocity pattern is influenced by the applied wind stress, several different wind stresses were tested and compared to the idealized zonal wind stress scenario of the reference experiment (described in section 3.2.4).

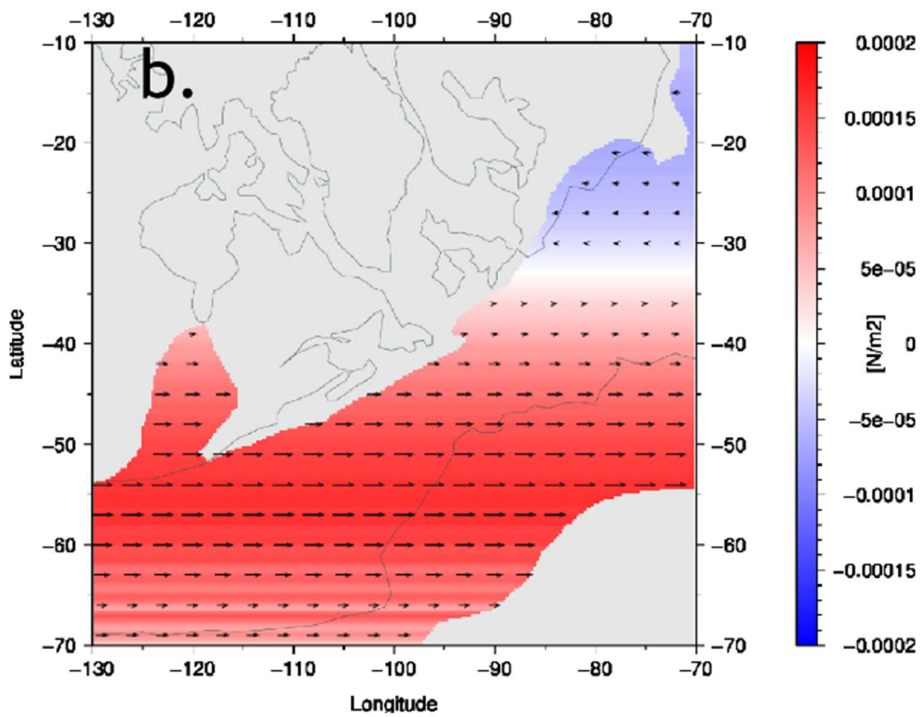
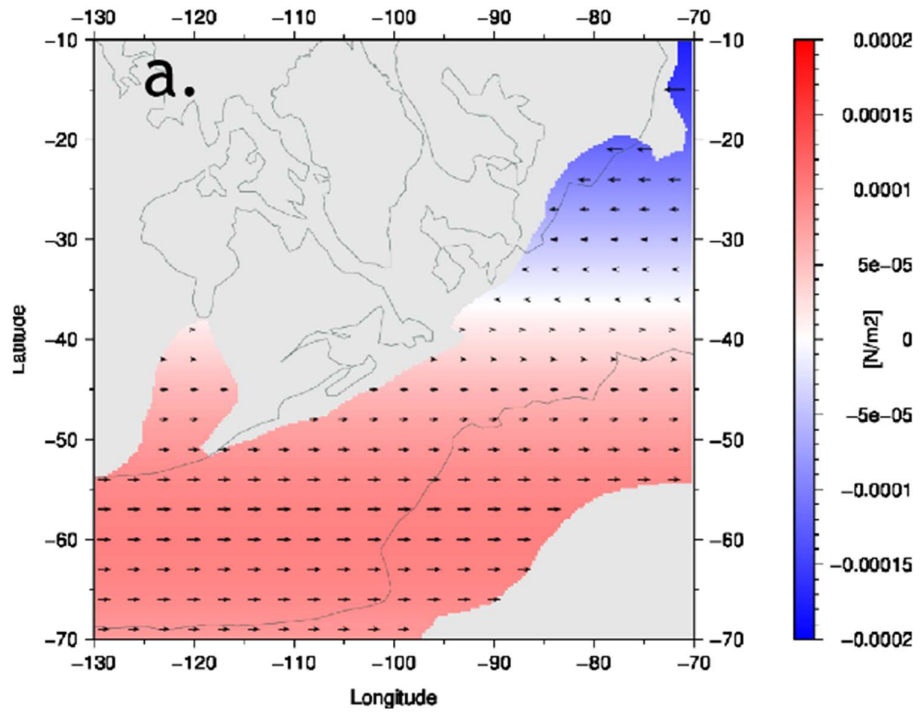
The experiment forced with a present-day zonal wind stress taken from satellite data is depicted in Fig. 4.15b. It shows eastward wind stresses between 10-30° south latitude, after which the wind stress reduces to zero at an inflection point and turns eastward from 35° south latitude onwards. The highest wind stresses are reached between 50-60° south latitude, with a maximum of 1.6×10^{-04} Nm/kg. There are some bands in the region between 60-70° south latitude which are an artefact from satellite data processing.

The resulting current velocity pattern in Fig. 4.16b shows how an applied present-day zonal wind stress still generates a strong current along Laurussia, although the current does not reach as far along the Laurussian margin as in the reference experiment. The northern gyre is overall similar to the Emsian reference experiment, but the southern gyre shows a different pattern. Although still flowing as a clock-wise cell, the gyre is difficult to interpret due to the aforementioned artefacts which also cause similar bands to appear as in Fig. 4.15b.

In the second experiment, a uniform eastward wind stress of 0.976×10^{-04} Nm/kg is applied to the model. Fig. 4.16c shows how a uniform eastward wind causes one single anti-cyclonic gyre to develop throughout the basin. Overall, the water mass flows along Gondwana in the south-western direction and picks up speed as it reaches the southern boundary of the model. This speed remains constant as it passes the Kaskaskia sea and picks up more speed along the remainder of the Laurussian margin up to 25° south latitude. The gyre in the Kaskaskia sea in this experiment also flows in the clockwise direction and at much lower velocities. As with the reference experiment, a strong current is still present at the western margin of the ocean basin. In this case, it flows in the opposite north-eastern direction due to the eastward wind.

In the third experiment within this series, a uniform meridional wind stress is applied in the northward direction. This has resulted in an overall quiescent ocean with very slight increases in velocity at the Laurussian margin as seen in Fig. 4.16d. As with previous experiments, a slight increase in velocity can be observed at the south and south-east boundary of the model. The figure shows that the effect of meridional wind results in very low velocities overall and can be considered negligible.

Two aspects of the applied wind stress were tested in the model: how realistic the applied idealized wind stress function was (also zonal vs meridional) and how sensitive the model was to large changes in the applied wind (zonal uniform wind stress).



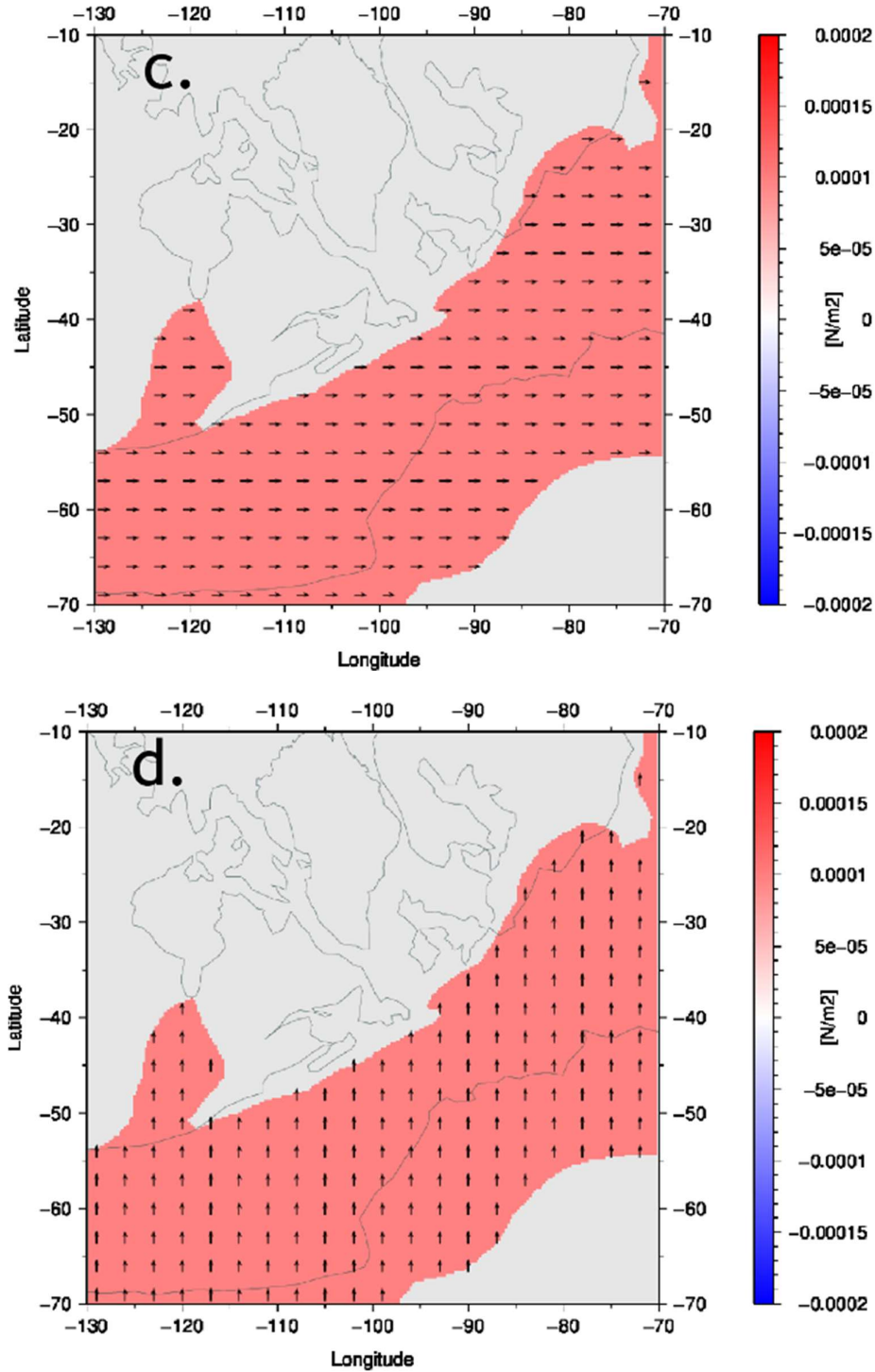
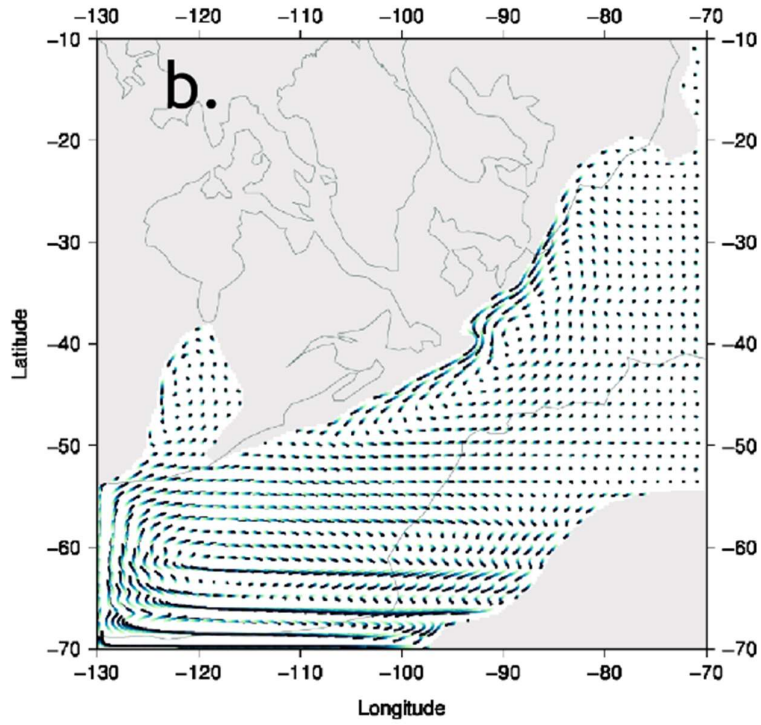
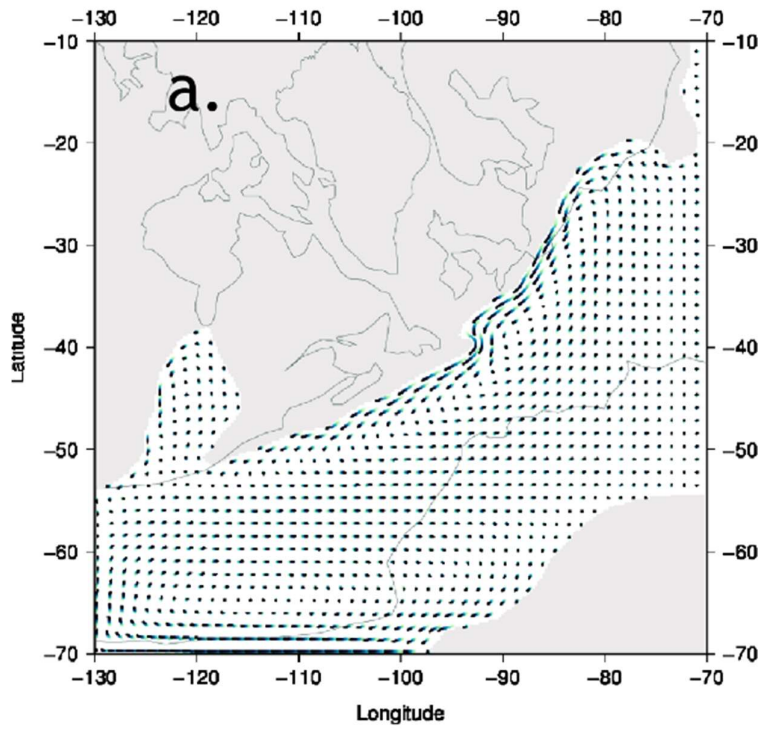


Fig. 4.15: Wind stress patterns applied to an Emsian configuration with uniform depth showing the a) idealized zonal windstress, b) present-day windstress from satellite data, c) uniform zonal windstress and d) and uniform meridional wind stress.



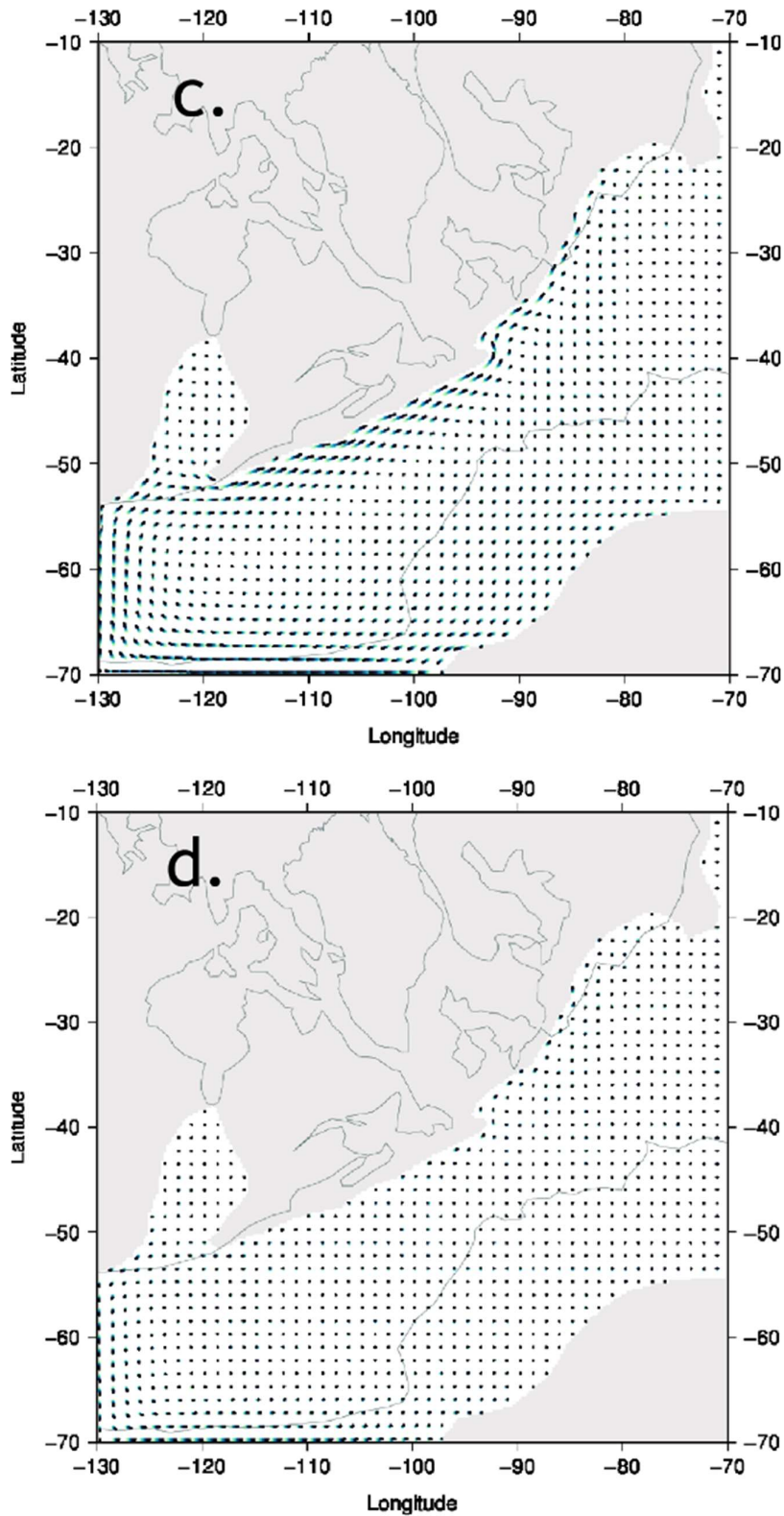


Fig. 4.16: Effect of variable wind stress on surface current pattern, showing the depth-averaged horizontal velocities resulting from a) an applied idealized zonal wind stress, b) present-day wind stress, c) uniform zonal wind stress and d) and uniform meridional wind stress.

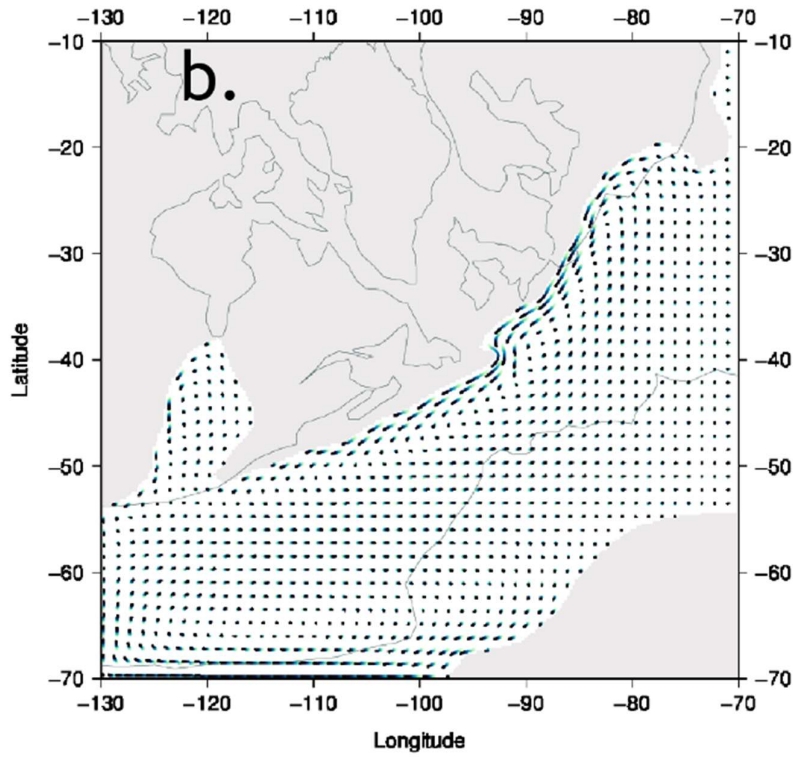
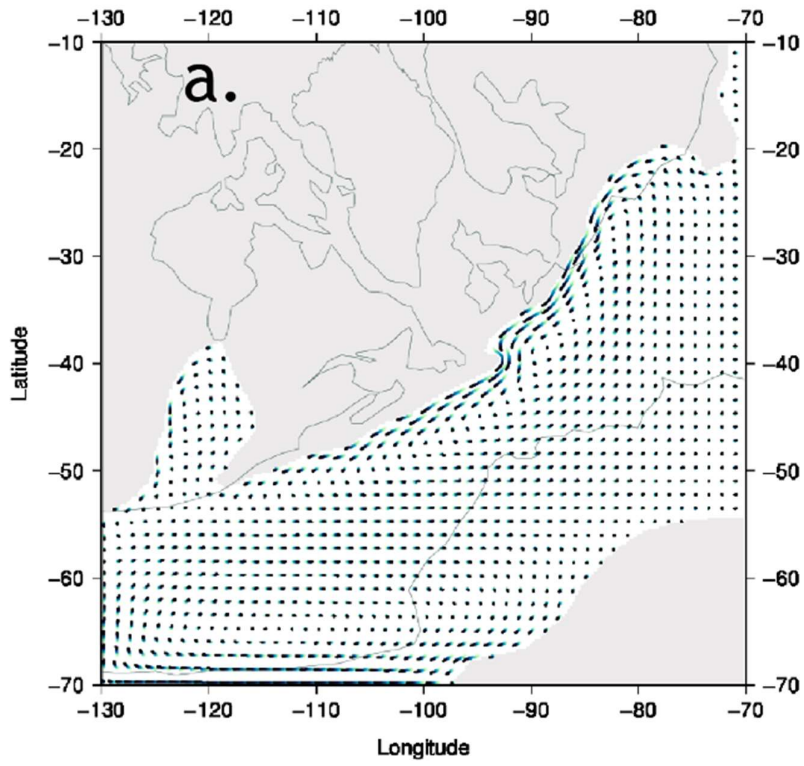
4.4 Effect of the Coriolis parameter

In this experiment series, we analyse the difference in surface current patterns when the applied Coriolis parameter is adjusted present-day, Devonian, uniform, or zero values (see section 3.2.5). The experiments are otherwise identical to the Emsian reference experiment.

Fig. 4.17b shows the current velocity pattern when the Coriolis parameter has been adjusted to a Devonian earth rotation rate, resulting in a smaller Coriolis parameter. Little difference is seen in the velocity pattern itself when comparing to the reference experiment with a present-day Coriolis parameter. The main features of the reference current velocity pattern are retained. The two gyres are generated with a strong current along Laurussia and the southern and south-eastern boundary of the basin. The decreased Coriolis effect is mainly reflected in the overall basin velocities and velocities are lower compared to the reference experiment.

Fig. 4.17c shows how the implementation of a uniform Coriolis results in a more symmetric distribution of velocity on both the eastern and western sides of the gyres. The currents at the Laurussian margin and at the south-eastern basin boundary are still the strongest. However, high velocities are no longer concentrated at the western boundaries but can be seen on the eastern boundaries of the gyres as well. In the northern gyre, for example, the water mass that reaches the Gondwanan margin below -55° has higher velocities in the north-eastern direction than in the reference experiment. In the southern gyre, as the water mass at the Gondwanan boundary at -60° is deflected to the south-west, velocities increase. Higher velocities are generated at the eastern boundary of the Kaskaskia Sea as well.

In Fig. 4.17d, the velocity pattern is generated with a Coriolis parameter set to zero and the basin is therefore not subjected to the Coriolis force at all. The velocity pattern that is generated is similar to the uniform Coriolis experiment in Fig. 4.17c, with the main difference being that higher velocities are reached at the eastern and western boundaries of the gyres. Eastern boundaries, like in the previous experiment, are subjected to higher velocities and higher velocities are therefore reached at the Gondwanan boundary. The Coriolis force has no influence in this experiment. The current at the western boundary remains the strongest suggesting that wind plays an important role in the WBC phenomenon as well.



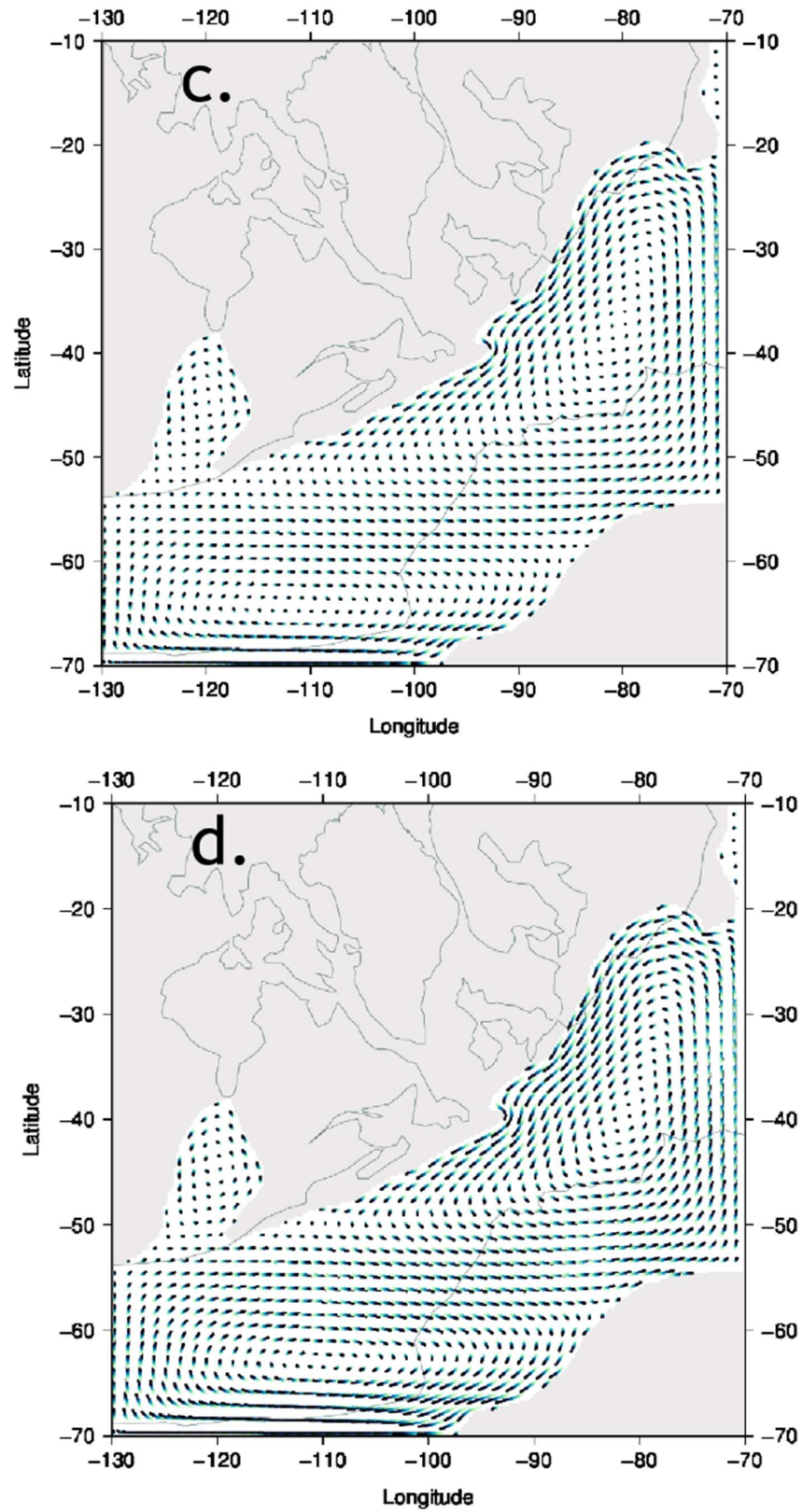


Fig. 4.17: Effect of a varying Coriolis parameter on the surface current pattern. Resulting depth-averaged horizontal velocities after applying the a) present-day Coriolis parameter value, b) Devonian value, c) uniform value and d) zero Coriolis parameter.

5 DISCUSSION

5.1 Model limitations

The model configurations used in this study have several important limitations which should be considered when reviewing and discussing results. Main limitations include the boundary effects, modelling dimensions, and the temporal as well as spatial scale of the model.

The modelled Rheic Ocean represents an ocean basin which was part of a much larger system and which would have connected oceanic waters from the Paleotethys Ocean at its eastern boundary and Panthalassa Ocean at its western boundary. In this study, however, a limited area model was used where the Rheic basin was analysed in isolation, which made it necessary to specify the water mass exchange at boundaries in areas where the basin is not already bound by land. In turn, the interaction between the water mass and these virtual boundaries influenced both the location and speed of currents close to the boundary areas.

The basin has artificial boundaries in the areas not bounded by land; at the north-east, east, south, and south-west edges of the basin. The greatest boundary effects were observed at the southern and western edges of the Rheic Ocean, especially evident in the experiment where solely meridional wind forcing was applied (Fig. 5.1). In this experiment, nearly zero flow results in all other areas of the model while higher velocities are still reached at the south and southwestern boundaries of the basin. Higher velocities were likewise generated at the southern and southwestern boundaries of the Emsian, and to a lesser extent Famennian, experiments.

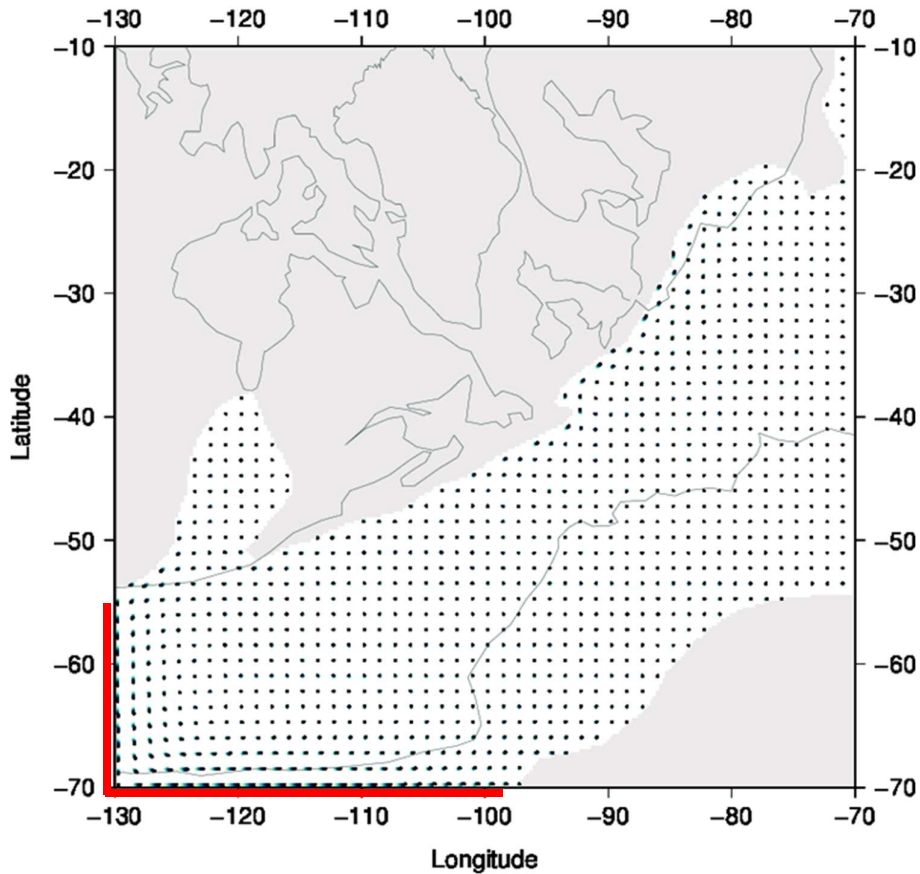


Fig. 5.1: Modified version of the meridional wind stress experiment shown in Fig. 4.16. Red lines highlight areas subjected to the greatest boundary effects.

The southern model boundary cuts off the Rheic before reaching the actual southwestern Amazonian shelf which would, in fact, have been further south. The higher velocities that can be seen at the southern model boundary are therefore expected to have occurred further southward. Likewise, the western boundary would have been an open connection to the Panthalassa Ocean. The current which is deflected northwards at the western model boundary would most likely not have been deflected but would have continued westward into the open ocean. The water reaching the Laurussian shelf would, therefore, have come from further east rather than the south as shown in the model results. The water masses at the southwestern edge of the Rheic basin are supplied by this deflected current and are also expected to have had much lower velocities than model results suggest. Another location where the boundary affects the circulation is at the western edge of the Kaskaskia sea. In several of the land-sea distributions used in the model, the western edge of the Kaskaskia sea was cut off at the model boundary, while it would have reached further west (shown in Fig. 5.2).

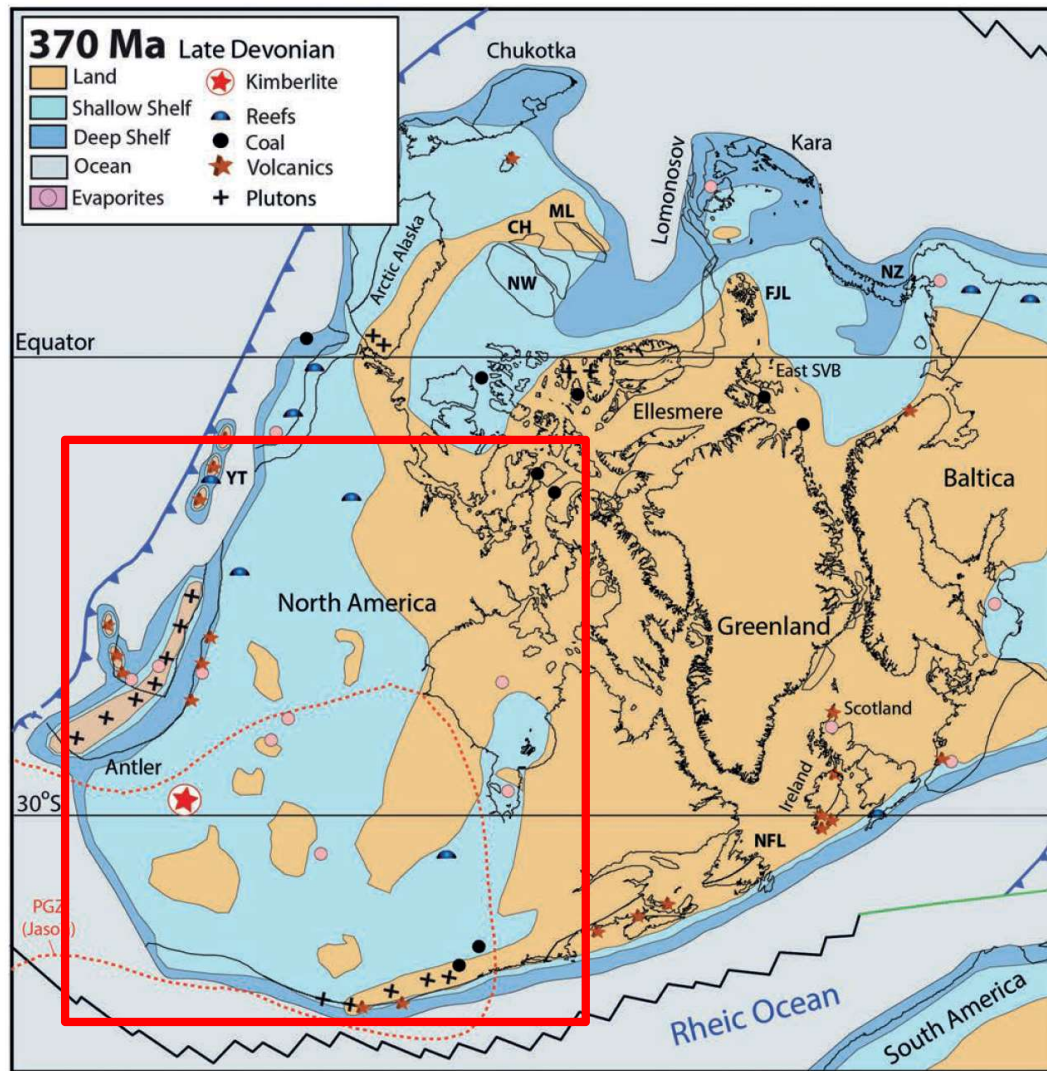


Fig. 5.2: Figure showing the full extent of the Kaskaskia sea, indicated by the red box. Modified from Torsvik and Cocks (2016).

All in all, the boundary affects the current by adding to the velocities already generated by the wind stress curl in the region, causing deflected strong currents. It should therefore be kept in mind when analysing the potentially erroneous high velocities and current directions in these regions.

Seeing as this is a first study, the decision was made to begin with a large-scale model of the entire Rheic basin prior to being able to model the circulation at the scale of epeiric and epicontinental seas such as the Rhenohercynian Ocean. The modelled area eventually spanned an area of roughly 44,000,000 km² at a resolution of ¼°. Using a scale this size allows the model to be compared to more schematic ocean circulation models. It is additionally useful for a general understanding of the factors affecting the surface current pattern within the Rheic basin and gives ideas on the possible interaction between the Rheic and bordering Panthalassa and Paleotethys oceans which could in turn influence the smaller oceanic basins. On the other hand, it does limit the uses of the model to general observations as analysis of smaller-scale processes such as eddies, monsoons, or storms require a higher resolution, more paleogeographic detail, additional forcing such as vertical density gradients, or a dynamic instead of steady-state model. Research could benefit from the incorporation of such smaller-scale processes as the frequent occurrence of

monsoons and storms due to a high Devonian seasonal variability is evidenced in Devonian deposits and shown to have played an important role in mid-Paleozoic ocean circulation (Thorez and Dreesen, 1986; De Vleeschouwer, 2015; Tait, 2000; Narkiewicz et al., 2015). These processes, however, would additionally require three-dimensionality to allow for the incorporation of vertical movements. Using a three-dimensional model could also make the analysis of the thermohaline circulation as well as coastal up- and downwelling possible which could be of interest as oceanic overturning of anoxic waters is seen as a possible cause of the Devonian mass extinctions such as the Hangenberg event (Caplan and Bustin, 1999, Chen et al., 2012).

5.2 Main parameter sensitivity

Throughout the study, several aspects of three main parameters were tested, namely the paleogeography, wind stress and the Coriolis force. The process-based analysis of these parameters led to the identification of the most influential factors on the modelled circulation pattern, namely the bathymetry, throughflow, and applied zonal wind stress. The Coriolis parameter and meridional wind stress were found to have had a relatively insignificant effect. There was little difference in the circulation pattern between the modern Coriolis parameter and the expected Devonian Coriolis parameter. Results showed that the meridional wind stress generates a negligible amount of flow, thereby justifying the omission of meridional wind effects in the idealized wind stress function. Of the three paleogeographic aspects tested, the influence of the land-sea distribution had less influence on the general circulation pattern but was still found to have some local influence, which will be discussed in section 5.4.

5.2.1 Bathymetry

The generated bathymetry results in Fig. 4.10 and Fig. 4.11 showed that noticeable velocities were not reached unless the depth of the ocean basin was less than 200-300 meters, which occurred at the continental and island coastlines. A depth greater than 200-300 metres resulted in a diffuse circulation pattern, with no overall current direction. The two-dimensionality of the model leads to depth-averaged velocities, which are expected to have caused a diffuse pattern. Nonetheless, model results do suggest that variations in depth have a strong influence on the generated surface circulation.

The generated bathymetry used in this study is a rough estimate of the Rheic bathymetry and was mainly intended for identifying the sensitivity of the model. The generated bathymetry does incorporate several features such as the Rheic Ocean and a subduction zone that is closer to Laurussia than Gondwana. The bathymetry at the Laurussian shelves, however, causes narrower and deeper shelves than suggested in literature. For example, one study that focused on a smaller basin within the Gondwanan shelf suggested that the intrashelf Mader Basin did not reach depths greater than 20 metres (Jakubowicz et al., 2019). The Laurussian shelf is also often shown to cover a much larger surface area of the European segment of Laurussia than in the land-sea distributions used in this model, as shown in Fig. 5.3 (Hüneke, 2006; Stets and Schäfer, 2011).

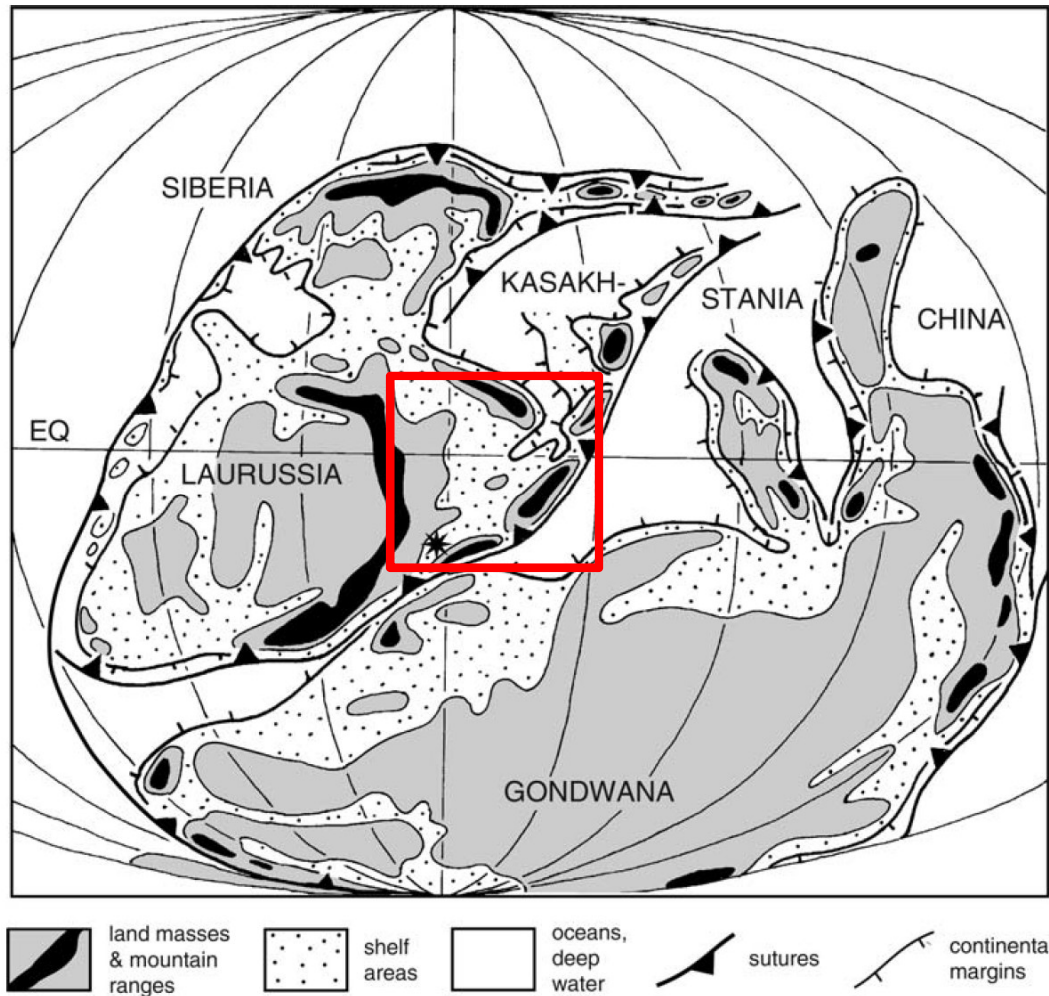


Fig. 5.3: Early Devonian paleogeographic reconstruction, the red box highlights how in this reconstruction Europe was predominantly one large shelf. Modified from Stets and Schäfer (2011).

Furthermore, the depth of the Rhenohercynian Ocean is an uncertain parameter as it is not sure what type of basin it was. In this study, it was set to a depth of 3500 metres to represent a back-arc basin. In Hüneke (2006), on the other hand, it is suggested to be a failed rift with a depth of 200-1000 meters.

The sensitivity of the model to the bathymetry lead to the conclusion that future model expansions would require a more refined bathymetry. To achieve this, a choice must first be made whether to focus on a detailed, smaller-scale local bathymetry or a more generalized, large-scale global bathymetry. In both cases, the overall effects of the bathymetry on the circulation would be better represented by a three-dimensional model. This would, for example, allow for the distinction of flow directions at different depth levels as opposed to the depth-mean result from the two-dimensional configuration used in this study.

Using a smaller, basin-scale bathymetric reconstruction

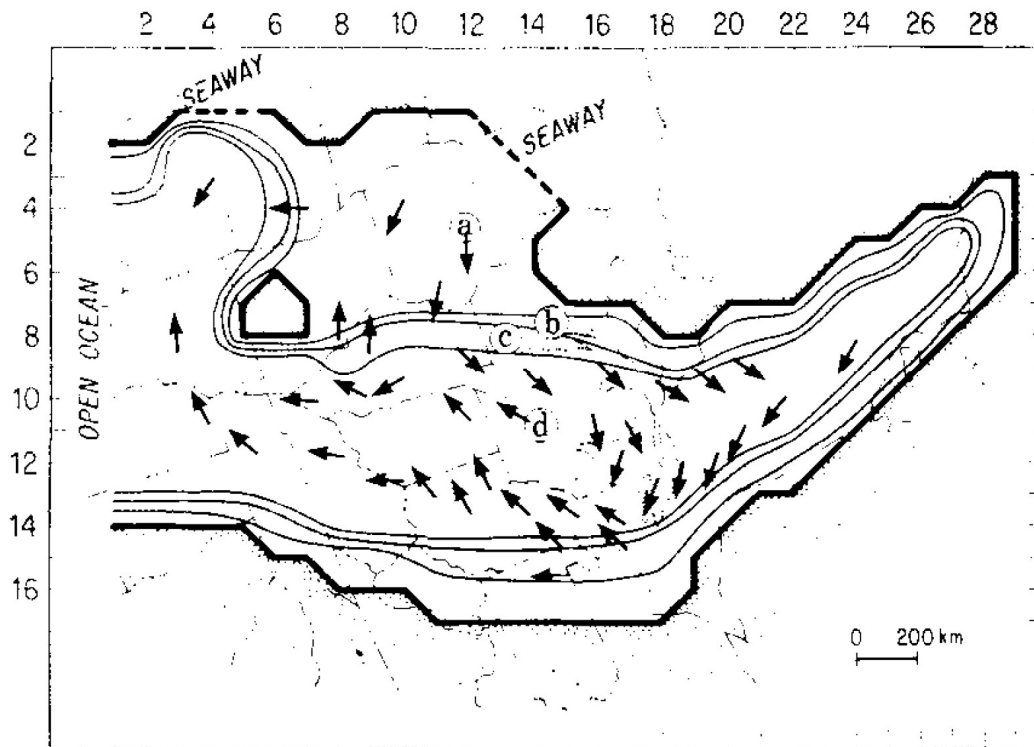


Fig. 5.4: Example of a smaller basin-scale study. Showing circulation within the Upper Devonian Catskill Sea. Modified from Slingerland (1986).

An option which would result in a more refined bathymetry would be to apply the model on smaller oceanic basins or shelfal areas within the Rheic Ocean. This would be beneficial as the modelled results would be easier to constrain with geological observations since, although no direct evidence of the Rheic deep-sea environment remains, the number of studies that study smaller basins along the Rheic shallow shelves are numerous.

Several regions that have been the subject of sedimentary, tectonostratigraphic and biotic studies are for example the Tafilt and Mader basins in the Moroccan Variscides (Dopieralska, 2009), the Ahnet and Mouydir basins in Algeria (Lüning et al., 2004; Wendt et al., 2006), the Ardennes area including Condroz Shelf in Belgium (Paproth et al., 1986; Thorez et al., 2006), the Orcadian basin in Scotland (Marshall et al., 2007), the Appalachian, Catskill and Illinois basins in North America (Sageman et al., 2003; Smith and Read, 2000), and the Rhenohercynian basin (Stets and Schäfer, 2011). Other studied localities, not including the terrane margins such as Iberia and Armorica, are found along the Rheic margins in present-day Peru and Bolivia (Reimann et al., 2010), as well as Poland (Dopieralska et al., 2006; Matyja, 2009). The data presented in these studies provide information on a more detailed bathymetry, and several incorporate the local features such as the local tectonic situation shown in Fig. 5.3 for the Rhenohercynian basin. In this publication by Stets and Schäfer (2011), for example, local tectonics were incorporated in sediment supply directions in their depositional models. The influence of tectonics on the local circulation was also highlighted by Wendt et al. (2006), where diverging paleoflow orientations in Givetian calcareous facies within the Azel Matti Ridge (Algeria) are thought to be related to irregular seafloor topography.

Modelling these smaller-scale basins would require tidal forcing, as it is an important influence on shallow-sea environments. This is also shown in the numerical study on the Catskill Sea by Slingerland (1986) (Fig. 5.4).

To minimize the uncertainty caused by unknown values of throughflow and boundary effects, it would be useful to use a model nested in a larger model. The modelled basins could, therefore, make use of a larger-scale model such as the one presented in this study, or even a global-scale model.

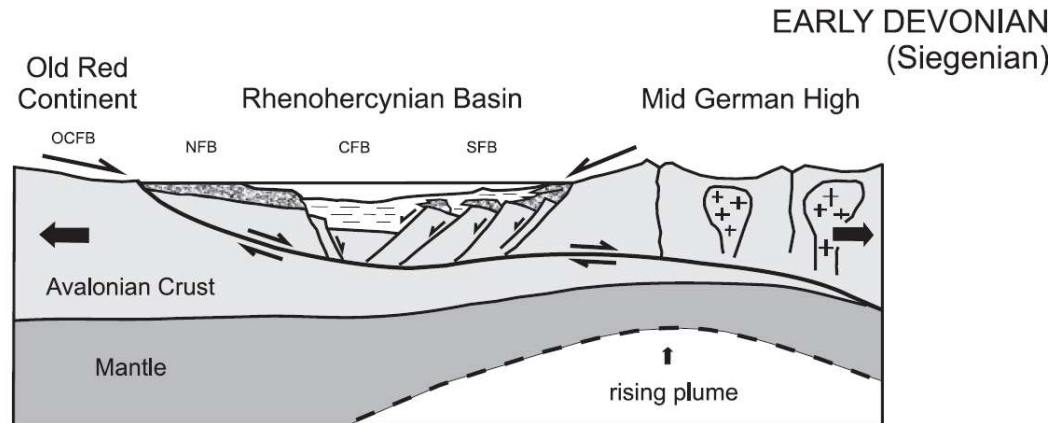


Fig. 5.5: Cross section of the Early Devonian Rhenohercynian basin that serves as an example of how local tectonics can be incorporated into basin-scale models (Stets and Schäfer, 2011).

Using a large, global-scale bathymetric reconstruction

Originally, the smaller-scale model of the Rhenohercynian Ocean was found to be more uncertain in terms of paleogeography, which is why a larger-scale model of the Rheic Ocean was opted for instead. Although bathymetry might be better constrained by the small-scale model of a shallow basin as previously discussed, it might also be beneficial to model the larger, global scale circulation of the mid-Paleozoic. The reason for this is related to the fact that small-scale basins provide more bathymetric detail: there is no evidence of the deep-sea conditions within the Rheic Ocean, and precisely this issue could make a large-scale model desirable as modelling provides a unique insight into an otherwise unknown scenario. To use a large, global-scale model but improve model results, a bathymetry could be implemented that is based on a more refined tectonic plate model. The tectonic complexity of the opening and closure of the Rheic Ocean is still widely debated, which is expected to be the same for the Panthalassa and Paleotethys ocean. Despite this obstacle, an approximate estimate of the bathymetry could be made using the relationship between flexure and age of oceanic crust as shown in Fig. 5.6 to create a bathymetric model. Although not yet available for mid-Paleozoic times, Fig. 5.7 shows a reconstruction of oceanic age by Müller et al. (2016) which could ideally be used. Seeing as interactive platforms such as GPlates promote the development of plate tectonics further and further back in time, a similarly detailed global tectonic reconstruction may become possible in the future.

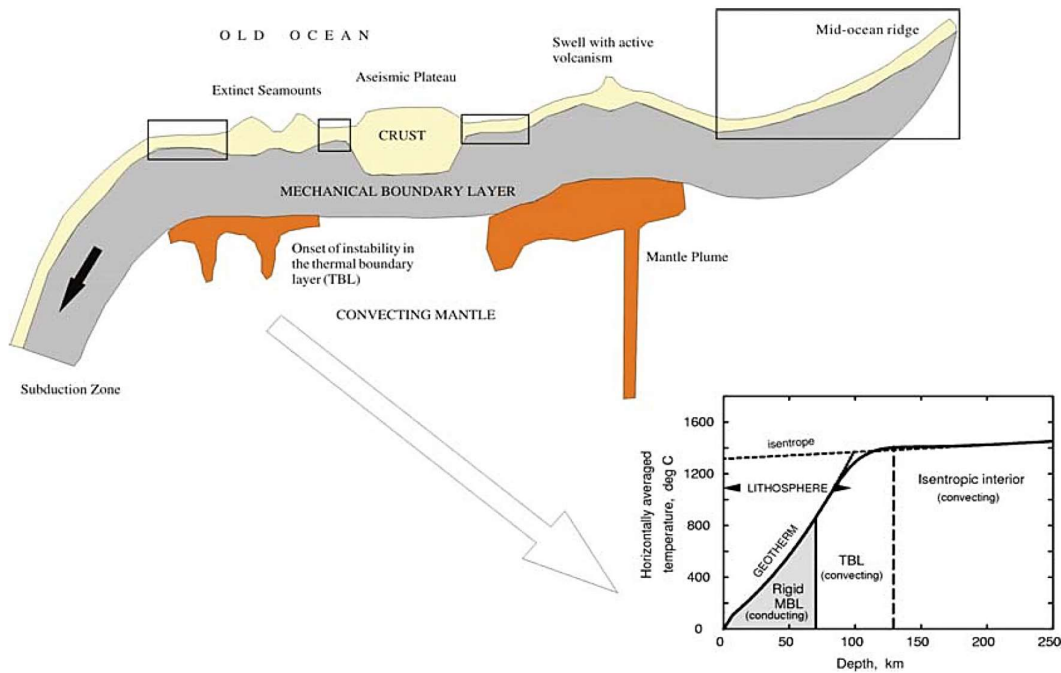


Fig. 5.6: Illustration of the relationship between age, flexure, and depth of oceanic lithosphere (Crosby et al., 2006).

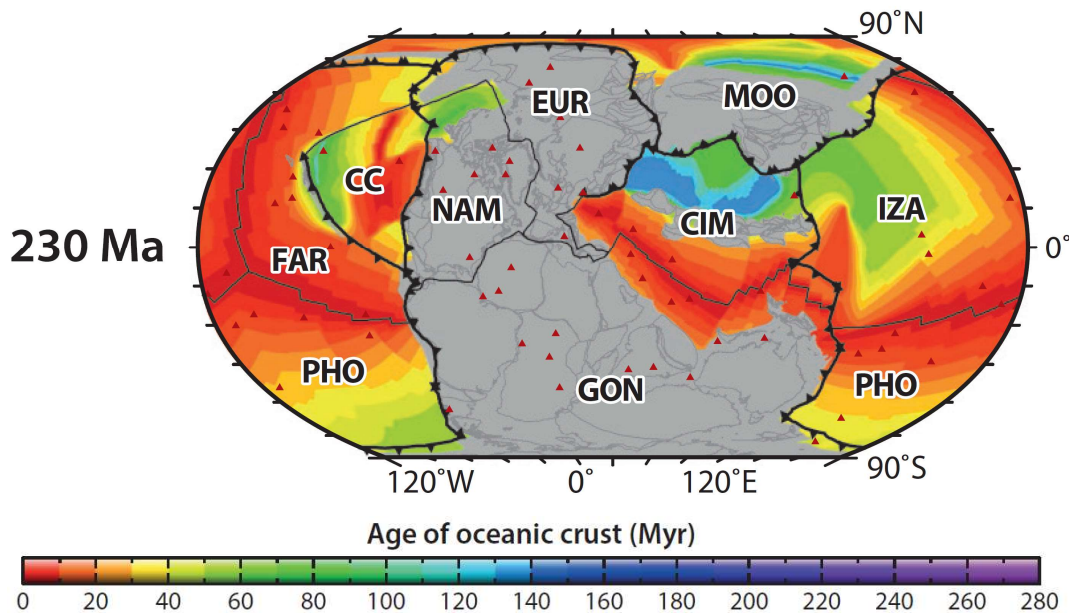


Fig. 5.7: Age-area distribution of oceanic crust at 230 Ma. Modified from Müller et al. (2016).

The approximated bathymetric model could then be used for a global circulation model which would mainly focus on the large global circulation patterns and ignores the smaller patterns along the bathymetrically-sensitive ocean margins. An example of such a model is the Ordovician numerical model by Pohl et al. (2016) shown in Fig. 5.8. The insight obtained with a global-scale model would provide more valuable insight into the Late-Devonian extinctions and global climate change which have been linked to anoxia (Caplan and Bustin, 1999; Chen et al., 2013; Lüning et al., 2004; Marshall et al., 2007; Menor-Salván et al., 2010), overturning and rise of toxic water

(Caputo et al., 2008), and to changes in thermohaline circulation by the deflection of warm currents by closure of the Rheic passage (Smith and Read, 2000) (see Fig. 1.5 and Fig. 5.9). Ideally, this would then be combined with a three-dimensional model and the incorporation of vertical density gradients which could then be coupled to reconstructed Sea Surface Temperature (SST) and sea-level curves to model the global overturning of waters or exchange of warm and cool waters between, for example, the two Rheic gyres that developed in the Emsian reference experiment (Fig. 4.4a).

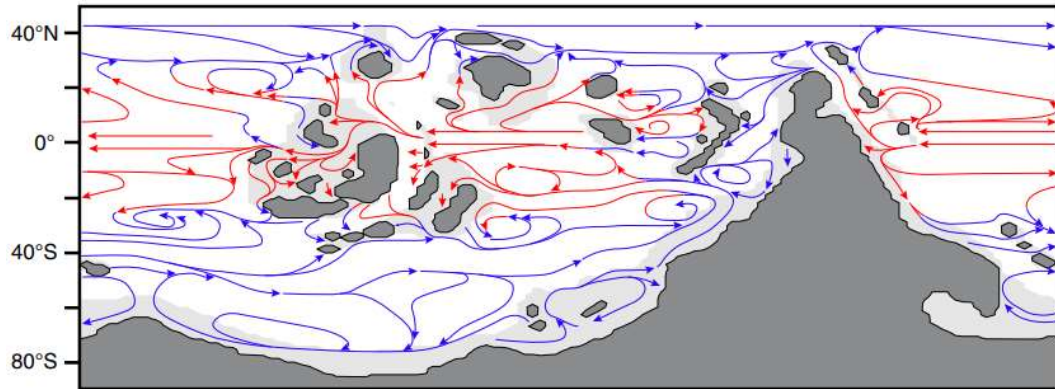


Fig. 5.8: Example of a global scale model, showing a Late Ordovician (440 Ma) circulation pattern from Pohl et al. (2016).

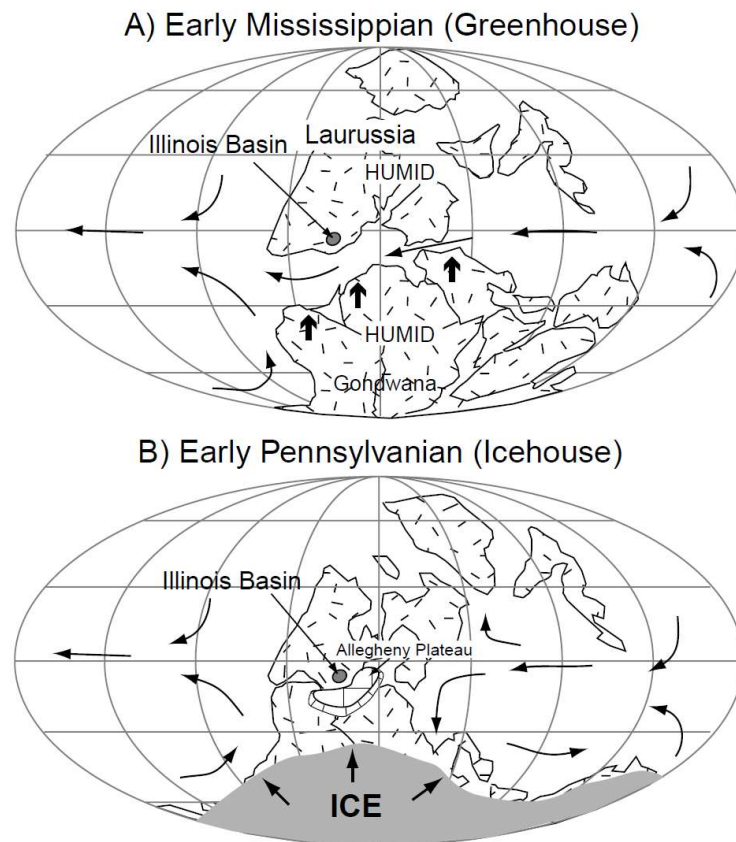


Fig. 5.9: Effect of Rheic closure on the global circulation (Smith and Read, 2000).

5.2.2 Throughflow

Another factor of influence on the generated circulation pattern is the westward throughflow. This throughflow was implemented in the model to capture the function of the Rheic Ocean as a connecting ocean. The model results have shown that an increased throughflow causes higher current velocities, without altering the circulation pattern itself. An issue lies in the fact the actual transport of water at the boundaries of the Rheic with its bordering oceans remains unknown. Transport values of 7, 5 and 1 Sverdrup were therefore chosen to represent high, normal, and low transport values in the model as (see section 3.2.3). The sensitivity of the model to the throughflow highlights the need for more investigation into the possible fluxes between the Rheic, Paleotethys and Panthalassa oceans. The possible boundary conditions in the Princeton Ocean Model are numerous (Mellor, 2004). For example, a potential implementation both an in- and outflow at the individual boundaries rather than an overall throughflow could also be explored. Another option would be to use the aforementioned nested model approach. This can be done by nesting a smaller basin in the Rheic Ocean model constructed in this study, or by nesting the same Rheic Ocean model in a global model.

5.2.3 Applied zonal wind stress

The wind stress experiments showed that small changes in the applied wind stress caused significant changes in the circulation pattern. In this model which is forced solely by the wind stress, the wind pattern rules the formation of gyres, the position of the WBC, and horizontal current velocities within the basin. Additionally, wind stress and paleolatitude are interconnected and currents depend on the placement of the area of interest within the applied wind stress pattern. For example, the strength of the current reaching Gondwana was stronger for the Famennian land-sea distribution based on Torsvik and Cocks (2016) than for the Famennian configuration based on Dopieralska et al. (2009) due to the Gondwanan shelf being located at higher latitudes, thereby falling in an area within the wind stress pattern with higher wind stresses. Comparison of the idealized wind stress function to the modern-day observed wind stresses showed that the two curves were not a perfect fit. Chereskin and Price (2018) show an alternative idealized wind stress function, where the wavelength used in equation 3.4 is reduced to $\pi/2$ instead of $2/3\pi$ (Fig. 5.10). Applying this wavelength results in a slightly better fit to the observed wind stresses (blue in Fig. 5.11). Alternatively, an idealized wind stress function with no asymmetry could be used (solid black in Fig. 5.11).

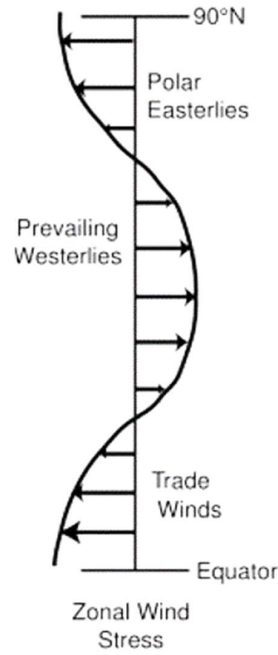


Fig. 5.10: Idealized surface wind in the northern hemisphere, modified from Chereskin and Price (2018).

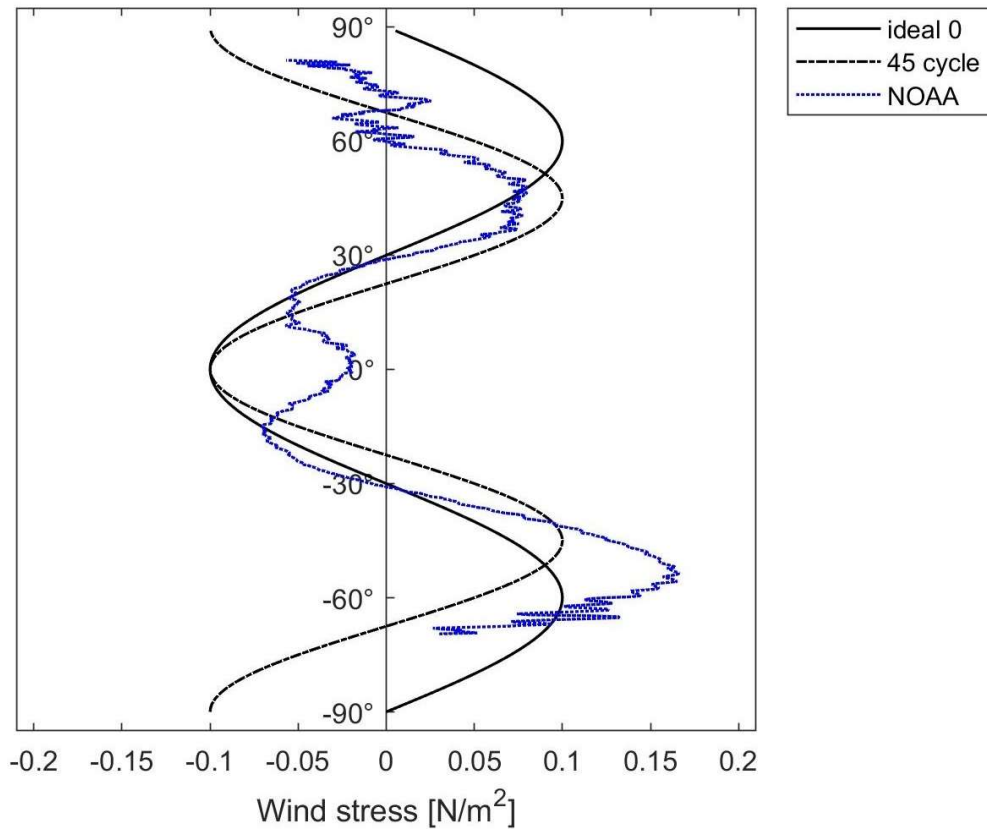


Fig. 5.11: Modern-day winds stresses from the NOAA database (blue) compared to the idealized wind stress curve with an alternative wavelength of $\pi/2$ (dashed black), and curve with no asymmetry called “ideal 0” (solid black).

Another feature of wind stress expected to have an influence is the effect of land mass on the wind stress. In the Devonian continental configuration, continents were concentrated in the Southern Hemisphere. The possible influence this would have had on the wind stress pattern over the Rheic Ocean could consequently be of importance and would require further testing.

5.3 Comparison to conceptual circulation models

The numerical model results generated in this study show circulation patterns that are comparable to available schematic reconstructions of mid-Paleozoic oceanic circulation. In section 2.3.1, four main circulation patterns were identified from six schematic reconstructions. These include the reconstructions by Dopieralska (2009) Fig. 1.6), Hüneke (2006) (Fig. 5.12), Jakubowicz et al. (2019) (Fig. 5.13), Kiessling et al. (1999) (Fig. 2.13), Oczlon (1990) (Fig. 2.12), and Paproth et al. (1986) (Fig. 1.4). The model results will be compared to these four patterns in the sections below.

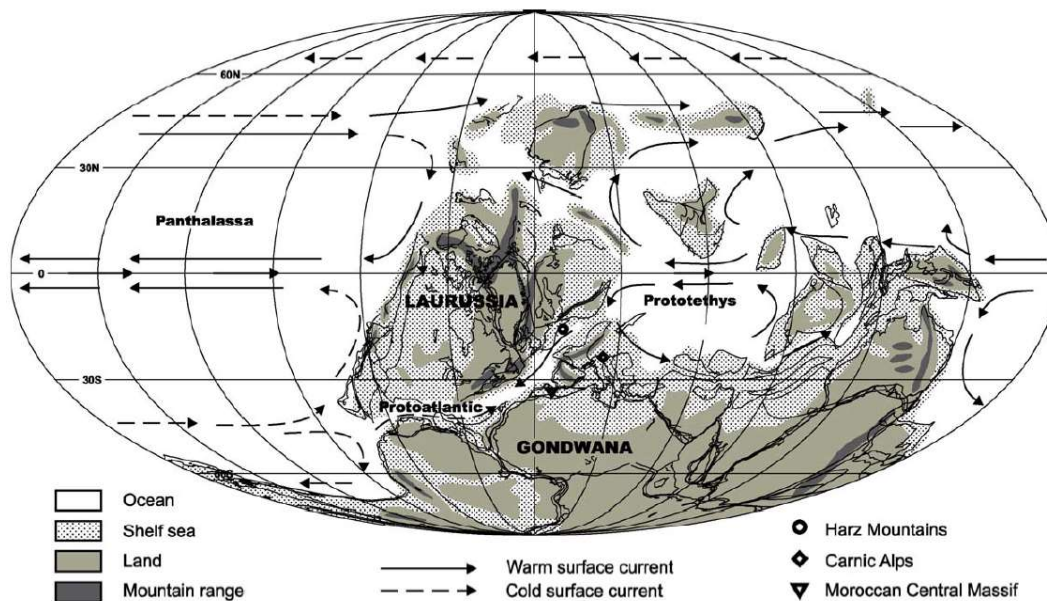


Fig. 5.12: Global pattern of oceanic surface circulation in the Givetian-Frasnian epochs, modified from Hüneke (2006).

1.) Gyre patterns within the Rheic

Cyclonic and anti-cyclonic gyres were generated within the Rheic Ocean in the Emsian as well as Famennian experiments in this study. Similarly, in the reconstructions by Hüneke (2006) and Kiessling et al. (1999), anti-cyclonic gyres occur at lower latitudes and cyclonic gyres occur at higher latitudes. In their schematic reconstructions, however, the northern anti-cyclonic gyre is considered to have been deflected upon contact with the ATA at the margin of Gondwana. The southern, cyclonic gyre is also not shown to have been generated in the narrow Rheic Ocean, and both gyres are therefore instead limited to the Panthalassa and Paleotethys basins. The difference between schematic and modelled circulation, in this case, is most likely due to a difference in chosen plate reconstruction, causing the Rheic Ocean in the schematic reconstructions to be much narrower, and at lower latitudes, than in the modelled experiments.

The Rheic circulation generated through the model in this study is more similar to the reconstructions by Dopieralska (2009), Jakubowicz et al. (2019), and Oczlon (1990). These reconstructions also place the Rheic Ocean at lower latitudes, but they do show the formation of

an anti-cyclonic gyre within the Rheic Ocean. A cyclonic gyre, however, is also not shown. Interestingly, large differences occur even between these three similar reconstructions. In the reconstruction by Jakubowicz et al. (2019) (Fig. 5.13), for example, a Mid-Devonian Rheic Ocean is shown with a closed western arm. This would be similar to the Tournaisian experiment in this study (Fig. 4.8), where one single gyre is generated within the basin. In the reconstructions by Dopieralska et al. (2006) and Oczlon (1990), the Rheic Ocean is still open to the Panthalassa Ocean. The inflow from the east shown in their reconstructions would correspond to the cyclonic gyre, which generates an eastward flow at latitudes near -60° (Emsian) and -50° (Famennian).

The similarity in faunas between Laurussia and Gondwana has been attributed to their connection by the Rheic Ocean, and studies may benefit from the added information on the anti-cyclonic and cyclonic gyres obtained through this study (Narkiewicz et al., 2015). For example, the lateral inflow of Givetian faunas into shallow basinal areas in present-day Algeria as described by Wendt et al. (2006) could be explained by the predominantly eastward currents formed along the southern edge of the anti-cyclonic or northern edge of the cyclonic gyre, which generated an eastward flow.

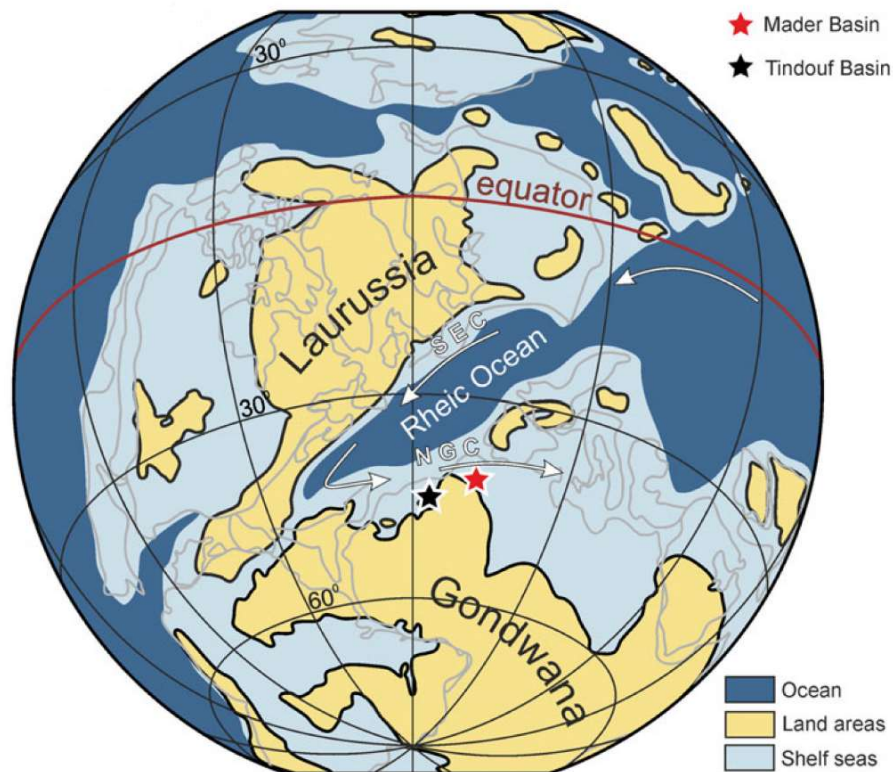


Fig. 5.13: Mid-Devonian seawater circulation from Jakubowicz et al. (2019) based on the schematic reconstruction by Oczlon (1990). The South Equatorial Current (SEC) and North Gondwanan Current (NGC) are located more southward in this reconstruction.

2.) Current direction along the Laurussian shelf

What can be said is that in general, the model results agree with the schematic reconstructions on the current direction along Laurussia. This current was termed the Western Boundary Current (WBC) by Paproth et al. (1986) and South Equatorial Current (SEC) by Oczlon (1990) and Jakubowicz et al. (2019), see Fig. 5.13 and section 2.3.1.

In the model results, this strong boundary current occurs along a great part of the Laurussian margin, justifying the assumption made by Paproth et al. (1986) that a WBC was of importance to the Condrosz shelf region on the redistribution of delta-lobe sediments. The model results also support the study by Jakubowicz (2018), in which the migration of several different conodonts and corals are attributed to a South Equatorial Current (SEC) that reached from the Urals to the south-eastern margin of Laurussia (Bruno-Silesian unit). The model results additionally show that the WBC originated in north-eastern Europe and reached the North American segment of Laurussia, which would facilitate a westward distribution of, for example, fauna from Europe to North America. In the Famennian (Late Devonian) experiments, the WBC even traversed nearly the entire length of the Laurussian margin. Yet, this connection between Europe and Laurussia does not seem to be as straightforward when looking at paleobiogeological studies focusing on the North American segment of Laurussia. For example, findings by Narkiewicz and Bultynck (2010) do report the distribution of the same conodont species from Poland to Iowa in the Middle Devonian, but Late Devonian research by Wicander (1975) shows an unexplained dissimilarity of microflora between Europe and Ohio. This disconnect could be related to smaller sea-level fluctuations and their effect on the connection between the Kaskaskia Sea and Rheic Ocean. It should, therefore, be noted that the land-sea distributions capture a rough estimate of paleogeographies over a large period of time. This low temporal resolution can, therefore, contrast with the higher resolution of the evidence recorded in the geological record.

3.) Current direction along the Gondwanan shelf

The Emsian model results in Fig. 4.4 indicate a strong south-eastern current at the western-most margin of the Amazonian segment of Gondwana. This is supported by paleocurrent indicators from Upper Silurian to Middle Devonian Peruvian sandstones, indicating a south-eastern current direction according to Reimann et al. (2010). The location of these sandstones matches the location of the highest velocities within the south-eastern current seen in the model results.

It should be noted that model results are difficult to directly compare to the schematic reconstructions in general, as evidenced by previously discussed differences in latitude as well as ocean basin geometries. This is also in part due to the land-sea distributions used in this study, which are based on the paleogeographic reconstructions by Torsvik et al. (2012) and Torsvik and Cocks (2016). In their plate reconstructions, they use the Pangea-C configuration (see section 2.2). The reconstructions in the majority of the schematic reconstructions, on the other hand, are based on the Pangea-A configuration. Contrasting depictions of water depth is also of influence, causing certain regions to be shallower than others in some reconstructions despite the use of a similar plate configuration. In the circulation reconstructions by Hüneke (2006) and Kiessling et al. (1999), for example, currents do not traverse the ATA while the reconstructions by Dopieralska (2009), Jakubowicz et al. (2019) and Oczlon (1990) show that they do.

We consider a scenario in which the model would have had no eastern and western model boundaries, such as in the case of for example a nested model approach. Model results would most likely show that the anti-cyclonic northern gyre would be bigger and reach farther to the east, into the Paleotethys Ocean. With regards to the cyclonic gyre, the strong current at the southern boundary would follow the Amazonian shelf as opposed to the virtual model boundary. This Amazonian shelf is expected to have been slightly further south. The southern, cyclonic gyre would also not be deflected northward by the specified western model boundary, but rather flow further west.

If the shelf of the North African segment of Gondwana had been incorporated in a model domain that reached farther east, the model results would most likely show a similar eastward current

along Northern Africa, as they currently show for the Amazonian segment. This would also support the reconstructions by Hüneke (2006) and Kiessling et al. (1999) which show an anti-cyclonic gyre in the Paleotethys. A Late Devonian eastward current direction in studies within the Moroccan Variscides is confirmed (Dopieralska, 2009; Jakubowicz et al., 2019), although according to Dopieralska (2009), this was not the case in the Famennian.

The modelled surface circulation along Gondwana allows for a preference between the schematic reconstructions. The more recent Late Devonian reconstructions by Dopieralska (2009) and Jakubowicz et al. (2019) (Fig. 1.6 and Fig. 5.13) are based on the reconstruction by Oczlon (1990) (Fig. 2.12), but contrary to the reconstruction by Oczlon (1990) they depict an eastern rather than a south-eastern current at the northern part of the Gondwanan margin. In this study, model results that use Late Devonian land-sea distributions (Fig. 4.5, Fig. 4.6, and Fig. 4.7) support the eastward depiction of the North Gondwanan Current, as the current is relatively strong at the northern, E-W oriented part of the Amazonian shelf and velocities rapidly decrease when the current bends around the eastern edge of Amazonia.

Preference over the use of the Pangea-A or Pangea-C configurations cannot be made. The position of Gondwana and Laurussia vary laterally, placing them within the same wind belt in either of the configurations. In both configurations we would, therefore, see similar current directions. In our model, for example, we see a south-eastern current at the easternmost Amazonian shelf. A similarly directed current is depicted at the Amazonian shelf when the Pangea-A configuration is used (Fig. 5.12).

4.) Interaction with Panthalassa and Paleotethys

The schematic reconstructions by Hüneke (2006) and Kiessling et al. (1999) simplify the exchange between Panthalassa and Paleotethys as a unidirectional inflow from the east and an inflow from the west. The circulation generated in this study show more detail and results show an anti-cyclonic gyre to be in connection with the Paleotethys Ocean, and a cyclonic gyre with the Panthalassa Ocean in the Emsian and Famennian experiments. These gyres combine between 50-60° south latitude, allowing for the exchange of waters from both oceans. Warm water carried by the anti-cyclonic gyre connected to the Paleotethys would be interchanged with cold water from the cyclonic gyre connected to Panthalassa. The reconstructions by Dopieralska (2009), Jakubowicz et al. (2019), and Oczlon (1990) are more congruent with model results as they incorporate the anti-cyclonic gyre that is in connection with the Paleotethys Ocean.

5.4 Contribution to mid-Paleozoic paleogeography

The second research question was aimed at determining whether the generated Rheic surface currents could be used as a possible aid to several mid-Paleozoic paleogeographic controversies (see section 2.2). The circulation generated in this study through numerical modelling indicates a correlation between land-sea distribution and current behaviour, namely an increase in current velocity. The following sections discuss whether this relationship could help determine terrane positions as well as the position of Gondwana, the two main controversies regarding the Rheic Ocean paleogeographic configuration.

1.) Inferring the paleoposition of Gondwana

Model results showed that current velocities increased on both sides of the Rheic Ocean when the ocean basin was narrower. This constriction was resulted from the convergence of the northern and southern continents as reconstructed in the Tournaisian configuration in Fig. 4.8, or by setting the shelf break as an artificial current barrier as in Fig. 4.9. In both cases, the effect of a narrow

Rheic results in higher WBC velocities and higher velocities in the Amazonian shelf. An increase in lithological indicators of high speeds can be expected in the Amazonian margin surrounding the constriction such as condensed sequences, reworked and eroded sediments, ferrous ooids, and conglomerates (Oczlon, 1990; Hüneke, 2006; Thorez and Dreesen, 1986). According to Hüneke (2006), calcareous bottom currents along the Rheic margins, namely in the Harz Mountains (Germany) and Eastern Central Massif (Morocco), point to higher hydraulic activity in this same period of time. The model results in this study support the conclusion by Hüneke (2006) that these higher speeds were related to the amalgamation of Gondwana to Laurussia and subsequent narrowing of the Rheic basin. Looking at the difference between a narrowed basin (Fig. 4.9) and basin closure (Fig. 4.8), it could be expected that velocities would continually increase up to the point of full closure. Nonetheless, as previously mentioned, there are many other factors that can lead to higher velocities, especially the local bathymetry. In addition, the disconnect in temporal resolution between geological evidence and model results should be kept in mind. This could lead to the recording of momentary high velocities in the geological record of an otherwise quiescent region, which can be interpreted as a general higher velocity in the region. The need for a large amount of geological evidence at various instances of time make it difficult to directly connect increases in velocity to closure or constriction of the basin.

2.) Inferring Peri-Gondwanan terrane positions

The generated surface circulation in the Famennian experiments showed that high velocities were reached at the protruding edges of the smaller terranes within the Rheic basin, as shown in Fig. 5.14. This suggests that the orientation of a terrane might be derived from indicators of high speeds within localities assumed to have been part of terranes. In addition to the Harz Mountains and Moroccan Central Massif, Hüneke (2006) also found evidence for high hydraulic activity within the Carnic Alps in Austria/Italy which might place their location at the protruding edge of the ATA that the Carnic Alps are assumed to be a part of. However, as is likewise the case when trying to infer the Gondwanan paleoposition, there is also a possibility that high hydraulic activity is related to changes in the local bathymetry. It is therefore not possible to directly correlate high energy deposits to the orientation of a terrane, and model insight is therefore limited.

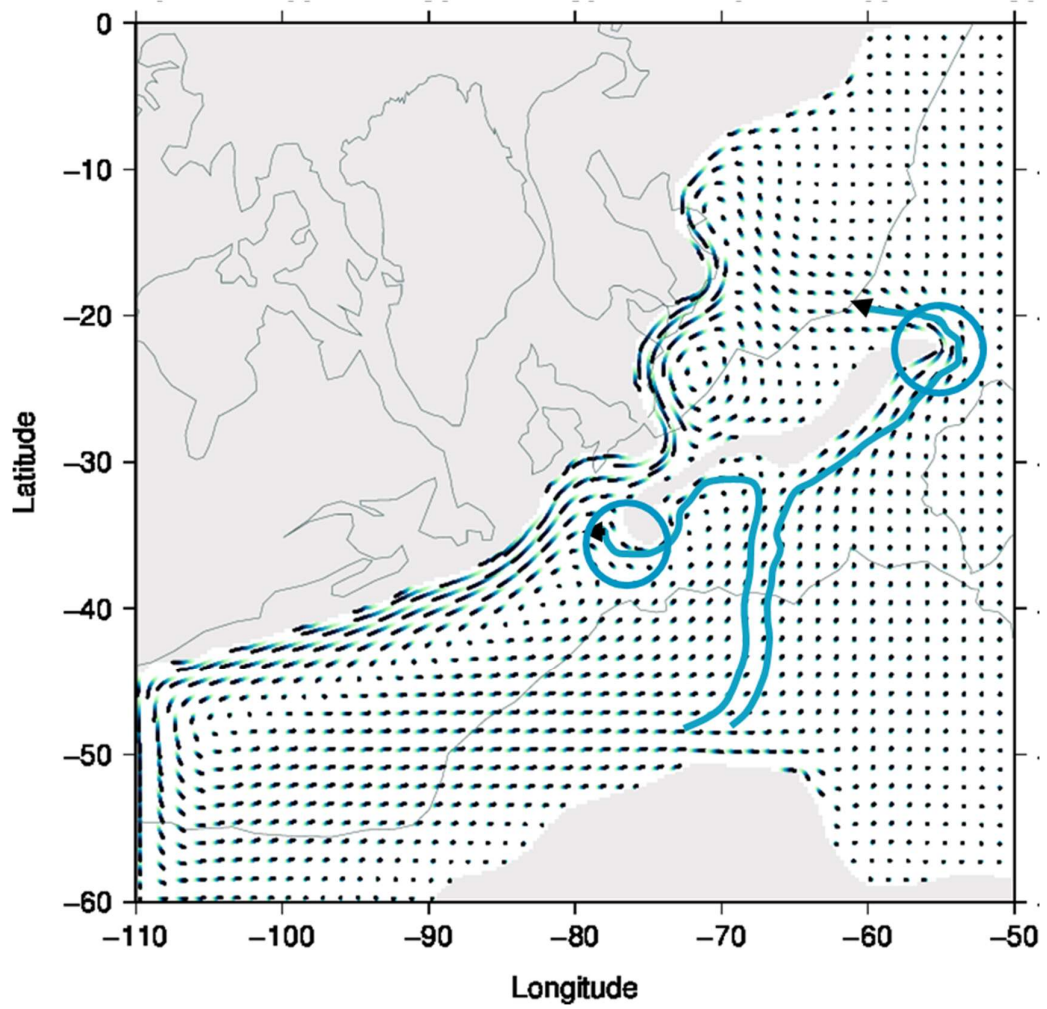


Fig. 5.14: An annotated version of the Famennian experiment results shown in Fig. 4.6b. Blue annotations highlight how the protruding edges of peri-Gondwanan terranes are subjected to higher velocities.

6 CONCLUSION

The original focus of this study evolved from modelling the circulation in a smaller Rhenohercynian oceanic basin to modelling a larger Rheic ocean basin. The reason for this was the greater paleogeographic uncertainty of the Rhenohercynian Ocean compared to the Rheic Ocean, as is the case for many of the smaller oceans and terranes within the Rheic. A simplistic model of the Rheic Ocean was constructed using 6 different land-sea distributions, two types of bathymetry and several throughflows. Aside from these paleogeographical aspects, two other controls on surface circulation were tested as well, namely the wind stress and Coriolis force.

Results show that the circulation generated by the limited area model in this study was subjected to boundary effects at south-western and western model boundaries in particular. Other than in the Tournaisian configuration, these boundaries would otherwise have been where the Rheic Ocean connected to the Panthalassa Ocean. In addition, the two-dimensionality of the model led to the generation of diffuse circulation pattern at depths greater than 200-300 meters.

Overall, model results indicated a sensitivity of the model to throughflow, wind stress and especially bathymetry. The strong sensitivity to bathymetry led to the conclusion that a more refined bathymetry is needed, which is why two possible future directions were proposed for the model. One suggestion was to focus on the shelf areas and therefore model smaller basins that can then be further constrained by the geological data reported in the numerous available studies. Such a small-scale model would then benefit from the knowledge of the general circulation patterns obtained in this study to determine the interaction the basins would have had with the gyres and currents observed in the larger Rheic Ocean. Another suggestion with regards to obtaining a more refined bathymetry would be to increase the scale to a global ocean model and by using an approximated bathymetry based on the relationship between flexure, age, and depth of the oceanic lithosphere. The global-scale model would then provide less insight on the shelf areas, and more so on the global interaction between oceans which would benefit studies looking at the climate change and biodiversity losses that occurred during for example the Devonian.

Several schematic circulation reconstructions exist for the mid-Paleozoic Rheic surface circulation. As no direct evidence remains of the deep-sea conditions in the Rheic Ocean, schematic models cannot be validated with geological data. One of the aims of this study was to, therefore, compare the circulation patterns depicted in several reconstructions with a numerical model. However, model results were difficult to compare due to a difference in plate configuration, paleogeographic reconstruction, and projection used. The plate configuration used in this study was based on the plate tectonic model by Torsvik et al. (2012) who use a Pangea-C configuration. This configuration fits well with paleomagnetic data but contrasts to most schematic reconstructions as they find their basis in sedimentary and faunal data. The schematic reconstructions show a better fit with the Pangea-A configurations.

Nonetheless, many similarities exist between the patterns depicted in the schematic circulation reconstructions and the circulation patterns generated in this study. As was the case in the majority of the schematic reconstructions, the model generated a comparable strong boundary current along Laurussia and a strong eastward current along Gondwana. One anti-cyclonic gyre was formed in the Famennian and Tournaisian experiments, showing more likeness with the reconstructions by Dopieralska (2009); Jakubowicz et al. (2019), and Oczlon (1990). The interaction between the Panthalassa, Rheic and Paleotethys Oceans was shown to have been through these gyre formations as well, as opposed to the unidirectional currents entering the Rheic from either side as depicted in the reconstructions by Hüneke (2006) and Kiessling et al. (1999).

Gaining insight on a time as far back as the mid-Paleozoic is hampered by the contradicting evidence that results in major differences between paleogeographic reconstructions. For this reason, this study was additionally aimed at determining whether numerical modelling can provide insight that can be useful in the debate on two main paleogeographic uncertainties, namely the positions of peri-Gondwanan terranes and the position of Gondwana. The modelled circulation patterns suggested that the model could be helpful in determining terrane orientation, as protruding terrane edges were subjected to the highest velocities. Other factors, however, can lead to high velocities at terrane boundaries as well, for example through shallowing of the coast. The relationship between high velocity at protruding edges and terrane orientation is therefore not diagnostic and terrane positions prove to be hard to infer through this model. With regards to the Gondwanan paleoposition, narrowing and closure of the Rheic led to high generated velocities at the Laurussian and Gondwanan margin (Amazonia and Northern Africa). Yet, in this case it is also difficult to directly link indications of high velocity to Rheic closure as other factors that influence velocity, such as local bathymetry, cannot be ruled out. The insight gained from the model on the paleogeographic controversies is therefore limited.

The Rheic model constructed in this study represents a first numerical model reconstruction of mid-Paleozoic surface circulation in the Rheic Ocean. It should, therefore, be kept in mind that the study does not aim to represent a realistic scenario of the Rheic Ocean basin but to understand the interaction of the possible factors that could have affected its circulation (exemplified by the illustration in Fig. 6.1). The model served to point out several sensitivities of the model, such as bathymetry, throughflow and wind stress, which can then be addressed in subsequent model expansions.

In summary, the model results are generally in good agreement with the available mid-Paleozoic schematic circulation models, and model results provide a more detailed circulation pattern within the basin than shown in the schematic circulation reconstructions. From the circulation patterns generated in this study, it has become evident that model improvements are needed to gain more insight on the paleogeography. These improvements include a more refined bathymetry, other boundary conditions, and three-dimensionality. It is suggested that a choice be made whether to focus on the smaller, shallow-sea circulation and to achieve higher bathymetric detail or to focus on the global, deep-sea circulation to understand the extinctions and climate change that occurred in the mid-Paleozoic.

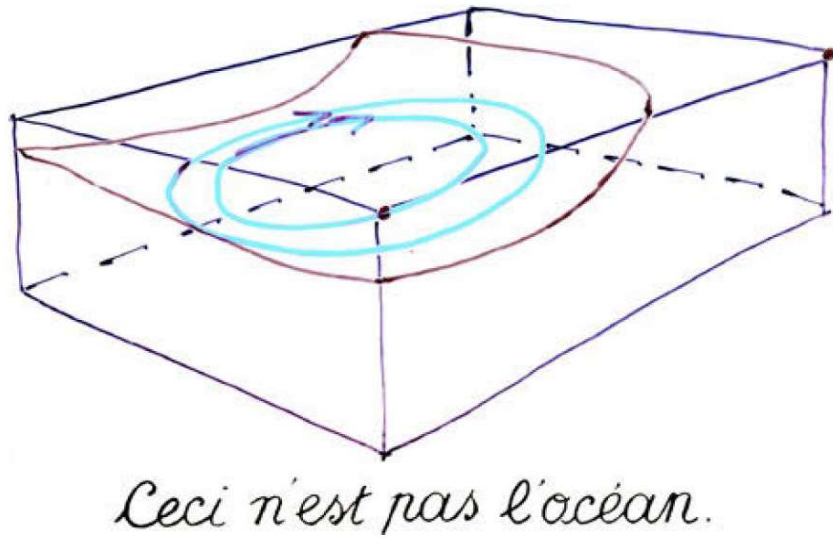


Fig. 6.1: Illustration from Olbers et al. (2012).

7 ACKNOWLEDGEMENTS

This project would never have been completed if not for Paul Meijer's continued interest and unending kindness, and I am eternally grateful to him. I also want to thank my family for all their support, patience, care, and love, and for helping me become the person that I am. This thesis has been an absolute rite of passage, which I would not have survived without the daily encouragement of my unbelievably kind friends. All the comfort, joy, advice, and warmth that I received have been the rays of sunshine that brightened my days. Thank you so very much for being a part of my journey. And last but not least, I am grateful for all the support available to students at Utrecht University, as I don't know where I would be without it.

8 REFERENCES

- Arenas, R., Díez Fernández, R., Sánchez Martínez, S., Gerdes, A., Fernández-Suárez, J., Albert, R. (2014). Two-stage collision: Exploring the birth of Pangea in the Variscan terranes. *Gondwana Research*, 25(2), 756–763. <https://doi.org/10.1016/j.gr.2013.08.009>
- Blakey, R. C. (2008). Gondwana paleogeography from assembly to breakup—A 500 m.y. odyssey. In *Special Paper 441: Resolving the Late Paleozoic Ice Age in Time and Space* (pp. 1–28). Geological Society of America. [https://doi.org/10.1130/2008.2441\(01\)](https://doi.org/10.1130/2008.2441(01))
- Blumberg, A. F., Mellor, G. L. (1987). A description of a three-dimensional coastal ocean circulation model. In Norman S. Heaps (Ed.), *Three Dimensional Coastal Ocean Models* (pp. 1–16). American Geophysical Union (AGU). <https://doi.org/10.1029/co004p0001>
- Caplan, M. L., Bustin, R. M. (1999). Devonian–Carboniferous Hangenberg mass extinction event, widespread organic-rich mudrock and anoxia: causes and consequences. *Palaeogeography, Palaeoclimatology, Palaeoecology*, 148(4), 187–207. [https://doi.org/10.1016/S0031-0182\(98\)00218-1](https://doi.org/10.1016/S0031-0182(98)00218-1)
- Caputo, M. V., Melo, J. H. G., Streef, M., Isbell, J. L. (2008). Late Devonian and Early Carboniferous glacial records of South America. *America Special Paper*, 441(11), XXX–XXX. [https://doi.org/10.1130/2008.2441\(11\)](https://doi.org/10.1130/2008.2441(11))
- Chen, D., Wang, J., Racki, G., Li, H., Wang, C., Ma, X., Whalen, M. T. (2013). Large sulphur isotopic perturbations and oceanic changes during the Frasnian–Famennian transition of the Late Devonian. *Journal of the Geological Society*, 170(3), 465–476. <https://doi.org/10.1144/jgs2012-037>
- Chereskin, T. K., Price, J. F. (2018). Upper Ocean Structure: Ekman Transport and Pumping ☆. In *Reference Module in Earth Systems and Environmental Sciences*. <https://doi.org/10.1016/b978-0-12-409548-9.11161-3>
- Cocks, L. R. M., Torsvik, T. H. (2002). Earth geography from 500 to 400 million years ago: a faunal and palaeomagnetic review. *Journal of the Geological Society*, 159(6), 631–644. <https://doi.org/10.1144/0016-764901-118>
- Cocks, L. R. M., Torsvik, T. H. (2006). European geography in a global context from the Vendian to the end of the Palaeozoic. *Geological Society, London, Memoirs*, 32(1), 83–95. <https://doi.org/10.1144/gsl.mem.2006.032.01.05>
- Copper, P. (1986). Frasnian/Famennian mass extinction and cold-water oceans. *Geology*, 14(10), 835–839. [https://doi.org/10.1130/0091-7613\(1986\)14<835:FMEACO>2.0.CO;2](https://doi.org/10.1130/0091-7613(1986)14<835:FMEACO>2.0.CO;2)
- Copper, P. (2002). Silurian and Devonian Reefs: 80 Million Years of Global Greenhouse Between Two Ice Ages. *Phanerozoic Reef Patterns*, 72, 181–238. Retrieved from http://archives.datapages.com/data/sepm_sp/SP72/Silurian_and_Devonian_Reefs.htm
- Cresswell, G., Frische, A., Peterson, J., Quadfasel, D. (1993). Circulation in the Timor Sea. *Journal of Geophysical Research*, 98(C8), 14379. <https://doi.org/10.1029/93jc00317>
- Crosby, A. G., McKenzie, D., Sclater, J. G. (2006). The relationship between depth, age and gravity in the oceans. *Geophysical Journal International*, 166(2), 553–573. <https://doi.org/10.1111/j.1365-246X.2006.03015.x>
- de la Vara, A., Meijer, P. (2016). Response of Mediterranean circulation to Miocene shoaling and closure of the Indian Gateway: A model study. *Palaeogeography, Palaeoclimatology, Palaeoecology*, 442, 96–109. <https://doi.org/10.1016/j.palaeo.2015.11.002>
- De Vleeschouwer, D., Crucifix, M., Bounceur, N., Claeys, P. (2014). The impact of astronomical forcing on the Late Devonian greenhouse climate. *Global and Planetary Change*, 120, 65–80. <https://doi.org/10.1016/j.gloplacha.2014.06.002>

- Domeier, M. (2016). A plate tectonic scenario for the Iapetus and Rheic oceans. *Gondwana Research*, 36, 275–295. <https://doi.org/10.1016/j.gr.2015.08.003>
- Domeier, M., Torsvik, T. H. (2014). Plate tectonics in the late Paleozoic. *Geoscience Frontiers*, 5(3), 303–350. <https://doi.org/10.1016/j.gsf.2014.01.002>
- Dopieralska, J. (2003). [Ph.D. Thesis] *Neodymium isotopic composition of conodonts as a palaeoceanographic proxy in the Variscan oceanic system*. *Geology*. <https://doi.org/http://geb.uni-giessen.de/geb/volltexte/2003/1168/1>
- Dopieralska, J. (2009). Reconstructing seawater circulation on the Moroccan shelf of Gondwana during the Late Devonian: Evidence from Nd isotope composition of conodonts. *Geochemistry, Geophysics, Geosystems*, 10(3), n/a-n/a. <https://doi.org/10.1029/2008GC002247>
- Dopieralska, J., Belka, Z., Haack, U. (2006). Geochemical decoupling of water masses in the Variscan oceanic system during Late Devonian times. *Palaeogeography, Palaeoclimatology, Palaeoecology*, 240(1–2), 108–119. <https://doi.org/10.1016/j.palaeo.2006.03.056>
- Eckelmann, K., Nesbor, H.-D., Königshof, P., Linnemann, U., Hofmann, M., Lange, J.-M., Sagawe, A. (2014). Plate interactions of Laurussia and Gondwana during the formation of Pangaea — Constraints from U–Pb LA–SF–ICP–MS detrital zircon ages of Devonian and Early Carboniferous siliciclastics of the Rhenohercynian zone, Central European Variscides. *Gondwana Research*, 25(4), 1484–1500. <https://doi.org/10.1016/J.GR.2013.05.018>
- Encyclopaedia Britannica. (n.d.). Mediterranean Sea | Facts, History, Islands, & Countries | Britannica.com. Retrieved February 22, 2019, from <https://www.britannica.com/place/Mediterranean-Sea>
- Ezer, T., Mellor, G. L. (2004). A generalized coordinate ocean model and a comparison of the bottom boundary layer dynamics in terrain-following and in z-level grids. *Ocean Modelling*, 6(3–4), 379–403. [https://doi.org/10.1016/S1463-5003\(03\)00026-X](https://doi.org/10.1016/S1463-5003(03)00026-X)
- Franke, W. (1989). Variscan plate tectonics in Central Europe-current ideas and open questions. *Tectonophysics*, 169(4), 221–228. [https://doi.org/10.1016/0040-1951\(89\)90088-7](https://doi.org/10.1016/0040-1951(89)90088-7)
- Franke, W. (2006). The Variscan orogen in Central Europe: construction and collapse. *Geological Society, London, Memoirs*, 32(1), 333–343. <https://doi.org/10.1144/GSL.MEM.2006.032.01.20>
- Franke, W. (2008). The mid-European segment of the Variscides: tectonostratigraphic units, terrane boundaries and plate tectonic evolution. *Geological Society, London, Special Publications*, 179(1), 35–61. <https://doi.org/10.1144/gsl.sp.2000.179.01.05>
- Franke, W., Cocks, L. R. M., Torsvik, T. H. (2017, August 1). The Palaeozoic Variscan oceans revisited. *Gondwana Research*. Elsevier. <https://doi.org/10.1016/j.gr.2017.03.005>
- Franke, W., Dulce, J. C. (2017). Back to sender: tectonic accretion and recycling of Baltica-derived Devonian clastic sediments in the Rhenohercynian Variscides. *International Journal of Earth Sciences*, 106(1), 377–386. <https://doi.org/10.1007/s00531-016-1408-y>
- Gerhard, L. C., Harrison, W. E., Hanson, B. M., American Association of Petroleum Geologists. Division of Environmental Geosciences., Kansas Geological Survey. (2001). *Geological perspectives of global climate change*. American Association of Petroleum Geologists in collaboration with the Kansas Geological Survey and the AAPG Division of Environmental Geosciences. Retrieved from https://books.google.nl/books?id=okfCqYFfCdYC&source=gbs_navlinks_s
- GMT. (n.d.). The Generic Mapping Tools. Retrieved February 23, 2019, from <http://gmt.soest.hawaii.edu/projects/gmt/wiki/Documentation>
- Golonka, J., Gaweda, A. (2012). Plate Tectonic Evolution of the Southern Margin of Laurussia

- in the Paleozoic. In *Tectonics - Recent Advances*. InTech. <https://doi.org/10.5772/50009>
- Hüneke, H. (2006). Erosion and deposition from bottom currents during the Givetian and Frasnian: Response to intensified oceanic circulation between Gondwana and Laurussia. *Palaeogeography, Palaeoclimatology, Palaeoecology*, 234(2–4), 146–167. <https://doi.org/10.1016/j.palaeo.2005.09.033>
- Jakubowicz, M., Król, J., Zapalski, M. K., Wrzolek, T., Wolniewicz, P., Berkowski, B. (2019). At the southern limits of the Devonian reef zone: Palaeoecology of the Aferdou el Mrakib reef (Givetian, eastern Anti-Atlas, Morocco). *Geological Journal*, 54(1), 10–38. <https://doi.org/10.1002/gj.3152>
- Kiessling, W., Flügel, E., Golonka, J. (1999). Paleoreef maps: Evaluation of a comprehensive database on Phanerozoic reefs. *AAPG Bulletin*, 83(10), 1552–1587. <https://doi.org/10.1306/E4FD4215-1732-11D7-8645000102C1865D>
- Kroner, U., Romer, R. L. (2013, July 1). Two plates - Many subduction zones: The Variscan orogeny reconsidered. *Gondwana Research*. Elsevier. <https://doi.org/10.1016/j.gr.2013.03.001>
- Lash, G. G. (2016). Hyperpycnal transport of carbonaceous sediment – Example from the Upper Devonian Rhinestreet Shale, western New York, U.S.A. *Palaeogeography, Palaeoclimatology, Palaeoecology*, 459, 29–43. <https://doi.org/10.1016/j.palaeo.2016.06.035>
- Linnemann, U., Gerdes, A., Drost, K., Buschmann, B. (2007). The continuum between Cadomian orogenesis and opening of the Rheic Ocean: Constraints from LA-ICP-MS U-Pb zircon dating and analysis of plate-tectonic setting (Saxo-Thuringian zone, northeastern Bohemian Massif, Germany). In *Special Paper 423: The Evolution of the Rheic Ocean: From Avalonian-Cadomian Active Margin to Alleghenian-Variscan Collision* (pp. 61–96). [https://doi.org/10.1130/2007.2423\(03\)](https://doi.org/10.1130/2007.2423(03))
- Lüning, S., Wendt, J., Belka, Z., Kaufmann, B. (2004). Temporal–spatial reconstruction of the early Frasnian (Late Devonian) anoxia in NW Africa: new field data from the Ahnet Basin (Algeria). *Sedimentary Geology*, 163(3–4), 237–264. [https://doi.org/10.1016/S0037-0738\(03\)00210-0](https://doi.org/10.1016/S0037-0738(03)00210-0)
- Marshall, J. E. A., Astin, T. R., Brown, J. F., Mark-Kurik, E., Lazauskiene, J. (2007). Recognizing the Kačák Event in the Devonian terrestrial environment and its implications for understanding land–sea interactions. *Geological Society, London, Special Publications*, 278(1), 133–155. <https://doi.org/10.1144/SP278.6>
- Martin, R. E. (2013). *Earth's evolving systems : the history of planet Earth*. Jones & Bartlett Learning. Retrieved from https://books.google.nl/books?hl=en&lr=&id=agaOKrvAoeAC&oi=fnd&pg=PR1&dq=Earth%27s+Evolving+Systems:+The+History+of+Planet+Earth&ots=qBrhuIsk7l&sig=mQad9Clrzx8V45_1h1g92bEHeC8&redir_esc=y#v=onepage&q=Earth's+Evolving+Systems%3A+The+History+of
- Martínez Catalán, J. R., Arenas, R., Abati, J., Martínez, S. S., García, F. D., Suárez, J. F., ... Carmona, A. L. (2009). A rootless suture and the loss of the roots of a mountain chain: The Variscan belt of NW Iberia. *Comptes Rendus Geoscience*, 341(2–3), 114–126. <https://doi.org/10.1016/J.CRTE.2008.11.004>
- MathWorks. (n.d.). GRABIT - File Exchange - MATLAB Central. Retrieved February 22, 2019, from <https://www.mathworks.com/matlabcentral/fileexchange/7173-grabit>
- Matte, P. (2001). The Variscan collage and orogeny (480–290 Ma) and the tectonic definition of the Armorica microplate: A review. *Terra Nova*, 13(2), 122–128. <https://doi.org/10.1046/j.1365-3121.2001.00327.x>
- Matte, P., Maluski, H., Rajlich, P., Franke, W. (1990). Terrane boundaries in the Bohemian Massif: Result of large-scale Variscan shearing. *Tectonophysics*, 177(1–3), 151–170.

[https://doi.org/10.1016/0040-1951\(90\)90279-H](https://doi.org/10.1016/0040-1951(90)90279-H)

- Matthews, K. J., Maloney, K. T., Zahirovic, S., Williams, S. E., Seton, M., Müller, R. D. (2016). Global plate boundary evolution and kinematics since the late Paleozoic. *Global and Planetary Change*, 146, 226–250. <https://doi.org/10.1016/J.GLOPLACHA.2016.10.002>
- Matyja, H. (2009). Depositional history of the Devonian succession in the Pomorian Basin, NW Poland. *Geological Quarterly*, 53(1), 63–92. Retrieved from <https://gq.pgi.gov.pl/article/view/7505/6155>
- Mellor, G. L. (2004). *Users guide for a three-dimensional, primitive equation, numerical ocean model*. Retrieved from <http://www.aos.princeton.edu/WWWPUBLIC/htdocs/pom/>
- Mellor, G. L. (George L. (1996). *Introduction to physical oceanography*. American Institute of Physics. Retrieved from <https://www.springer.com/gp/book/9781563962103>
- Menor-Salván, C., Tornos, F., Fernández-Remolar, D., Amils, R. (2010). Association between catastrophic paleovegetation changes during Devonian–Carboniferous boundary and the formation of giant massive sulfide deposits. *Earth and Planetary Science Letters*, 299(3–4), 398–408. <https://doi.org/10.1016/J.EPSL.2010.09.020>
- Monroe, J. S. (James S., Wicander, R. (2014). *The changing earth: exploring geology and evolution* (7th ed.). Cengage Learning. Retrieved from https://books.google.nl/books?id=GOKbCgAAQBAJ&dq=kaskaskia+sea&source=gbs_navlinks_s
- Morzadec, P., Paris, F., Plusquellec, Y., Racheboeuf, P., Weyant, M. (1988). Devonian Stratigraphy and Paleogeography of the Armorican Massif (Western France), 401–420. Retrieved from http://archives.datapages.com/data/cspg_sp/data/014/014001/401_cspgsp014a0401.htm
- Müller, R. D., Seton, M., Zahirovic, S., Williams, S. E., Matthews, K. J., Wright, N. M., ... Cannon, J. (2016). Ocean Basin Evolution and Global-Scale Plate Reorganization Events Since Pangea Breakup. *Annual Review of Earth and Planetary Sciences*, 44(1), 107–138. <https://doi.org/10.1146/annurev-earth-060115-012211>
- Munk, W. H., Carrier, G. F. (1950). The Wind-driven Circulation in Ocean Basins of Various Shapes. *Tellus*, 2(3), 158–167. <https://doi.org/10.3402/tellusa.v2i3.8550>
- Murphy, J. B., Keppie, J. D., Nance, R. D., Dostal, J. (2010). Comparative evolution of the Iapetus and Rheic Oceans: A North America perspective. *Gondwana Research*, 17(2–3), 482–499. <https://doi.org/10.1016/j.gr.2009.08.009>
- Nance, R. D. (2010). The Rheic Ocean: Palaeozoic evolution from Gondwana and Laurussia to Pangaea - Introduction. *Gondwana Research*, 17(2–3), 189–192. <https://doi.org/10.1016/j.gr.2009.12.001>
- Nance, R. D., Gutiérrez-Alonso, G., Keppie, J. D., Linnemann, U., Murphy, J. B., Quesada, C., ... Woodcock, N. H. (2010). Evolution of the Rheic Ocean. *Gondwana Research*, 17(2–3), 194–222. <https://doi.org/10.1016/J.GR.2009.08.001>
- Nance, R. D., Gutiérrez-Alonso, G., Keppie, J. D., Linnemann, U., Murphy, J. B., Quesada, C., ... Woodcock, N. H. (2012). A brief history of the Rheic Ocean. *Geoscience Frontiers*, 3(2), 125–135. <https://doi.org/10.1016/J.GSF.2011.11.008>
- Narkiewicz, K., Bultynck, P. (2010). The Upper Givetian (Middle Devonian) Subterminus Conodont Zone in North America, Europe and North Africa. *Journal of Paleontology*, 84(4), 588–625. <https://doi.org/10.1666/10-029.1>
- Narkiewicz, M. (2007). Development and inversion of Devonian and Carboniferous basins in the eastern part of the Variscan foreland (Poland). *Geological Quarterly*, 51(3), 231–256. Retrieved from <https://gq.pgi.gov.pl/article/view/7453>
- Narkiewicz, M., Grabowski, J., Narkiewicz, K., Niedźwiedzki, G., Retallack, G. J., Szrek, P., De Vleeschouwer, D. (2015). Palaeoenvironments of the Eifelian dolomites with earliest

- tetrapod trackways (Holy Cross Mountains, Poland). *Palaeogeography, Palaeoclimatology, Palaeoecology*, 420, 173–192. <https://doi.org/10.1016/J.PALAEO.2014.12.013>
- NOAA. (2015). Office of Satellite And Product Operations. Retrieved February 23, 2019, from <https://www.ospo.noaa.gov/Products/ocean/sst/contour/>
- Oczlon, M. S. (1990). Ocean currents and unconformities: The North Gondwana Middle Devonian. *Geology*, 18(6), 509–512. [https://doi.org/10.1130/0091-7613\(1990\)018<0509:OCAUTN>2.3.CO;2](https://doi.org/10.1130/0091-7613(1990)018<0509:OCAUTN>2.3.CO;2)
- Olbers, D. J., Willebrand, J. (Jürgen), Eden, C. (2012). *Ocean dynamics*. Springer.
- Paproth, E., Dreesen, R., Thorez, J. (1986). Famennian paleogeography and event stratigraphy of northwestern europe. *Annales de La Societe Geologique de Belgique*, 175–186. Retrieved from <https://popups.uliege.be/0037-9395/index.php?id=2472&file=1&pid=2471Subtidal>
- Paris, F., Robardet, M. (1990). *Early Palaeozoic palaeobiogeography of the Variscan regions* (Vol. 177). Retrieved from https://ac.els-cdn.com/004019519090281C/1-s2.0-004019519090281C-main.pdf?_tid=c6cecf42-104a-42cc-b622-1c6aa943f316&acdnat=1551606829_6b858a523ffea0b2bc045e6d6d23b88e
- Pereira, M. F., Gutierrez-Alonso, G., Gama, C., Drost, K., Murphy, J. B., Silva, J. B. (2017). Birth and demise of the Rheic Ocean magmatic arc(s): Combined U–Pb and Hf isotope analyses in detrital zircon from SW Iberia siliciclastic strata. *Lithos*, 278–281, 383–399. <https://doi.org/10.1016/j.lithos.2017.02.009>
- Pohl, A., Nardin, E., Vandenbroucke, T. R. A., Donnadieu, Y. (2016). High dependence of Ordovician ocean surface circulation on atmospheric CO₂ levels. *Palaeogeography, Palaeoclimatology, Palaeoecology*, 458, 39–51. <https://doi.org/10.1016/j.palaeo.2015.09.036>
- Pond, S., Pickard, G. L. (2013). *Introductory dynamical oceanography* (2nd ed.). Elsevier. Retrieved from https://books.google.nl/books?id=S6X8BAAQBAJ&source=gbs_navlinks_s
- Prestianni, C., Decombeix, A. L., Thorez, J., Fokan, D., Gerrienne, P. (2010). Famennian charcoal of Belgium. *Palaeogeography, Palaeoclimatology, Palaeoecology*, 291(1–2), 60–71. <https://doi.org/10.1016/j.palaeo.2009.10.008>
- Qiao, L., Shen, S. zhong. (2014). Global paleobiogeography of brachiopods during the Mississippian-Response to the global tectonic reconfiguration, ocean circulation, and climate changes. *Gondwana Research*, 26(3–4), 1173–1185. <https://doi.org/10.1016/j.gr.2013.09.013>
- Reimann, C. R., Bahlburg, H., Kooijman, E., Berndt, J., Gerdes, A., Carlotto, V., López, S. (2010). Geodynamic evolution of the early Paleozoic Western Gondwana margin 14°–17°S reflected by the detritus of the Devonian and Ordovician basins of southern Peru and northern Bolivia. *Gondwana Research*, 18(2–3), 370–384. <https://doi.org/10.1016/J.GR.2010.02.002>
- Ribeiro, A., Munhá, J., Dias, R., Mateus, A., Pereira, E., Ribeiro, L., ... Pedro, J. (2007). Geodynamic evolution of the SW Europe Variscides. *Tectonics*, 26(6). <https://doi.org/10.1029/2006TC002058>
- Sageman, B. B., Murphy, A. E., Werne, J. P., Ver Straeten, C. A., Hollander, D. J., Lyons, T. W. (2003). A tale of shales: the relative roles of production, decomposition, and dilution in the accumulation of organic-rich strata, Middle–Upper Devonian, Appalachian basin. *Chemical Geology*, 195(1–4), 229–273. [https://doi.org/10.1016/S0009-2541\(02\)00397-2](https://doi.org/10.1016/S0009-2541(02)00397-2)
- Scotese, R. C. (n.d.). PALEOMAP Project. Retrieved March 6, 2019, from <http://www.scotese.com/moremaps2.htm>
- Segar, D. A. (2018). *Introduction to Ocean Sciences* (4th ed.). Retrieved from <http://www.reefimages.com/oceans/SegarOcean4Chap01.pdf>

- Servais, T., Danelian, T., Harper, D. A. T., Munnecke, A. (2014). Possible oceanic circulation patterns, surface water currents and upwelling zones in the Early Palaeozoic. *GFF*, 136(1), 229–233. <https://doi.org/10.1080/11035897.2013.876659>
- Servais, T., Sintubin, M. (2009). Avalonia, Armorica, Perunica: terranes, microcontinents, microplates or palaeobiogeographical provinces? *Geological Society, London, Special Publications*, 325(1), 103–115. <https://doi.org/10.1144/sp325.5>
- Seton, M., Müller, R. D., Zahirovic, S., Gaina, C., Torsvik, T., Shephard, G., ... Chandler, M. (2012, July 1). Global continental and ocean basin reconstructions since 200Ma. *Earth-Science Reviews*. Elsevier. <https://doi.org/10.1016/j.earscirev.2012.03.002>
- Shail, R. K., Leveridge, B. E. (2009). The Rhenohercynian passive margin of SW England: Development, inversion and extensional reactivation. *Comptes Rendus - Geoscience*, 341(2–3), 140–155. <https://doi.org/10.1016/j.crte.2008.11.002>
- Slingerland, R. (1986). Numerical computation of co-oscillating palaeotides in the Catskill epeiric Sea of eastern North America. *Sedimentology*, 33(4), 487–497. <https://doi.org/10.1111/j.1365-3091.1986.tb00756.x>
- Smith, L. B., Fred Read, J. (2000). Rapid onset of late Paleozoic glaciation on Gondwana: Evidence from Upper Mississippian strata of the Midcontinent, United States. *Geology*, 28(3), 279. [https://doi.org/10.1130/0091-7613\(2000\)28<279:ROOLPG>2.0.CO;2](https://doi.org/10.1130/0091-7613(2000)28<279:ROOLPG>2.0.CO;2)
- Stampfli, G. M., Hochard, C., V erard, C., Wilhem, C., VonRaumer, J. (2013, May 8). The formation of Pangea. *Tectonophysics*. Elsevier. <https://doi.org/10.1016/j.tecto.2013.02.037>
- Stets, J., Sch afer, A. (2011). The Lower Devonian Rhenohercynian Rift – 20 Ma of sedimentation and tectonics (Rhenish Massif, W-Germany) [Das unterdevonische Rhenoherzynische Rift – 20 Ma Sedimentation und Tektonik (Rheinisches Schiefergebirge, Westdeutschland)]. *Zeitschrift Der Deutschen Gesellschaft F ur Geowissenschaften*, 162(2), 93–115. <https://doi.org/10.1127/1860-1804/2011/0162-0093>
- Tait, J., Sch atz, M., Bachtadse, V., Soffel, H. (2000). Palaeomagnetism and Palaeozoic palaeogeography of Gondwana and European terranes. *Geological Society, London, Special Publications*, 179(1), 21–34. <https://doi.org/10.1144/gsl.sp.2000.179.01.04>
- Thorez, J., Dreesen, R., Streel, M. (2006). Fammenian. *Geologica Belgica*, 9(1–2), 27–45. Retrieved from <http://www.vliz.be/en/imis?refid=221600>
- Torsvik, T. H., Cocks, L. R. M. (2004). Earth geography from 400 to 250 Ma: a palaeomagnetic, faunal and facies review. *Journal of the Geological Society*, 161(4), 555–572. <https://doi.org/10.1144/0016-764903-098>
- Torsvik, T. H., Cocks, L. R. M. (2016). *Earth History and Palaeogeography*. *Earth History and Palaeogeography*. <https://doi.org/10.1017/9781316225523>
- Torsvik, T. H., Van der Voo, R., Preeden, U., Mac Niocaill, C., Steinberger, B., Doubrovine, P. V., ... Cocks, L. R. M. (2012). Phanerozoic polar wander, palaeogeography and dynamics. *Earth-Science Reviews*, 114(3–4), 325–368. <https://doi.org/10.1016/J.EARSCIREV.2012.06.007>
- van Staal, C. R., Barr, S. M., Murphy, J. B. (2012). Provenance and tectonic evolution of Ganderia: Constraints on the evolution of the iapetus and Rheic oceans. *Geology*, 40(11), 987–990. <https://doi.org/10.1130/G33302.1>
- von Raumer, J. F., Nesbor, H. D., Stampfli, G. M. (2017). The north-subducting Rheic Ocean during the Devonian: consequences for the Rhenohercynian ore sites. *International Journal of Earth Sciences*, 106(7), 2279–2296. <https://doi.org/10.1007/s00531-016-1425-x>
- von Raumer, J. F., Stampfli, G. M. (2008). The birth of the Rheic Ocean - Early Palaeozoic subsidence patterns and subsequent tectonic plate scenarios. *Tectonophysics*, 461(1–4), 9–20. <https://doi.org/10.1016/j.tecto.2008.04.012>
- Wells, M. R., Allison, P. A., Hampson, G. J., Piggott, M. D., Pain, C. C. (2005). Modelling ancient

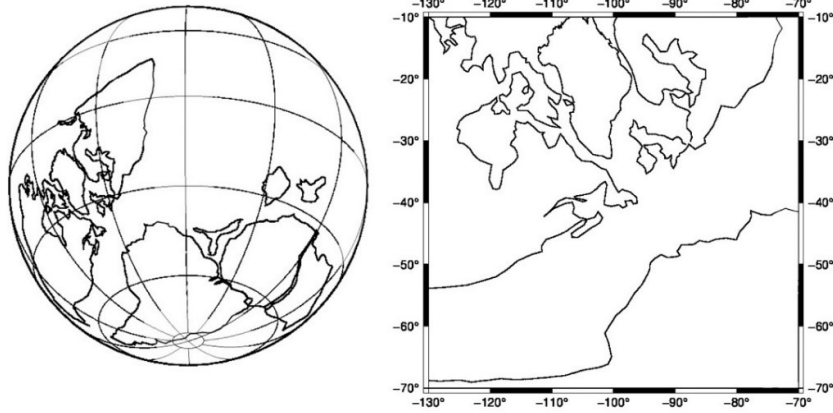
- tides: The Upper Carboniferous epi-continental seaway of Northwest Europe. *Sedimentology*, 52(4), 715–735. <https://doi.org/10.1111/j.1365-3091.2005.00718.x>
- Wendt, J., Kaufmann, B., Belka, Z., Klug, C., Lubeseder, S. (2006). Sedimentary evolution of a Palaeozoic basin and ridge system: The middle and upper Devonian of the Ahnet and Mouydir (Algerian Sahara). *Geological Magazine*, 143(3), 269–299. <https://doi.org/10.1017/S0016756806001737>
- Wicander, E. R. (1975). Fluctuations in a late devonian-early Mississippian phytoplankton flora of Ohio, U.S.A. *Palaeogeography, Palaeoclimatology, Palaeoecology*, 17(2), 89–108. [https://doi.org/10.1016/0031-0182\(75\)90048-6](https://doi.org/10.1016/0031-0182(75)90048-6)
- Woodcock, N. H., Soper, N. J., Strachan, R. A. (2007). A Rheic cause for the Acadian deformation in Europe. *Journal of the Geological Society*, 164(5), 1023–1036. <https://doi.org/10.1144/0016-76492006-129>
- Zeh, A., Gerdes, A. (2010). Baltica- and Gondwana-derived sediments in the Mid-German Crystalline Rise (Central Europe): Implications for the closure of the Rheic ocean. *Gondwana Research*, 17(2–3), 254–263. <https://doi.org/10.1016/j.gr.2009.08.004>
- Zhenyu, Z., Yaoqi, Z., Guosheng, J. (2007). The periodic growth increments of biological shells and the orbital parameters of Earth-Moon system. *Environmental Geology*, 51(7), 1271–1277. <https://doi.org/10.1007/s00254-006-0420-0>

9 APPENDICES

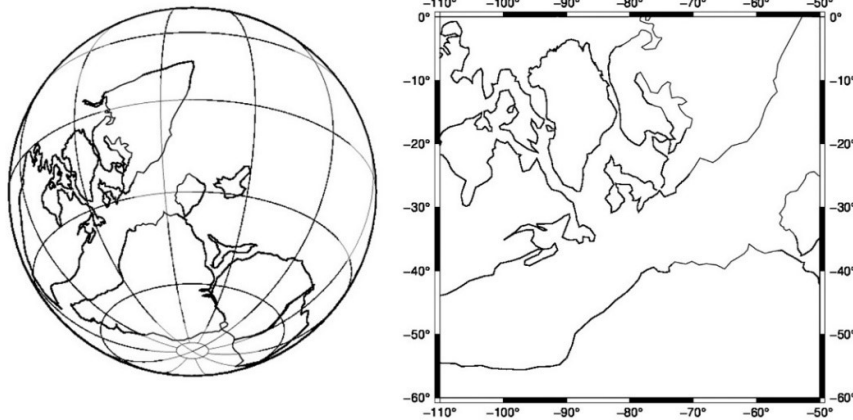
APPENDIX A – COMPLETE SET OF MODEL DOMAINS.....	102
APPENDIX B – REPRODUCING THE DATA.....	103

APPENDIX A – COMPLETE SET OF MODEL DOMAINS

Emsian



Famennian



Tournaisian

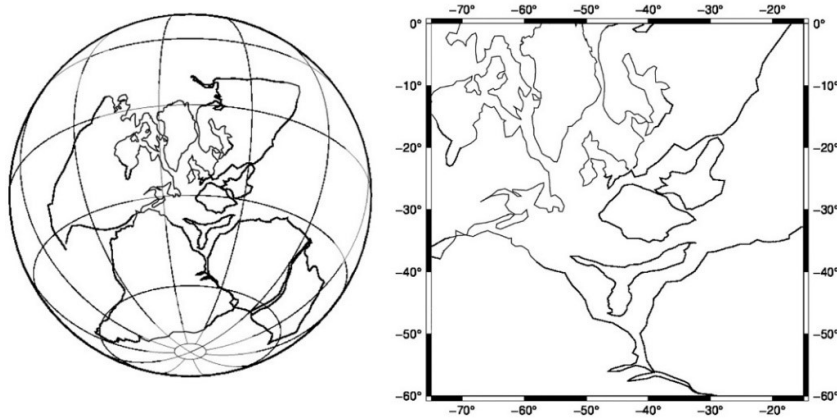


Fig. A.1: Global plate configuration projected with an orthogonal projection on the left. Model domain of same plate configuration projected with a Cartesian linear projection on the right.

APPENDIX B – REPRODUCING THE DATA

Princeton Ocean Model (POM) code:

- The numerical model used in this study was based on the POM08_WAD code version which was last modified on April 25th, 2008 and created by L. Oey.
- Files for this version are found at http://www.ccpo.odu.edu/POMWEB/POM08_WAD/
- The scripts provided in the POM08_WAD will be further called the original version and consists of the following:
 - grid indicates grid dimensions
 - params standard input values for pom08.f
 - pom08.c Common blocks for pom08.f
 - pom08.f program code
 - pom08.n NetCDF subroutines for pom08.f
- An additional subroutine written by Paul Meijer (pers.comm.) was incorporated into the pom08.f program code, called “subroutine basin”. The supplied version of this code which was not altered by me will also be referred to as the original.
- The following tables only the parameters that have changed from the original scripts:
 - Table B-1 lists which parameters have been altered as well as their location within the scripts.
 - Table B-2 lists the parameters that require lengthy functions/addresses and have therefore not been included in Table B-1.

Generic Mapping Tools (GMT)

- Scripts used to generate figures and masks were written for the GMT 4.5.14 version and can be provided upon request.
- Additional information for making the model domains:
 - Tectonic continental units were traced on a present-day world map, which was generated with GMT. This world map was projected with a Cartesian linear projection (-JX15d).
 - The shape of the continental units were largely based on the tectonic units described in Torsvik and Cocks (2016, p. 38-76)
 - These continental units were rotated with angles to reproduce the plate configurations from Torsvik et al. (2012). We used a different method than Torsvik et al. (2012) and were not able to reproduce the plate configurations with the data provided in the publication. Rotation angles were therefore provided by Trond Helge Torsvik through personal communication.

Table B-1: Overview of parameters that deviate from the original values in pom08.f, params, grid, and subroutine basin

Description	Parameter	Input	Where to alter
	<u>Non-parameter alterations to POM08 code</u>		
Add new parameters	ylat0, dxdeg, dydeg, gr	add to common blocks	pom08.c
Add new parameters	bwlengthe, bwlengthw, transe,	define in subroutine	
incorporate subroutine basin	transw	basin	subroutine basin
	lproblem	add to iproblem lists	main program/params
	<u>Grid</u>		
Length	im	241	main program/params
Width	jm	241	main program/params
Vertical levels	kb	16	main program/params
Bathymetry			
Uniform depth	h(i,j)	200	subroutine basin
		Depth file, see Table	
Variable depth	h(i,j)	B-2	subroutine basin
	<u>Boundary conditions</u>		
Close north boundary	h(i, 1)	1	subroutine basin
Close south boundary	h(i, jm)	1	subroutine basin
Close east boundary	h(1,j)	1	subroutine basin
Close west boundary	h(im,j)	1	subroutine basin
Throughflow	bwlengthe, bwlengthw, transe, transw	see Table B-2	subroutine basin
		see Table B-2, and see condition A-1,	
Type of boundary condition	uaf, elf, vaf	Mellor (2002, pg 29)	subroutine bcond
	<u>Forcing</u>		
Coriolis force	cor(i,j)	see Table B-2	subroutine basin
Devonian rotation	omega	0.0000836	subroutine basin
Emsian lowest latitude (in degrees)	ylat0	-70	subroutine basin AND main program
Famennian/Tournasian latitude	ylat0	-60	subroutine basin AND main program
Cell size	dxdeg	0.25	subroutine basin AND main program
Cell size	dydeg	dydeg=dxdeg	subroutine basin AND main program
Conversion to degrees	gr	pi/180	subroutine basin AND main program
Idealized zonal wind	wusurf(i,j), wvsurf(i,j)	see Table B-2	main program
Uniform zonal wind	wusurf(i,j), wvsurf(i,j)	see Table B-2	main program
Uniform meridional wind	wusurf(i,j), wvsurf(i,j)	see Table B-2	main program
NOAA windstresses	wusurf(i,j), wvsurf(i,j)	see Table B-2	main program
No tidal forcing	nwad	0	main program/params
	nsmolar	0	main program/params
no salinity	sbias	35	subroutine basin
No temperature	tbias	10	subroutine basin
	<u>Time Stepping</u>		
cfl condition (dti/dte)	isplit	10	main program/params
external time step	dte	10	main program/params
ramping	lramp	lramp=.true.	main program
	period	7	main program
run duration	days	150	main program/params
initial print interval	prtd1	1	main program/params
final print interval	prtd2	0.5	main program/params
time to switch from prtd1 to prtd2	swtch	110	main program/params
	<u>General</u>		
set to 2 dimensions	mode	2	main program/params
call subroutine basin	iproblem	0	main program/params

Table B-2: Overview of functions used in pom08.f

Description	Function	Additional information
Bathymetry: depth files		
<u>Emsian:</u>		
Torsvik, uniform depth	read (10,*) h(i,j)	Depth file location: /net/home/vleugel/work18/masks/ocean/182808/400ma/uniform/uniform400ma.z
Torsvik, variable depth	read (10,*) h(i,j)	/net/home/vleugel/work18/masks/ocean/182808/400ma/generated/generated400ma.z
Torsvik-shelf break, uniform depth	read (10,*) h(i,j)	/net/home/vleugel/work18/masks/ocean/2016/0922/160922_400ma.z
<u>Famennian:</u>		
Torsvik, uniform depth	read (10,*) h(i,j)	/net/home/vleugel/work18/masks/ocean/182808/370ma/uniform/torsvik370ma.z
Torsvik, variable depth	read (10,*) h(i,j)	/net/home/vleugel/work18/masks/ocean/182808/370ma/generated/generated370ma.z
Dopierska, uniform depth	read (10,*) h(i,j)	/net/home/vleugel/work18/masks/ocean/182808/370ma/uniform/dopier_island.z
Huneke, uniform depth	read (10,*) h(i,j)	/net/home/vleugel/work18/masks/ocean/182808/370ma/uniform/huneke370ma.z
<u>Tournaisian:</u>		
Torsvik, uniform depth	read (10,*) h(i,j)	/net/home/vleugel/work18/masks/ocean/2016/2811/162811_350isl.z
Wind stress functions		
Idealized zonal wind	wusurf(i,j)=ramp*(0.15*cos(3.e0*(ylat*gr))+0.05)/rhoref wvsurf(i,j)=0.e0	
Uniform zonal wind	wusurf(i,j)=ramp*(-0.10/rhoref) wvsurf(i,j)=0.e0	
Uniform meridional wind	wusurf(i,j)=0.e0 wvsurf(i,j)=ramp*(-0.10/rhoref)	
NOAA windstresses	read (10,*) wusurf(i,j) wusurf(i,j)=ramp*1.e0*(wusurf(i,j)/rhoref) wvsurf(i,j)=0.e0	/net/home/vleugel/work18/masks/NOAAwind/zonal70wusurf.z'
Throughflow functions		
1. replace evap with transe and transp	transe=-1*1000000.e0 transw=-1*1000000.e0 bwlengthe=0.e0 bwlengthw=0.e0	Equals 1 Sverdrup towards the east. Replace -1 with -5 or -7 for the 5 Sverdrup and 7 Sverdrup scenario
2. calculate length of east and west boundaries	do j= 1,jm bwlengthe= bwlengthe + dum(imm1,j)*5.e-1*(dy(im,j)+dy(imm1,j)) bwlengthw= bwlengthw + dum(2,j)*5.e-1*(dy(1,j)+dy(2,j)) end do do j= 2,jmm1 if (dum(imm1,j).gt.0.e0) uabe(j)= transe/bwlengthe end do	
3. Divide total transport across boundary	do j= 2,jmm1 if (dum(2,j).gt.0.e0) uabw(j)= transw/bwlengthw end do	
Boundary Conditions		
Eastern boundary conditions	uaf(im,j)=2*uabe(j)/(h(im,j)+elf(im,j)+h(imm1,j)+elf(imm1,j)) uaf(im,j)=ramp*uaf(im,j) vaf(im,j)=0.e0 uaf(2,j)=2*uabw(j)/(h(1,j)+elf(1,j)+h(2,j)+elf(2,j)) uaf(2,j)=ramp*uaf(2,j) uaf(1,j)=uaf(2,j) vaf(1,j)=0.e0	
Western boundary conditions	vaf(1,j)=0.e0	
Coriolis functions		
Uniform coriolis	cor(i,j)=1.e-4	standard value at midlatitudes
Devonian coriolis	cor(i,j)=2.*omega*sin(ylat*gr)	omega=8.36e-5
Midlatitude coriolis	cor(i,j)=2.*omega*sin(35*gr)	ylat replaced with of 35 degrees
Normal coriolis	cor(i,j)=2.*omega*sin(ylat*gr)	omega= 7.292e-5